

AD-A271 085



ATION PAGE

Form Approved  
OMB No. 0704-0188

②

Provide a number response including the time for reviewing instructions, searching existing data sources, gathering and maintaining the data needed, completing and reviewing the collection of information, and sending comments regarding this burden estimate or any other aspect of this collection of information, including suggestions for reducing this burden estimate, to the Office of Management and Budget, Paperwork Reduction Project (0704-0188), Washington, DC 20503.

1. AGENCY USE ONLY (Leave blank)		2. REPORT DATE Sept. 17, 1993	3. REPORT TYPE AND DATES COVERED Final Report 5/1/92-4/30/93	
4. TITLE AND SUBTITLE Performance Potential of Plasma Thrusters: Arcjet and Hall Thruster Modeling			5. FUNDING NUMBERS FQ 8671-9300908 G-AFOSR-91-0256	
6. AUTHOR(S)  Manuel Martinez-Sanchez, PI				
7. PERFORMING ORGANIZATION NAME(S) AND ADDRESS(ES) Space Power and Propulsion Laboratory MIT, Dept. of Aero/Astro 77 Massachusetts Ave Cambridge, MA 02139			8. PERFORMING ORGANIZATION REPORT NUMBER  AFOSR-TR-93-0753	
9. SPONSORING / MONITORING AGENCY NAME(S) AND ADDRESS(ES) AFOSR/NA 110 Duncan Ave., Suite B115 Bolling AFB, D.C. 20332-0001			10. SPONSORING / MONITORING AGENCY REPORT NUMBER	
11. SUPPLEMENTARY NOTES				
12a. DISTRIBUTION / AVAILABILITY STATEMENT  Approved for public release; distribution is unlimited.			12b. DISTRIBUTION CODE	
13. ABSTRACT (Maximum 200 words)  This is the second and final yearly Report on Grant 91-0256, for the period 5/1/92-4/30/93. The Report describes two recently completed and highly successful models for the internal physics and the performance of hydrogen arcjets and Hall thrusters, respectively. These are thought to represent the state of the art in their respective topics. Also discussed is an equally significant theoretical model of MPD anode drops, which completes previously funded work.				
14. SUBJECT TERMS Electric Propulsion, Arcjets, Hall Thrusters			15. NUMBER OF PAGES 15	
			16. PRICE CODE	
17. SECURITY CLASSIFICATION OF REPORT Unclassified	18. SECURITY CLASSIFICATION OF THIS PAGE Unclassified	19. SECURITY CLASSIFICATION OF ABSTRACT Unclassified	20. LIMITATION OF ABSTRACT UL	

93-24268



# PERFORMANCE POTENTIAL OF PLASMA THRUSTERS: ARCJET AND HALL THRUSTER MODELING

## Yearly Technical Progress Report on Grant AFOSR-91-0256

Covering the period: 5/1/92-4/30/93

by

Manuel Martinez-Sanchez  
Professor of Aero/Astro  
MIT, Room 37-401  
Cambridge, MA 02139

Attn: Mitat A. Birkan  
AFOSR/NA  
110 Duncan Ave., Suite B115  
Bolling AFB  
Washington, D.C. 20332-0001

Accession For	
NTIS CRA&I	<input checked="checked" type="checkbox"/>
DTIC TAB	<input type="checkbox"/>
Unannounced	<input type="checkbox"/>
Justification .....	
By .....	
Distribution /	
Availability Codes	
Dist	Avail and/or Special
A-1	

DTIC QUALITY INSPECTED 2

September 17, 1993

## **1. Introduction**

The purpose of this Grant is to develop theoretical tools for performance assessment of Plasma Propulsion devices. These models can be used for design purposes, as correlators of experimental data, and as pointers to necessary technology improvements.

In our first Yearly Progress Report <sup>[1]</sup> we showed results of a simplified arcjet model which was then being finalized by Graduate Student Atsuko Sakamoto. The final results of this work have since appeared in Ms. Sakamoto's M.S. Thesis <sup>[2]</sup>, and have been presented in a paper at the 29th Joint Propulsion Conference<sup>[3]</sup>. The method is capable of good ( $\pm 20\%$ ) a priori predictions of thrust and efficiency over a wide range of parameters, but requires some judgment in the selection of input parameters, and provides little detailed information on the internal flow parameters. Also in the first Yearly Report, we showed the development and preliminary results of a detailed arcjet numerical model which was part of Scott Miller's Ph.D. Thesis work. This model is now essentially complete, and results have also been presented at the Joint Propulsion Conference<sup>[4]</sup>. This is probably the most accurate description available of the hydrogen arcjet physics, and provides first-principles performance predictions as well as internal parameter distributions which illuminate the device's operation and suggest routes for improvement. The JPC paper summarizes these results, and is appended for further detail. Additional results, dealing principally with the thermal coupling between the gas and the arcjet body, are still being generated, and will be the subject of a subsequent paper to be presented at the 23rd International Electric Propulsion Conference. Scott Miller's Ph.D. Thesis is expected to be available by Sept. 1993.

In addition to the arcjet work, we have also developed during this 2nd Grant Year a one-dimensional model for a Hall thruster, which has yielded excellent results when compared to experimental data. This has been the subject of a M.S. Thesis by Chris Lentz<sup>[5]</sup>, and also of a paper presented at the Joint Propulsion Conference<sup>[6]</sup>. Although partial attempts had been made before at modeling Hall thruster operation, it appears that ours is the only truly quantitative and accurate theory in existence at this time. The work is described in the JPC paper, which is appended to this Report, and in more detail in Ch. Lentz' Thesis, which is expected in August 1993.

The good results obtained in both the arcjet and the Hall thruster tasks have opened the way for further refinements and for explorations of performance-raising modifications.

Thus, work is now being initiated (under a new AFOSR Grant) on mixed N<sub>2</sub>-H<sub>2</sub> arcjet modeling, examination of alkali seeding in arcjets, and 2-D Hall Thruster models.

Although the Grant being reported on did not cover work on MPD thrusters, work that had been initiated under earlier AFOSR Grants has been continued. In particular, the 2-D numerical model of MPD which was developed by Eli Niewood to examine in detail the genesis of near-anode voltage drops has been completed. This was the subject of Dr. Niewood's Thesis<sup>[7]</sup>, and was also presented at the Joint Propulsion Conference<sup>[8]</sup>. This work constitutes the first coherent explanation for the appearance and magnitude of the anode drop in MPD thrusters, which is by far their largest power loss and is also the source of difficult anode thermal management problems. The JPC paper is appended to this Report, and a copy of Dr. Niewood's Thesis is also included.

## **2. Numerical Model for Hydrogen Arcjets**

Previous numerical modeling of arcjet thrusters has focused on the development of 1-D, 2-D, and axisymmetric models with relatively simple physics and geometries. The level of detail has ranged from 1-D models [9] to coupled quasi-analytic models of the inner (arc) and outer (cold gas) flows [3,10,11], to simplified axisymmetric space-marching techniques [12], and finally to 2-D and axisymmetric viscous codes which begin to incorporate most of the detailed physical processes [13,14,15]. The latest research has obtained results which variously include ohmic heating, electron heat conduction, thermal and ionizational nonequilibrium, and empirical models of radiation losses. Issues left out of these models include viscous and diffusive effects (of importance in these very low Reynolds number devices), coupling of the block thermal response (which affects the gas temperature around the arc, and hence the specific impulse), and, more importantly, electron thermal non-equilibrium ( $T_e \neq T_g$ ) and the detailed arc attachment physics. If thermal equilibrium is forced, as has been done so far, the electrical conductivity outside the arc, and particularly near the anode wall, is nearly zero, because the single temperature is held down by cooling to the wall. This makes it impossible to obtain steady solutions with a prescribed current of the right magnitude, unless an artificial "floor" is introduced for the conductivity. Unfortunately neither the magnitude nor the spatial distribution of this artificial  $\sigma_{MIN}$  can be gleaned from such a model, and this throws in doubt the voltage prediction as well as that of the anode heat flux and its distribution. To some extent, this has been mitigated by artificially imposing (as well) the current distribution on the anode, based on empirical information.

In our work, we have decoupled  $T_e$  from  $T_g$  by separately balancing electron and gas energies. The results show that  $T_e$  remains close to  $T_g$  in the arc, where the collisional coupling is strong, but whereas the near-anode  $T_g$  is of the order of 1000-3000K, the corresponding  $T_e$  is of the order of 20,000K there, and, in fact, that a continuous "bridge" zone of high  $T_e$  connects the arc to the anode. This is shown clearly in Fig. 1, which is a radial cut in the attachment region. Since the electrical conductivity is

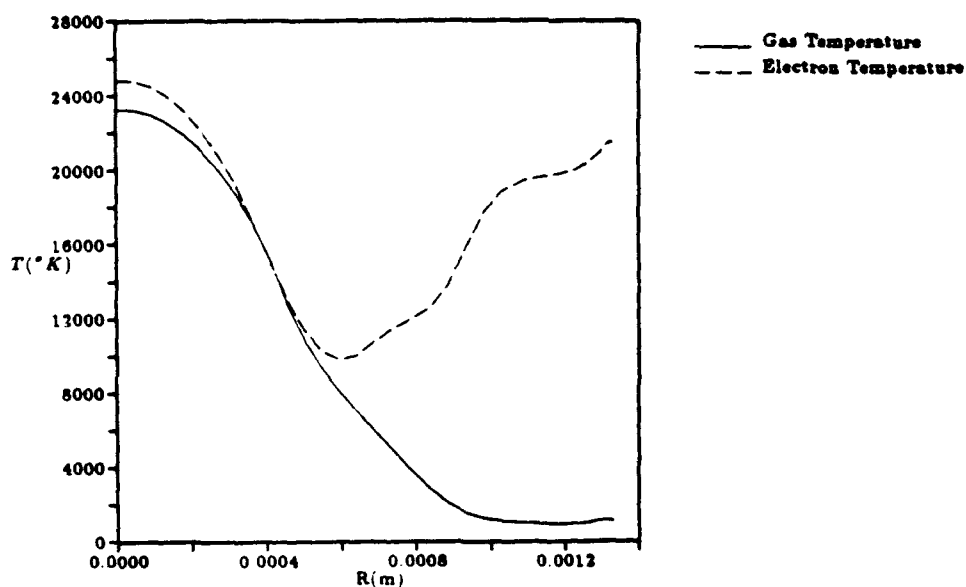


Fig. 1: Radial Profiles of Electron and Heavy Species Temperatures 0.25mm Downstream of the Constrictor Exit

governed by  $T_e$ , this bridge all the way to the wall allows the current connection to be made, with a net voltage drop which is very close to that measured experimental (see the attached paper, AIAA 93-2101, for details).

Not as essential, but also important for the physics of the attached region is the allowance for ambipolar diffusion of electron-ion pairs from a region of intense net ionization about 0.1mm from the wall to the wall itself, bridging any possible electron-poor thin layer there. This is shown in Fig. 2, where the dominant terms in the electron density balance are profiled.

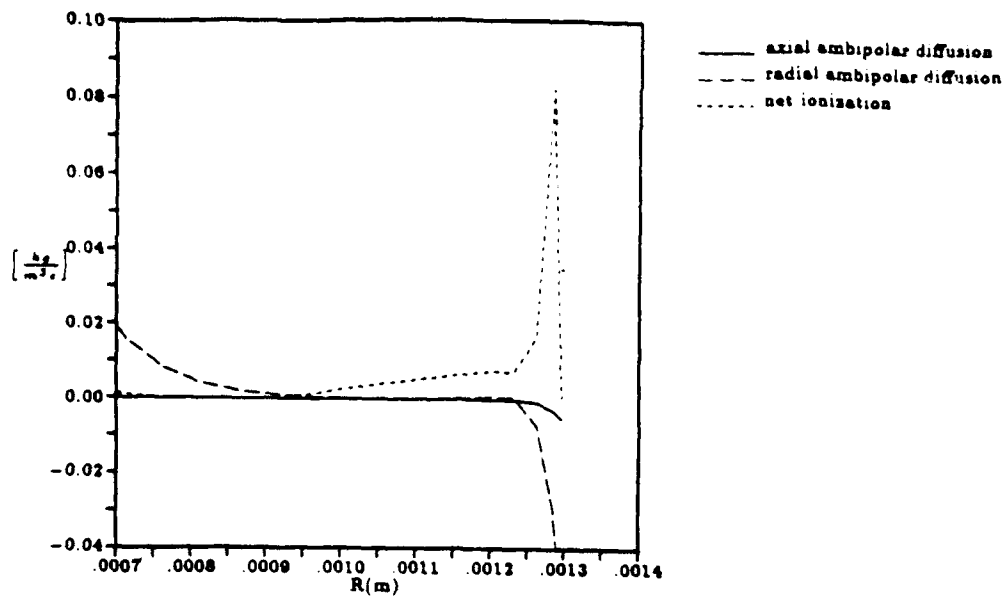
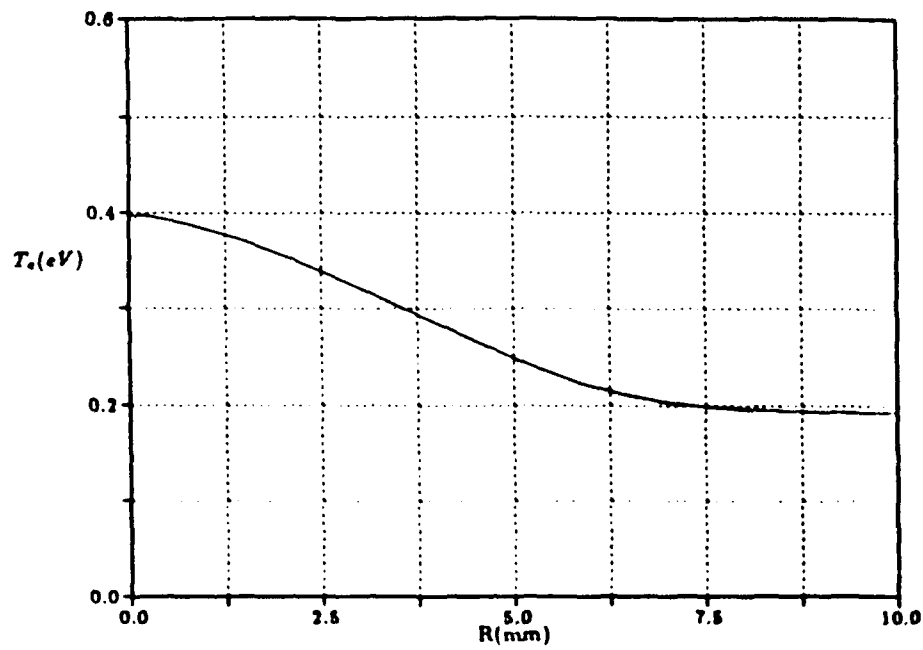


Figure 2. Radial Profiles of Some Terms in the Electron Density Equation in the Current Attachment Region Just Downstream of the Constrictor Exit

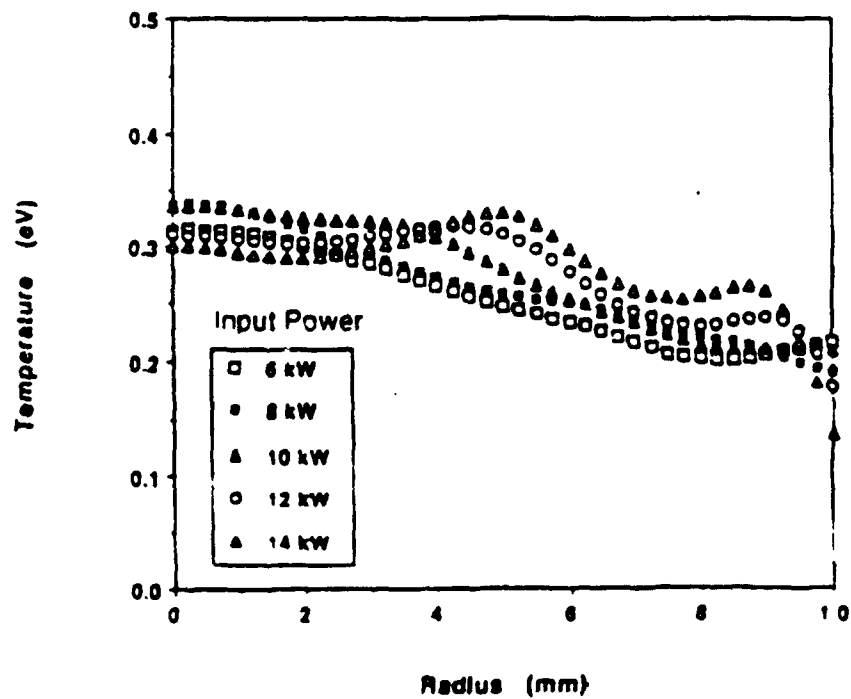
When these effects are tracked through the 2-D computational domain, the re-attachment distribution in the region downstream of the constrictor is obtained naturally in a manner which is realistic, although no detailed experimental distributions are available for hot anodes (See Fig. 4 of the attached paper AIAA 93-2101). The veracity of the  $T_e$  calculation is also proven by comparing the predicted  $T_e$  profile at the thruster exit (Fig. 3) to data of Haskins et al [16] and of Spores [17]. In both cases the measured  $T_e$  and its radial profile agree within 0.1 eV with our results; the data of Ref. 16 were taken a few mm. downstream of the exit plane, which may account for most of the difference.

Despite these important improvements to the anode attachment problem, no complete success can yet be claimed. On one hand, we do slightly under-predict voltage (by 7V out of 112 in the nominal case, but exploratory calculations for other conditions give voltage errors of up to 19V. in some instances). More importantly, we are still forced to restrict attachment to the region beyond the constrictor, and if this limitation is removed, attachment gradually creeps upstream without apparent limits. The mechanism which anchors the arc foot is not completely captured, and may require finer detail of the sheath and the surface chemistry to be modeled.

# CALCULATION:



# EXPERIMENTAL (Ref. 16)



Radial Electron Temperature Profiles at the Exit Plane



A broad measure of success for the model is its performance predictive ability. As Fig. 11 of the included Paper AIAA 93-2101 shows, the thrust (or the specific impulse) is within 5-10% of the experimental data in all cases tested, consistently showing some overprediction.

The situation for voltage is similar (Table 6 of the Paper). A wider set of conditions is currently being explored, and the results will be documented in an IEPC paper in September.

The other improvement contributed by our model is the ability to accurately model the thermal response of a radiatively cooled thruster body, and to couple this to the fluid model. The thermal time constant is of the order of seconds, compared to the  $\sim 50$   $\mu$ sec time scale for flow development, and this makes it impossible to numerically track both time evolutions in an interactive manner. Instead, the calculation is iterative, alternating between a flow solution with a frozen wall temperature and a steady state thermal computation using as input the heat flux from the latest flow update. This is mainly important in setting the outer gas temperature, which controls the thruster specific impulse. In fact, as Refs. 2 and 3 have shown, the role of the arc is simply to "plug up" a fraction of the constrictor exit area, with most of the flow passing around the arc. The temperature of this outer gas is decoupled from the arc, and is governed by wall heat transfer, particularly regenerative heating upstream of the cathode, and this temperature, in turn, controls the outer flow sonic speed, and hence the specific impulse. The detailed iterations are only now being conducted, and the results will also be reported in the upcoming IEPC paper. The results discussed here so far have all assumed a wall temperature of 1000K upstream, increasing to 1200K at the constrictor exit.

### **3. Numerical Model for a Hall Thruster**

In the early 1960's, under A.I. Morozov, the Soviets developed the first concept of a thruster with closed electron drift and an extended acceleration zone. Between 1964-1969, these thrusters were improved and evolved into the Hall thruster. Much experimental work has been performed in the Soviet Union by Morozov [18,19,20], Bugrova [21,22], Smirnov [23], Bishaev [24], Esipchuck [25] and Zubkov [26] to list a few. A great deal has been learned from the data about thruster design, scaling, plasma properties in the acceleration channel, and in improving performance.

Very little work had been performed on numerically modeling these thrusters. Kaufman [27] modeled performance for a variety of assumed potential profiles. Partial analysis of many of the important processes were reported in the Soviet literature [18-26] and also, more recently in the work of Yamagiwa and Kuriki [28]. Komurasaki et. al. [29], at the University of Tokyo, created simplified one and two dimensional models for the plasma. These models assume a constant ionization to loss ratio, use a simplified ionization model, and neglect thermal conduction in the electron energy equation.

The thrust of our research was to develop a more detailed and accurate model of the physical processes in the acceleration region. This model was then used to examine thruster performance over various operational power levels using Argon and Xenon as propellants.

This research uses a quasi-one dimensional transient model for the plasma properties down the length of the channel. The geometry for the model is taken from an actual thruster for comparison of the numerical results with collected data. The magnetic field is assumed to be imposed and taken as constant in time and the plasma is assumed to be quasi-neutral. Careful treatment is given to the electron energy equation, including heat conduction in its derivation. An ion distribution function as a function of the electric field, ionization rates and wall losses is defined and calculated. Additionally, momentum transfer between ions and neutrals is considered.

The leakage of electrons from the downstream cathode to the upstream anode is an important process in the physics of Hall thrusters, and the radial magnetic field is introduced to control this leakage, as well as to slow down the flow of secondary electrons to the anode. This increases the probability of a given electron producing ionizing collision with the neutral gas, and also creates a high density electron population to neutralize the ions during their acceleration. We have modeled the plasma impedance to the flow of electrons by an extension of Bohm's anomalous diffusion concepts, following Ref. 29. This results from electron scattering by turbulent field fluctuations. The Russian literature [21] has suggested that electron-wall collisions also have the effect of interrupting electron Larmor gyrations, thereby inducing additional field-aligned drifts and creating a near-wall shorting layer. This effect was not accounted for in our study. The results, as will be shown, appear to justify our approximations, but further examination of the possible effects of wall shorting is needed.

Since the details of the model are explained in the attached paper AIAA 93-2491, we will here only comment on the salient aspects of the results and on perceived remaining uncertainties and research needs.

The internal consistency of the model was verified by careful comparison the to the data of Ref. 29 on the axial distribution of (transversally averaged) ion density, electron temperature, ionization rate and potential (see Figs. 7-11 of AIAA 93-2491), which are predicted consistently within  $\pm 10\%$  of the data. This was important in order to avoid compensating errors which might still fortuitously yield good performance results. Especially noteworthy is the good prediction of  $T_e(x)$ , because there are several competing channels for the energy gained by electrons from the field, thermal energy being only one of them. This  $T_e$ , in turn, determines the local ionization rate, whose accurate prediction is important to ensure that the proper efficiency is calculated.

The final check on the model is the calculation of thruster efficiency when only the anode current and the mass flow rate are specified. This involves calculation of the voltage (not specified) and the beam current (smaller than the anode current by the amount of electron upstream leakage). We have carried out computations for the conditions of the experiments of Ref. 29, using Argon propellant. To date, we have only completed the case of  $\dot{m} = 2Aeq$ , over the tested  $I_{anode}$  range. The results, reproduced in Fig. 4 (from our paper) are excellent. Similar calculations covering

the full range of mass flows of the tests, as well as the cases where Xe was used as propellant, are now underway, and will be reported at the IEPC Seattle meeting (Sept. 1993). Preliminary results are very encouraging.

Despite this success, several areas require further attention:

(a) As noted, wall conductivity was not included, which may be important for other conditions.

(b) The loss of electron-ion pairs to recombination on walls was modeled originally by assuming perfect plasma-wall contact and using the flux  $\Gamma = 0.61n_e v_B$ , where  $v_B$  is the Bohm velocity. This proved excessive, and, since the 2-D data indicate that the plasma near the anode is not in direct contact with the wall, a shape factor was included, going from 0 at the anode to 1 at mid-channel. Clearly, this kind of approximation can only be made with confidence in view of either some 2-D data or some 2-D computational results.

(c) The plasma fluctuations are implicitly accounted for in the anomalous resistance, but are not explicitly calculated otherwise, nor are any other potential macroscopic instabilities assessed. Local stability analyses were reported early on [18], but these can only serve as rough guidelines, and much more work is needed here (probably in terms of direct simulations).

(d) Experimenters report wide beam divergence, and associated lip erosion by impinging ions. This is another 2-D effect requiring 2-D calculations.

We plan to work to these problems in the coming two years, by developing a 2-dimensional code for Hall thrusters. Initial efforts in this direction are aimed at assessing the feasibility of directly simulating electron transport by means of particle-in-cell codes, or, alternatively, extending the phenomenological approach used so far to the 2-D case.

## **References**

- [1] M. Martinez-Sanchez, "Performance Potential of Plasma Thrusters: Arcjet Modeling". First Yearly Progress Report on Grant AFOSR-91-0256, for the period 5/1/92-4/30/93. Aug. 20, 1992.
- [2] Atsuko Sakamoto, Simplified Modeling and Analysis of Arcjet Thrusters. M.S. Thesis in Aeronautics and Astronautics, MIT, Feb. 1993.
- [3] M. Martinez-Sanchez and A. Sakamoto, "Simplified Analysis of Arcjet Thrusters". Paper AIAA 93-1904, 29th Joint Propulsion Conference, Monterey, CA., June 1993.
- [4] Scott A. Miller and M. Martinez-Sanchez, "Multifluid Non-equilibrium Simulation of Electrothermal Arcjets". Paper AIAA 93-2101, 29th JPC, Monterey, CA, June 1993.
- [5] Christopher A. Lentz, Transient One Dimensional Numerical Simulation of Hall Thrusters. M.S. Thesis in Aeronautics and Astronautics, MIT, Aug. 1993.
- [6] Ch. A. Lentz and M. Martinez-Sanchez, "Transient One-Dimensional Simulation of Hall Thrusters". Paper AIAA 93-2491, 29th JPC, Monterey, CA, June 1993.
- [7] Eliahu H. Niewood, An Explanation for Anode Voltage Drops in MPD Thrusters. Ph.D. Thesis, MIT, June 1993.
- [8] E.H. Niewood and M. Martinez-Sanchez, "An Explanation for Anode Voltage Drops in MPD Thrusters". Paper AIAA 93-2104, 29th JPC, Monterey, CA., June 1993.
- [9] R. Spurrett and R.A. Bond, "Modeling Arcjet Thruster Performance", IEPC 91-110, AIDAA/AIAA/DGLR/JSASS 22nd International Electric Propulsion Conference, Viareggio, Italy, October 1991.
- [10] B. Glocker, H.O. Schrade, and P.C. Sleziona, "Numerical Prediction of Arcjet Performance", AIAA 90-2612, AIAA/DGLR/JSASS 21st International Electric Propulsion Conference, Orlando, July 1990.

- [11] B. Glocker and M. Auweter-Kurtz, "Numerical and Experimental Constrictor Flow Analysis of a 10kW Thermal Arcjet", AIAA 92-3835, AIAA/SAE/ASME/ASEE 28th Joint Propulsion Conference, Nashville, July 1992.
- [12] M. Andrennucci et al., "Development of a Computer Programme for the Analysis of Arcjet Nozzles", IEPC 91-113, AIDAA/AIAA/DGLR/JSASS 22nd International Electric Propulsion Conference, Viareggio, Italy, October 1991.
- [13] G.W. Butler and D.Q. King, "Single and Two Fluid Simulations of Arcjet Performance", AIAA 92-3104, AIAA/SAE/ASME/ASEE 28th Joint Propulsion Conference, Nashville, July 1992.
- [14] R. Rhodes and D. Keefer, "Modeling Arcjet Space Thrusters", AIAA 91-1994, AIAA/SAE/ASME/ASEE 27th Joint Propulsion Conference, Sacramento, June 1991.
- [15] R. Rhodes and D. Keefer, "Comparison of Model Calculations With Experimental Data From Hydrogen Arcjets", IEPC-91-111, AIDAA/AIAA/DGLR/JSASS 22nd International Electric Propulsion Conference, Viareggio, Italy, October 1991.
- [16] W.A. Hoskings, A.E. Kull, and G.W. Butler, "Measurement of Population and Temperature Profiles in an Arcjet Plume", AIAA 92-3240, AIAA/SAE/ASME/ASEE 28th Joint Propulsion Conference, Nashville, July 1992.
- [17] Ronald Spores, Personal Communication
- [18] Morozov, A.I., Esipchuck, Yu. V and Kapulkin, A.M., "Azimuthally Asymmetric Modes and Anomalous Conductivity in Closed Electron Drift Accelerators", Sov. Phys. Tech Phys., 18 P. 615, 1973.
- [19] Morozov, A.I. Esipchuck, YU. V., Kapulkin, A.M., Nevrovskii, V.A. and Smirnov, V.A., "Effect of the Magnetic Field on a Closed-Electron-Drift Accelerator", Sov. Phys.-Tech. Phys., 17, P. 482, 1972.
- [20] Morozov, A.I. Esipchuck, Yu. V., Tilinin, G.N., Trofimov, A.V., Sharov, Yu. A. and Shchepkin, G. Ya., "Plasma Accelerator With Closed Electron Drift and Extended Acceleration Zone, "Sov. Phys.-Tech. Phys. 17 P. 38, 1972.

[21] Bugrova, A.I., Kim, B., Maslennikov, N.A. and Morozov, A.I., "Physical Process and Characteristics of Stationary Plasma Thrusters with Closed Electron Drift", IEPC-91-079, AIDAA/AIAA/DGLR/JSASS 22nd International Electric Propulsion Conference, Viareggio, Italy, Oct. 1991.

[22] Bugrova, A.I., Morozov, A.I. and Kharchevnikov, V.K., "Probe Measurements of Drift Current in a Hall Accelerator", Sov. Phys.-Tech. Phys., 30, P. 610, 1985.

[23] Smirnov, V.A., "Electron Energy Balance in a Hall-Current Accelerator with an Extended Acceleration Zone", Sov. J. Plasma Phys. 5, P. 202, 1979.

[24] Bishaev, A.M. and Kim, V., "Local Plasma Properties in a Hall-Current Accelerator with an Extended Acceleration Zone", Sov. Phys.-Tech. Phys., 23, p. 1055, 1978.

[25] Esipchuk, Yu. V. and Tilinin, G.N., "Drift Instability in Hall-Current Plasma Accelerator", Sov. Phys.-Tech. Phys., 21, P. 419, 1976.

[26] Zubkov, I.P., Kislov, A. Ya. and Morozov, A.I., "Experimental Study of a Two-Lens Accelerator", Sov. Phys.-Tech. Phys., 15, P. 1796, 1971.

[27] Kaufman, H.R., "Technology of Closed-Drift Thrusters" AIAA Journal, Vol. 23, No. 1, 1985 pp. 78-87.

[28] Yamagiwa, Y. and Kuriki, K. "Performance of Double Stage-Discharge Hall Ion Thruster". J. of Propulsion and Power, Vol. 7, No. 1, Jan-Feb. 1991, pp. 65-70.

[29] Komurasaki, K., Hirakawa, M. and Arakawa, Y., "Plasma Acceleration Processes in a Hall-Current Thruster", IEPC-91-078, AIDAA/AIAA/DGLR/JSASS 22nd International Electric Propulsion Conference, Viareggio, Italy, Oct. 1991.

## **APPENDIX**

### **RELEVANT PUBLICATIONS**

Following are the papers by (a) S. Miller and M. Martinez-Sanchez on arcjet modeling, (b) Ch. Lentz and M. Martinez-Sanchez on Hall thruster modeling, (c) E. Niewood and M. Martinez-Sanchez on anode drops in MPD thruster, and (d) M. Martinez-Sanchez and A. Sakamoto on a simplified arcjet model. These contain detailed technical accounts of the topics discussed above.





**AIAA 93-2101**

**Multifluid Nonequilibrium Simulation of  
Electrothermal Arcjets**

**S. A. Miller and M. Martinez-Sanchez**

**Space Power and Propulsion Laboratory**

**Dept. of Aeronautics and Astronautics**

**MIT**

**Cambridge, MA**

**AIAA/SAE/ASME/ASEE**

**29th Joint Propulsion**

**Conference and Exhibit**

**June 28-30, 1993 / Monterey, CA**

# MULTIFLUID NONEQUILIBRIUM SIMULATION OF ELECTROTHERMAL ARCJETS

S.A. Miller\* and M. Martinez-Sanchez †

Space Power and Propulsion Laboratory

Dept. of Aeronautics and Astronautics, MIT, Cambridge, MA 02139

## Abstract

A detailed model has been developed to study the gasdynamic flow in an electrothermal arcjet thruster through numerical simulation. This two-temperature model consistently incorporates viscosity and heat conduction effects by expressing the governing equations in a Navier-Stokes form. Other simulated effects include ohmic dissipation, collisional energy transfer between electrons and heavy species, ambipolar diffusion, nonequilibrium dissociation and ionization, and continuum radiation. The fluid equations are solved by MacCormack's method, while an iterative procedure is used to relax an electric potential equation, from which the current distribution in the thruster is obtained. Converged solutions are compared with experimental results from the German TT1 radiatively-cooled arcjet thruster with hydrogen propellant. Results are presented for a baseline case which reveal the two-dimensional, two-fluid nature of the interior flow, especially in terms of the distribution and anode attachment of the electric current and the growth and development of the arc region. Calculated discharge voltage is within a few percent of experimental measurements, and predicted specific impulse is within 5-10% agreement over a range of operating parameters.

## Nomenclature

$\hat{c}_v$	Specific heat at constant volume [ $J/mole/^\circ K$ ]
$D_a$	Ambipolar diffusion coefficient [ $m^2/s$ ]
$d_{ee}$	Ambipolar flux of ions and electrons [ $1/m^2/s$ ]
$e$	Electric charge [ $C$ ], internal energy [ $J/kg$ ]
$\vec{E}$	Electric field [ $V/m$ ]
$E_i$	Ionization energy [ $J$ ]
$E_d$	Dissociation energy [ $J$ ]
$E_l$	Elastic collisional energy transfer [ $W/m^3$ ]
$E_{vib}$	Vibrational excitation energy [ $J$ ]

$h$	Planck's constant [ $J_s$ ], enthalpy [ $J/kg$ ]
$I$	Total current [ $A$ ]
$\vec{j}$	Electric current density [ $A/m^2$ ]
$k$	Boltzman's constant [ $J/^\circ K$ ]
$K$	Equilibrium constant
$m$	Particle mass [ $kg$ ]
$n$	Number density [ $1/m^3$ ]
$\dot{n}_e$	Net electron production rate [ $1/m^3/s$ ]
$\dot{n}_H$	Net atomic hydrogen production rate [ $1/m^3/s$ ]
$\hat{N}$	Avogadro's number [ $1/mole$ ]
$p$	Scalar pressure [ $Pa$ ]
$\vec{q}$	Heat flux vector [ $W/m^2$ ]
$R$	Real gas constant [ $J/kg/^\circ K$ ]
$\hat{R}$	Universal gas constant [ $J/mole/^\circ K$ ]
$\dot{R}$	Energy loss due to continuum radiation [ $W/m^3$ ]
$T$	Temperature [ $^\circ K$ ]
$\vec{u}$	Mean flow velocity [ $m/s$ ]
$v_B$	Bohm velocity [ $m/s$ ]
$\vec{V}$	Slip velocity [ $m/s$ ]
$x$	Mole fraction
$\alpha$	Ionization fraction
$\kappa$	Coefficient of thermal conductivity [ $W/m/^\circ K$ ]
$\mu$	Coefficient of viscosity [ $kg/ms$ ]
$\nu$	Collision frequency [ $1/s$ ]
$\phi$	Electric potential [ $V$ ]
$\Phi$	Viscous dissipation function [ $W/m^3$ ]
$\psi$	Electron mobility [ $m^2/\Omega/C$ ]
$\rho$	Mass density [ $kg/m^3$ ]
$\sigma$	Electrical conductivity [ $mho/m$ ], molar concentration
$\bar{\Omega}$	Average effective collision integral [ $m^2$ ]

## 1 Introduction

Low power arcjet thrusters have recently been flight qualified through ground testing and will soon be tested in space for stationkeeping of geosynchronous communication satellites. Most of the impetus for design strategies, however, has come from empirical studies and experimentation, and a need remains to better understand the underlying physics, detailed energy balances, and transport mechanisms

\*Graduate Student, Member AIAA

†Professor, Member AIAA

Copyright ©1993 by the American Institute of Aeronautics and Astronautics, Inc. All rights reserved.

of these devices. In order to fully understand the physics of arcjet thrusters, it is necessary to accurately model many complex interacting phenomena. Unfortunately, the complexity of the models and equations needed to accurately represent these devices effectively limits the use of analytic techniques to simplified cases, through which one may obtain useful physical insights but inadequate predictions of thruster performance. Experimental techniques provide much useful empirical data, but many quantities of interest are not accessible in the important regions of the thrusters. For these reasons numerical methods of solving the governing equations have become an important tool for conducting arcjet thruster research.

Previous numerical modeling of arcjet thrusters has focused on the development of 1-D, 2-D, and axisymmetric models with relatively simple physics and geometries. The level of detail has ranged from 1-D models[1] to coupled quasi-analytic models of the inner (arc) and outer (cold gas) flows[2, 3, 4], to simplified axisymmetric space-marching techniques[5], and finally to 2-D and axisymmetric viscous codes which begin to incorporate most of the detailed physical processes[6, 7, 8]. The latest research has obtained results which variously include ohmic heating, electron heat conduction, thermal and ionizational nonequilibrium, and empirical models of radiation losses. There are still a number of issues, such as viscous and diffusive effects, arc formation and attachment, the heat balance in the anode, and ultimately the accurate prediction of voltage and efficiency, which need to be addressed. This paper describes a generalized, more physically accurate model of the gasdynamic flow through an arcjet thruster, which includes the aforementioned effects and compares favorably to experimental results obtained with medium power hydrogen arcjets.

## 2 Model

### 2.1 Basic Assumptions

A basic diagram of an electrothermal arcjet thruster is shown in Figure 1. This model is based on an axisymmetric formulation. Consequently, variations in flow quantities in the azimuthal direction are neglected. A component of the flow velocity in the  $\theta$ -direction, however, is incorporated to account for the "swirl" injection of most experimental arcjets. This injected vortex has been shown to stabilize arc attachment and to help maintain a concentrated arc along the centerline of the thruster. Although  $u_\theta$  is assumed constant in the  $\theta$ -direction, it is allowed to develop in the axial and radial directions through

the conservation of global angular momentum.

The model has been developed in a general enough sense so that any monatomic or diatomic propellant may be simulated. For the purpose of this research hydrogen was selected as the propellant of choice, due to its low molecular weight (and therefore high performance) and its simple molecular structure, which allows for analytic evaluation of the necessary transport coefficients. Nonequilibrium dissociation and ionization are modeled, and four species of particles are tracked: diatomic molecules, monatomic neutrals and ions, and electrons. Dissociation is modeled by heavy species collisions and by electron impact, and the ionization process is based on electron impact ionization and three-body recombination, with only  $H^+$  ions considered.

The following assumptions are made regarding the state of the flow in the thruster and the physical processes involved. The plasma produced by ionizing electron collisions is assumed to be macroscopically neutral, so that  $n_e = n_i$ . Strong coupling is assumed between the ions and neutrals, designated together as the heavy species. This implies that  $\bar{u}_i \cong \bar{u}_n \cong \bar{u}$  (except for ambipolar diffusion), and  $T_i \cong T_n \cong T_g$ . Effects which are consistently incorporated include ambipolar diffusion, heat conduction, viscous shear and dissipation, ohmic heating, collisional energy transfer between electrons and heavy species, and energy lost through continuum radiation. The self-induced magnetic field of the ionized gas is neglected due to the low current density and thus negligible magnetic pressure in arcjet thrusters, and the individual species are assumed to obey the ideal gas law. Given the aforementioned assumptions, the model can be summarized by a set of nine partial differential equations which must be solved locally in order to generate a viable simulation of the flow in an arcjet thruster.

### 2.2 Governing Equations

The set of equations which govern the flow in the model arcjet thruster of this research is essentially a group of modified Navier-Stokes equations. These include an equation of state and equations for the ion, neutral atom, and global density; the axial, radial, and azimuthal global momentum; the electron and heavy species energy; and the electric potential. In order to maintain numerical robustness, these equations are written in as conservative a manner as possible, particularly with respect to the  $\frac{1}{r}$  terms which appear due to the axisymmetry of the problem.

The electric potential equation is derived by combining Ohm's law,  $\vec{j} = \sigma \vec{E} + \psi \nabla p_e$ , with the equation

$\nabla \cdot \vec{j} = 0$ , where  $\psi = \frac{e}{m_e \sum \nu_{ee}}$  is the electron mobility. Assuming a potential of the form  $\vec{E} = -\nabla \phi$ , the resulting equation is given by

$$\frac{1}{r} \frac{\partial}{\partial r} (r \phi_r) + \frac{\partial}{\partial z} (\phi_z) = \psi \left( \frac{\partial^2 p_e}{\partial r^2} + \frac{1}{r} \frac{\partial p_e}{\partial r} + \frac{\partial^2 p_e}{\partial z^2} \right) + \frac{\partial p_e}{\partial r} \frac{\partial \psi}{\partial r} + \frac{\partial p_e}{\partial z} \frac{\partial \psi}{\partial z}, \quad (1)$$

where

$$\phi_r = \sigma \frac{\partial \phi}{\partial r} \quad \text{and} \quad \phi_z = \sigma \frac{\partial \phi}{\partial z}. \quad (2)$$

The current density may then be extracted by solving

$$j_r = \psi \frac{\partial p_e}{\partial r} - \sigma \frac{\partial \phi}{\partial r} \quad \text{and} \quad j_z = \psi \frac{\partial p_e}{\partial z} - \sigma \frac{\partial \phi}{\partial z}. \quad (3)$$

The global density equation is obtained by summing the individual species continuity equations:

$$\frac{\partial \rho_r}{\partial t} + \frac{\partial \rho u_r}{\partial r} + \frac{\partial \rho u_z}{\partial z} = 0. \quad (4)$$

For the ion (or electron) density, the governing equation is derived from the statement of ion mass conservation, modified to account for the ambipolar flux of charged particles in terms of ion density gradients:

$$\frac{\partial \rho_e}{\partial t} + \frac{\partial (\rho_e u_r + d_{er})}{\partial r} + \frac{\partial (\rho_e u_z + d_{ez})}{\partial z} = m_e \dot{n}_e, \quad (5)$$

where  $\vec{d}_e$  is the ambipolar flux, given by

$$\vec{d}_e = -D_a \nabla \rho_e; \quad D_a = \sqrt{\frac{\pi k T_g}{4 m_n}} \frac{(1 + \frac{T_e}{T_g})}{Q_{in}(n_e + n_n)}. \quad (6)$$

The source term  $\dot{n}_e$  represents the net rate of production of ions per unit volume through inelastic collisional processes. The statement of neutral atom mass conservation is obtained in a similar manner, and the effect of ambipolar diffusion is consistently included by assuming that both neutral species travel at the same velocity and by employing the definition of the mean flow velocity ( $\vec{u} = \sum_j \rho_j \vec{u}_j / \sum_j \rho_j$ ):

$$\begin{aligned} \frac{\partial \rho_H}{\partial t} + \frac{\partial \rho_H u_r}{\partial r} - \frac{\partial}{\partial r} \left( \frac{\rho_H}{(\rho_{H_2} + \rho_H)} \frac{m_H}{m_e} d_{er} \right) \\ + \frac{\partial \rho_H u_z}{\partial z} - \frac{\partial}{\partial z} \left( \frac{\rho_H}{(\rho_{H_2} + \rho_H)} \frac{m_H}{m_e} d_{ez} \right) \\ = m_H (\dot{n}_{H+} + \langle \sigma v \rangle n_e n_{H_2} - \dot{n}_e) r. \end{aligned} \quad (7)$$

Here the source term represents the net rate of production of neutral atoms, given by the difference between the net rate of production due to dissociation

and the net rate of ionization of those neutral atoms produced.

The three global momentum equations are given by

$$\begin{aligned} \frac{\partial \rho u_r}{\partial t} + \frac{\partial (\rho u_r^2 + p - \tau_{rr})}{\partial r} + \frac{\partial (\rho u_r u_z - \tau_{rz})}{\partial z} \\ + \tau_{\theta\theta} - \rho u_\theta^2 - p = 0, \end{aligned} \quad (8)$$

$$\begin{aligned} \frac{\partial \rho u_\theta}{\partial t} + \frac{\partial (\rho u_r u_\theta - \tau_{r\theta})}{\partial r} + \frac{\partial (\rho u_\theta u_z - \tau_{\theta z})}{\partial z} \\ + \rho u_r u_\theta = 0, \quad \text{and} \end{aligned} \quad (9)$$

$$\frac{\partial \rho u_z}{\partial t} + \frac{\partial (\rho u_r u_z - \tau_{rz})}{\partial r} + \frac{\partial (\rho u_z^2 + p - \tau_{zz})}{\partial z} = 0; \quad (10)$$

and the corresponding viscous stress tensor components in axisymmetric coordinates are

$$\tau_{rr} = \frac{2}{3} \mu_g \left( 2 \frac{\partial u_r}{\partial r} - \frac{\partial u_z}{\partial z} - \frac{u_r}{r} \right) \quad (11)$$

$$\tau_{\theta\theta} = \frac{2}{3} \mu_g \left( 2 \frac{u_r}{r} - \frac{\partial u_r}{\partial r} - \frac{\partial u_z}{\partial z} \right) \quad (12)$$

$$\tau_{zz} = \frac{2}{3} \mu_g \left( 2 \frac{\partial u_z}{\partial z} - \frac{\partial u_r}{\partial r} - \frac{u_r}{r} \right) \quad (13)$$

$$\tau_{r\theta} = \mu_g \left( \frac{\partial u_\theta}{\partial r} - \frac{u_\theta}{r} \right) \quad (14)$$

$$\tau_{rz} = \mu_g \left( \frac{\partial u_r}{\partial z} + \frac{\partial u_z}{\partial r} \right) \quad (15)$$

$$\tau_{\theta z} = \mu_g \frac{\partial u_\theta}{\partial z}. \quad (16)$$

The heavy species energy equation is

$$\begin{aligned} \frac{\partial \rho e_g}{\partial t} + \frac{\partial (\rho e_g u_r + q_{gr})}{\partial r} + \frac{\partial (\rho e_g u_z + q_{gz})}{\partial z} \\ + \frac{\partial (\rho_{H_2} e_{H_2} V_{H_2} + \rho_H e_H V_H + \rho_{H+} e_{H+} V_{H+})}{\partial r} \\ + \rho_{H_2} \frac{\partial V_{H_2}}{\partial r} + \rho_H \frac{\partial V_H}{\partial r} + \rho_{H+} \frac{\partial V_{H+}}{\partial r} \\ + p_g \left( \frac{\partial u_r}{\partial r} + \frac{\partial u_z}{\partial z} \right) = \left( \Phi + E_I - \frac{1}{2} E_d \dot{n}_H \right) r, \end{aligned} \quad (17)$$

where the internal energy and enthalpy are defined by

$$\begin{aligned} \rho e_g = \frac{3}{2} (\rho_H + \rho_{H+}) R_H T_g + \frac{5}{2} \rho_{H_2} R_H T_g \\ + \frac{\rho_{H_2} R_H \theta_v}{e^{\frac{\theta_v}{T_g}} - 1} - \frac{7}{4} \rho_H T_g, \end{aligned} \quad (18)$$

and

$$\rho h_g = \rho e_g + \rho_H R_H T_g + (\rho_H + \rho_{H+}) R_H T_g. \quad (19)$$

Additional flux terms have been included in the radial direction to account for the radial transport of energy by ambipolar diffusion; these terms are dependent on the internal energy and slip velocity ( $V_{j,r}$ ) of each species. The heat flux vectors in Eqn. 17 can be expressed as

$$q_{g,r} = -k_g \frac{\partial T_g}{\partial r} \quad \text{and} \quad q_{g,z} = -k_g \frac{\partial T_g}{\partial z}, \quad (20)$$

while the viscous dissipation function is given by

$$\begin{aligned} \Phi = \mu_g \left[ 2 \left( \frac{\partial u_r}{\partial r} \right)^2 + 2 \left( \frac{\partial u_z}{\partial z} \right)^2 + 2 \left( \frac{u_r}{r} \right)^2 \right. \\ \left. + \left( \frac{\partial u_r}{\partial z} + \frac{\partial u_z}{\partial r} \right)^2 + \left( \frac{\partial u_\theta}{\partial r} - \frac{u_\theta}{r} \right)^2 + \left( \frac{\partial u_\theta}{\partial z} \right)^2 \right. \\ \left. - \frac{2}{3} \left( \frac{\partial u_r}{\partial r} + \frac{\partial u_z}{\partial z} + \frac{u_r}{r} \right)^2 \right]. \quad (21) \end{aligned}$$

The collisional transfer of energy from electrons to the heavy species is represented by the following expression:

$$E_l = 3 \frac{\rho_e}{m_H} (\nu_{eH^+} + \nu_{eH} + \delta_e \nu_{eH_2}) k (T_e - T_g). \quad (22)$$

The coefficient  $\delta_e$  in Eqn. 22 is necessary to correct for the fact that electron- $H_2$  collisions are inelastic in nature. An internal energy form of the heavy species energy equation is utilized rather than a more conservative total energy form because of numerical concerns. In some regions of an arcjet thruster the kinetic energy and the net loss of energy due to dissociation can become so large that numerical difficulties arise if these terms are kept in a total energy state vector. The same is true of the net loss of energy due to ionization in the electron energy equation.

The conservation of energy for electrons is given by the following expression:

$$\begin{aligned} \frac{\partial \rho_e E_e r}{\partial t} + \frac{\partial (\rho_e u_{er} H_e + q_{er}) r}{\partial r} + \frac{\partial (\rho_e u_{ez} H_e + q_{ez}) r}{\partial z} \\ = \left( \frac{j^2}{\sigma} - E_l - E_d < \sigma v > n_e n_{H_2} - E_i \dot{n}_e - \dot{R} \right) r. \quad (23) \end{aligned}$$

Here  $\frac{j^2}{\sigma}$  represents heating due to ohmic dissipation,  $\dot{R}$  is the radiative loss, and the total energy and enthalpy are given by

$$E_e = \frac{3}{2} R_e T_e + \frac{1}{2} u_e^2 \quad (24)$$

and

$$H_e = E_e + R_e T_e. \quad (25)$$

The required electron velocities are extracted from the local current density.

The final equation required for closure of the set is the equation of state:

$$p = \sum_j p_j = \sum_j n_{gj} k T_g + n_e k T_e. \quad (26)$$

## 2.3 Dissociation and Ionization

The nonequilibrium dissociation rate  $\dot{n}_H$  is derived by following the procedure and nomenclature of Biasca[9] for collisions of heavy species. Accordingly, this rate is given by

$$\begin{aligned} \dot{n}_H = A \hat{N} T_g^n \exp \left( -\frac{B}{RT_g} \right) (\hat{m}_H \sigma_H + \hat{m}_{H_2} \sigma_{H_2}) \\ \times \left[ \sigma_{H_2} - \frac{\hat{R} T_g}{K_p(T_g)} \sigma_H^2 \right], \quad (27) \end{aligned}$$

where  $\hat{N}$  is Avogadro's number,  $K_p$  is the equilibrium constant in terms of partial pressures, the  $\sigma_j$ s are the species molar concentrations, and the appropriate constants for hydrogen are listed in Table 1[10]. Dissociation by  $e - H_2$  collisions is represented by the second term on the right-hand side of Eqn. 7, where the reaction rate coefficient  $< \sigma v >$  as a function of  $T_e$  is taken from Janev et al.[11].

Table 1: Constants for the Hydrogen Dissociation Rate Equation

Constant	Value
A ( $m^3/mole - s$ )	$5.5 \times 10^{13}$
B (J/mole)	435,600
n	-1
$\hat{m}_H$	5
$\hat{m}_{H_2}$	2

For ionization, the finite production rate is given by the generalized model of ionization and three-body recombination[12] as modified by Sheppard[13]:

$$\dot{n}_e = R n_e (S n_H - n_e^2) \quad (28)$$

$$S = \left( \frac{2\pi m_e k T_e}{h^2} \right)^{\frac{1}{2}} e^{-\frac{U_i}{k T_e}} \quad (29)$$

$$R = 6.985 \times 10^{-42} \exp \left( \frac{(\ln \frac{T_e}{1000} - 4.0833)^2}{0.8179} \right) \quad (30)$$

## 2.4 Transport Properties

Because of the multi-component nature of the gas in an electrothermal arcjet, even with hydrogen as a propellant, the equations for the transport properties become quite complex. Since data are more

readily available for hydrogen in the form of collision integrals, a formulation of the transport coefficients based on these integrals rather than on collision cross-sections is implemented. The kinetic theory of multicomponent gases has been rigorously applied to the calculation of transport coefficients by Curtiss and Hirschfelder[14], and the formulation here follows their work.

For the electrical conductivity, a first order approximation by Grier[15] to the rigorous kinetic theory has been chosen for use in this research:

$$\sigma = \frac{\sigma_0}{1 - \Delta_e} \quad (31)$$

$$\sigma_0 = \frac{3}{16} \sqrt{\frac{2}{\pi m_e k T_e}} \times \frac{z_H + e^2}{z_H + \bar{\Omega}_{e-H}^{(1,1)} + z_H \bar{\Omega}_{e-H}^{(1,1)} + z_H \bar{\Omega}_{e-H}^{(1,1)}}, \quad (32)$$

where the  $z_j$  are mole fractions and the  $\bar{\Omega}_{ij}$  are average effective collision integrals. The variable  $\Delta_e$  is a more complicated function of mole fractions and additional collision integrals.

The gas coefficient of viscosity is calculated based on a mean free path mixture formula, which is a function of the collision integrals and the species number densities and pure viscosities[12]:

$$\begin{aligned} \mu_g = & \frac{n_{H_2} \mu_{H_2}}{n_{H_2} + n_H \sqrt{\frac{2}{3} \frac{\bar{\Omega}_{H_2-H}^{(2,2)}}{\bar{\Omega}_{H_2-H_2}^{(2,2)}}}} \\ & + \frac{n_H \mu_H}{n_H + n_{H_2} \sqrt{\frac{4}{3} \frac{\bar{\Omega}_{H-H}^{(2,2)}}{\bar{\Omega}_{H-H_2}^{(2,2)}}} + 2n_H \frac{\bar{\Omega}_{H-H}^{(2,2)}}{\bar{\Omega}_{H-H}^{(2,2)}}} \\ & + \frac{n_H + \mu_{H+}}{n_{H+} + 2n_H \frac{\bar{\Omega}_{H-H+}^{(2,2)}}{\bar{\Omega}_{H-H+}^{(2,2)}}}, \quad (33) \end{aligned}$$

where the pure viscosities are given to lowest order by

$$\mu_j = 2.6693 \times 10^{-26} \frac{(M_j T_g)^{\frac{1}{2}}}{\bar{\Omega}_{jj}^{(2,2)}}. \quad (34)$$

Electron and heavy species thermal conductivity coefficients are calculated based on similar mean free path arguments and mixture rules, and the pure thermal conductivities are given by Eucken's relation

$$\kappa_j = \frac{15}{4} \frac{\hat{R}}{M_j} \mu_j \left( \frac{4}{15} \frac{\hat{c}_v}{\hat{R}} + \frac{3}{5} \right), \quad (35)$$

where  $\hat{c}_v$  equals  $\frac{3}{2} \hat{R}$  for monatomic gases and  $\frac{5}{2} \hat{R}$  for diatomic gases.

Collision integrals required in the calculation of transport coefficients are interpolated as a function

of temperature from data by Belov[16], Grier[15], and Vanderslice et al.[17]. The accuracy of the above approximate formulas for the transport coefficients was verified by comparison to previous, more detailed work for hydrogen in thermal and ionizational equilibrium.

### 3 Numerical Method

#### 3.1 Integration Scheme

The numerical method used in this research has been previously implemented in numerical simulations of MPD thrusters with coaxial geometries[18]. The governing fluid equations are numerically integrated using MacCormack's explicit node-based method. This predictor-corrector method is second order accurate in both time and space, and it has proved an excellent means of solving the compressible Navier-Stokes equations for a variety of conditions. The explicit nature of the algorithm allows for simpler coding than an implicit scheme because of the complex nature of the source terms and boundary conditions, and it also provides a means of obtaining time-accurate solutions.

An empirical stability formula developed by MacCormack and Baldwin[19] is utilized to calculate the integration time step, which is then multiplied by a fractional coefficient to account for the effect of source terms and nonlinearities. The time accuracy of the solution is maintained so long as the same time step is used at all computational grid locations. Although MacCormack's method contains some inherent dissipation, additional numerical smoothing is required in order to damp unwanted numerical oscillations in the fluid equations. Consequently, simple 2nd and/or 4th order smoothing terms are applied to each equation as necessary, based on the method of Kutler, Sakell, and Aiello[20].

The electric potential equation, being predominantly elliptic in nature, is solved by iteration using a successive overrelaxation (SOR) technique. Since the physical grid is nonuniform in order to closely represent the geometry of the actual arcjet being modeled, the governing equations are transformed into natural coordinates and then solved on a uniform Cartesian computational mesh. The physical grid used for the simulations presented in this paper is shown in Figure 2.

#### 3.2 Boundary Conditions

The conditions at the inlet of the computational domain are postulated to be essentially those of a flow which has just been injected into the thruster plenum by a large number of evenly spaced jets. The

flow is therefore assumed to be subsonic and parallel to the thruster walls. A fraction of the total inlet velocity, typically 30-50%, is specified as being in the azimuthal direction in order to simulate an injected swirl. The mass flow rate and total enthalpy are specified based on the particular run parameters, and the ionization fraction is set to a small value, typically  $1 \times 10^{-6}$ . The density is obtained from a downwind finite difference approximation of the overall continuity equation, and the axial velocity is then found from the specified mass flow rate. The inlet electron temperature is set equal to that of the next inside point, and the heavy species temperature is then found from the total enthalpy. No current is allowed to leave the domain at the inlet ( $j_z = 0$ ).

The boundary conditions at the outlet of the thruster depend on whether the exit flow is subsonic or supersonic. In both cases the electron temperature is set equal to that of the next inside point, and no current may pass beyond the exit plane. If the flow is supersonic at a point on the exit plane, then the remaining quantities are extrapolated from their values at the preceding two grid points of the mesh. If the flow is subsonic, then the exit pressure is set equal to a small value representing near-vacuum conditions and the density and axial velocity are given by Riemann invariants. The remaining quantities at a subsonic outlet are then calculated as in the supersonic case.

For those boundary points lying beyond the tip of the cathode on the line of symmetry ( $r = 0$ ), the radial and azimuthal flow velocities are set equal to zero and a zero radial gradient is imposed on the remaining quantities.

Flow boundary conditions at the thruster walls include viscous no-slip conditions for the axial and radial fluid velocities. The electron temperature is set equal to that of the next inside grid point, and the heavy species temperature is held constant at 1000°K upstream of the constrictor, increasing linearly to 1200°K at the constrictor exit. This profile was chosen based on experimental and numerical calculations of the anode wall temperature distribution for a reasonable operating range of the German TT1 radiatively-cooled arcjet thruster[21]. On the cathode the wall temperature is allowed to increase to a maximum of 2000°K at the tip. For the boundary condition on electron density at each electrode, a balance is postulated between the flux of ions arriving at the sheath edge by ambipolar diffusion and the flux of ions arriving at the wall by virtue of their thermal energy at the Bohm velocity ( $v_B$ )[22]:

$$D_a \frac{dn_e}{dy} = 0.37 n_e v_B, \quad (36)$$

where

$$v_B = \sqrt{\frac{k(T_e + T_g)}{m_g}}. \quad (37)$$

This boundary condition neglects the voltage drops present in the non-neutral plasma sheath. Also omitted is the dependence of the thermionic emission of electrons at the cathode on the cathode wall temperature. Application of the perpendicular overall momentum equation at the walls provides the approximate condition

$$\frac{dp}{d\tilde{n}}|_{\text{wall}} = 0, \quad (38)$$

where inertial and viscous terms have been neglected.

The boundary condition on the wall electric potential is that there is no current perpendicular to an insulating section, and the potential on the anode is set equal to a fixed but arbitrary voltage. For numerical reasons, anode current attachment is restricted to that portion of the outer wall downstream of the constrictor exit. On the cathode tip, a uniform axial current density is prescribed which sums to the specified total current; the potential at the cathode is then chosen so as to maintain this current level. A cathode voltage drop equal to the ionisation potential plus one half of the dissociation potential of the gas is added to the calculated voltage in order to account for the model's neglect of the cathode sheath region. In addition, an anode voltage drop is subtracted from the calculated voltage in order to account for the anode sheath region. A negative potential gradient is required in this sheath in order to turn back excess electrons since the extracted current is much less than the random thermal flux of electrons to the anode wall ( $j_{\text{anode}} \ll \frac{1}{4} n_e \bar{c}_e$ ). This voltage drop is given by

$$\Delta V_a = \frac{kT_e}{e} \left[ \ln \left( \frac{\sqrt{m_i/m_e}}{0.61 \sqrt{2\pi}} \right) - \ln \left( 1 + \frac{j}{0.61 n_e \sqrt{\frac{kT_a}{m_i}}} \right) \right]. \quad (39)$$

### 3.3 Procedure

Once the initial conditions of the flow have been specified, the solution is calculated numerically as follows. First, the timesteps are calculated for the overall and heavy species equations at all grid points from stability criteria. The most restrictive time step is chosen as the time interval for the current integration step, and these equations are integrated

according to MacCormack's method. Next, the electron density and energy equations are integrated based on their individual stability restrictions while maintaining consistency with the previously determined time interval. The electron equations are integrated separately because the associated stability criteria can be up to 30 times more restrictive than for the overall flow equations. Finally, the electric potential equation is relaxed a specified number of iterations. This system of equations is then repeatedly integrated until the solution is considered converged. Computations were performed on a variety of machines, including DECStation 5000s, IBM RS-6000s, Silicon Graphics Iris Indigos, and Cray X-MPs.

## 4 Results

Results have been achieved for comparison to the German TT1 radiation-cooled arcjet thruster at a number of operating points. For the baseline case of  $I = 100A$  and  $\dot{m} = 0.1g/s$ , Table 2 compares bulk results of the simulation to experimental measurements and Figures 3 through 10 show line and contour plots of representative quantities. There is excellent agreement in the voltage between predicted and experimental results, and good agreement (within 7%) in the thrust and specific impulse. The accuracy in voltage prediction shows that the model is accurately modeling arc growth, electrical conductivity, and current attachment given the assumptions we have made regarding electrode sheath voltage drops. A major reason for the discrepancy in thrust prediction is that the specified inlet gas temperature is probably too high. Recent modeling of the anode heat balance in this thruster has shown that the inlet temperature for the baseline case is about  $875^\circ K$  rather than  $1000^\circ K$  as specified in the present boundary conditions. Since the thrust scales as the plenum total pressure, which scales as  $\sqrt{T_0}$ , a 12% decrease in the inlet gas temperature could translate into a 6% reduction in thrust. This would bring the simulation results into very close agreement with the experimental data.

Table 2: Comparison of Predicted and Experimental Results for Baseline Case

	Predicted	Experiment
Voltage (V)	114	112
Power (kW)	11.4	11.2
Thrust (N)	1.01	0.94
Specific Impulse (s)	1030	960
Efficiency	0.442	0.395

Figure 3 shows an axial line plot of the electric potential from the cathode tip to the anode attachment zone. The near-cathode voltage drop  $\Delta V_c$  is composed of a 15.8V drop assigned to the cathode sheath ( $V_i + \frac{1}{2}V_d$ ) and an 8V drop calculated in the first few gridpoints downstream of the tip. The near-anode voltage drop  $\Delta V_a \approx 15V$  is composed of a 22V drop captured by the simulation and a -7V drop associated with the electron-repelling sheath. This total anode voltage drop is associated with the net deposition of energy into the anode block by heavy species heat conduction and by the impingement of current-carrying electrons. Assuming that the energy transferred per unit area is of the form

$$\dot{E}_{anode} = -k_g \frac{dT_g}{d\hat{n}} + u_{en} \left[ \frac{5}{2}p_e + \frac{1}{2}\rho_e u_e^2 + E_i n_e \right], \quad (40)$$

using the results of the baseline flow simulation yields an equivalent voltage of 14.5V for this deposited power, which agrees well with the  $\Delta V_a$  seen in the potential profile.

Current streamlines are plotted in Figure 4. In this case, the bulk of the current attaches within the first quarter of the nozzle, with a peak just downstream of the constrictor exit. The flow becomes fully ionized along the centerline immediately downstream of the cathode tip and remains so through the first part of the nozzle expansion, beyond which there is some recombination (Figure 5). The boundary of the partially ionized region grows to approximately 50% of the channel by the constrictor exit, and this region is essentially entrained in the flow throughout the nozzle. The primary heating mechanism is ohmic dissipation, which peaks locally along the constrictor centerline and just beyond the constrictor exit near the anode. This is evidenced by the local maxima in electron temperature in these regions (Figure 6).

Within the highly ionized region of the arc in the constrictor, collisional energy transfer between electrons and heavy species raises the gas temperature to  $20,000 - 30,000^\circ K$ , or nearly the same temperature as the electrons. Outside of the arc the flow remains cold, at a temperature approximately equal to the anode wall temperature. This outer flow remains essentially uncoupled from the hot core flow, as pictured in Figure 7. The flow velocity is also uncoupled, although viscous forces eventually wash out the separation in the nozzle expansion (Figure 8). Since the pressure is nearly uniform in the radial direction (Figure 9), rapid acceleration of the core flow occurs throughout the low pressure region of the arc in the constrictor. Once the bulk of the pressure work has been utilized in the expansion process, however, viscous forces arising from steep velocity gradients in



Table 3: Average Ratio of Terms to Dominant Term in Electron Energy Equation

TERM	ARC	OUTER
Radial Convection	0.338	0.423
Axial Convection	0.528	0.444
Radial Conduction	0.400	0.216
Axial Conduction	0.007	0.056
Ohmic Dissipation	0.508	0.504
Transfer to Heavy Species	0.023	0.069
Net Dissociation	0.006	0.007
Net Ionization	0.345	0.207
Radiation	0.001	0.001

Table 4: Average Ratio of Terms to Dominant Term in Electron Density Equation

TERM	ARC	OUTER
Radial Divergence	0.604	0.636
Axial Divergence	0.830	0.788
Radial Ambipolar Diffusion	0.512	0.212
Axial Ambipolar Diffusion	0.019	0.009
Net Ionization	0.240	0.301

the central core decelerate the flow significantly in the nozzle expansion. Both the inner and outer flows accelerate smoothly through sonic velocity at and just beyond the constrictor exit. Figure 10 shows Mach number contours for the baseline case arcjet simulation. Interestingly, due to the large radial gradients in temperature, composition, and velocity, the peak Mach number occurs in the interior region of the flow rather than at the centerline.

Simulating the current attachment at the anode realistically and self-consistently has been a major difficulty in previous arcjet simulations. The effectiveness of this model in simulating this region is due to the incorporation of separate energy equations for the heavy species and electrons and to the use of nonequilibrium dissociation and ionization finite rate equations. To illustrate this point, Tables 3, 4, and 5 compare the relative importance of effects in the electron energy, electron density, and atomic hydrogen density equations, respectively. Each table lists the ratio of every term in the equation to the dominant term at each grid location, averaged over all grid points. The flow is divided into two regions for this purpose, the arc core ( $\alpha > 0.01$ ) and the outer flow ( $\alpha < 0.01$ ).

With respect to the electron energy equation, Table 3 shows that ohmic dissipation is an important source of energy both inside and outside the arc. This leads to electron temperatures as high as  $20,000^\circ K$  in the anode attachment zone of the outer flow, much higher than the  $1000 - 2000^\circ K$  temper-

Table 5: Average Ratio of Terms to Dominant Term in Atomic Hydrogen Density Equation

TERM	ARC	OUTER
Radial Divergence	0.545	0.664
Axial Divergence	0.487	0.910
Radial Diffusion	0.265	0.001
Axial Diffusion	0.016	0.000
Net Dissociation ( $H - H_2$ )	0.131	0.019
Net Dissociation ( $e - H_2$ )	0.157	0.048
Net Ionization	0.332	0.139

atures which would be calculated by a model with only one energy equation. Figure 11 illustrates this result by comparing radial profiles of the electron and heavy species temperatures at an axial location 0.25mm downstream of the constrictor exit. This elevated electron temperature then produces enough electron impact dissociation and ionization to create the necessary charge carriers for electrical conduction between the outer arc boundary and the anode. Tables 4 and 5 show the importance of these nonequilibrium dissociation and ionization processes in the electron and atomic hydrogen continuity equations. Radial ambipolar diffusion also plays a role in moving ions and electrons outward from the arc into the surrounding cooler gas flow. This process is evidenced by radial profiles of the ambipolar diffusion and net ionization terms in the electron density equation, shown in Figure 12 near the anode wall in the current attachment region.

Several other cases have been run to evaluate the model's effectiveness in predicting arcjet performance over a range of parameters. Figure 13 compares simulation predictions of specific impulse for the TT1 thruster at three different applied currents for a mass flow rate of 0.1g/s. Predicted specific impulse is approximately 5-10% higher than experimental data, but should come into closer agreement when the results of the aforementioned anode heat balance model are incorporated into the arcjet flow model. Table 6 compares predicted discharge voltages with experimental measurements for the three cases presented in Figure 13. Voltage predictions from the arcjet simulation consistently fall within 2% of experimental results, demonstrating the code's effectiveness in consistently modeling the electric arc characteristics of this arcjet thruster. The negative slope of the V-I relationship is also captured.

## 5 Conclusions

A detailed, multifluid, viscous model has been developed to simulate the nonequilibrium gasdynamic flow in an electrothermal arcjet. The model is im-

Table 6: Comparison of Discharge Voltages for the Cases in Figure 8

Case	Numerical	Experiment
$I = 60A, \dot{m} = 0.1g/s$	117	117
$I = 100A, \dot{m} = 0.1g/s$	114	112
$I = 130A, \dot{m} = 0.1g/s$	112	110

plemented on a nonuniform mesh fixed to experimental thruster dimensions, and the equations are solved using MacCormack's method and successive over-relaxation. Numerical results are achieved for hydrogen propellant, and calculated thrust, specific impulse, and discharge voltage compare well with experimental data for the German TT1 arcjet thruster. The internal two-dimensional structure of the flow is revealed, particularly with respect to arc development and anode attachment, and the two-temperature nature of the flow is evident. In particular, the integration of a separate electron energy equation has shown that stable attachment of the arc to the anode occurs by increased local ohmic heating coupled with nonequilibrium dissociation and ionization in the flow between the arc core and the anode wall.

Additional cases are being run at this time to obtain more data points for comparison to experiment for a variety of operating points and thruster configurations. Also, an anode heat balance model has been developed to more accurately calculate the anode wall temperature for this class of radiation-cooled arcjet thrusters. This model is currently being integrated with the interior flow model in order to produce more fully consistent solutions. The simulation may then be used to identify ways to improve overall arcjet thruster performance.

## Acknowledgements

This research was supported by a National Defense Science and Engineering Graduate Fellowship administered by the U.S. Army Research Office.

## References

- [1] R. Spurrett and R.A. Bond, "Modelling Arcjet Thruster Performance", IEPC 91-110, AIDAA/AIAA/DGLR/JSASS 22nd International Electric Propulsion Conference, Viareggio, Italy, October 1991.
- [2] B. Glocker, H.O. Schrade, and P.C. Sleziona, "Numerical Prediction of Arcjet Performance", AIAA 90-2612, AIAA/DGLR/JSASS 21st International Electric Propulsion Conference, Orlando, July 1990.
- [3] B. Glocker and M. Auweter-Kurtz, "Numerical and Experimental Constrictor Flow Analysis of a 10kW Thermal Arcjet", AIAA 92-3835, AIAA/SAE/ASME/ASEE 28th Joint Propulsion Conference, Nashville, July 1992.
- [4] A. Sakamoto, *Simplified Modeling and Analysis of Arcjet Thrusters*, S.M. Thesis, Massachusetts Institute of Technology, February 1993.
- [5] M. Andrenucci et al., "Development of a Computer Programme for the Analysis of Arcjet Nozzles", IEPC 91-113, AIDAA/AIAA/DGLR/JSASS 22nd International Electric Propulsion Conference, Viareggio, Italy, October 1991.
- [6] G.W. Butler and D.Q. King, "Single and Two Fluid Simulations of Arcjet Performance", AIAA 92-3104, AIAA/SAE/ASME/ASEE 28th Joint Propulsion Conference, Nashville, July 1992.
- [7] R. Rhodes and D. Keefer, "Modeling Arcjet Space Thrusters", AIAA 91-1994, AIAA/SAE/ASME/ASEE 27th Joint Propulsion Conference, Sacramento, June 1991.
- [8] R. Rhodes and D. Keefer, "Comparison of Model Calculations With Experimental Data From Hydrogen Arcjets", IEPC-91-111, AIDAA/AIAA/DGLR/JSASS 22nd International Electric Propulsion Conference, Viareggio, Italy, October 1991.
- [9] R.J. Biasca, *Chemical Kinetics of Scramjet Propulsion*, S.M. Thesis, Massachusetts Institute of Technology, September 1988.
- [10] R.C. Rogers and C.J. Schexnayder Jr., "Chemical Kinetic Analysis of Hydrogen-Air Ignition and Reaction Times", NASA Technical Paper 1856, 1981.
- [11] R.K. Janev, W.D. Langer, K. Evans, and D.E. Post, *Elementary Processes in Hydrogen-Helium Plasmas*, Springer-Verlag, New York, 1987.
- [12] M. Mitchner and C. Kruger, *Partially Ionized Gases*, John Wiley and Sons, New York, 1973.
- [13] E.J. Sheppard, *Nonequilibrium Ionization in Electromagnetic Accelerators*, Ph.D. Thesis, Massachusetts Institute of Technology, 1993.
- [14] C.F. Curtiss and J.O. Hirschfelder, "Transport Properties of Multicomponent Gas Mixtures", *Journal of Chemical Physics*, Vol.17, June 1949, p.550-5.

- [15] N.T. Grier, "Calculation of Transport Properties of Ionizing Atomic Hydrogen", NASA TN D-3186, April 1966.
- [16] V.A. Belov, "Viscosity of Partially Ionized Hydrogen", High Temperature, Vol.5, 1967, p.31-6.
- [17] J.T. Vanderslice, S. Weissman, E.A. Mason, and R.J. Fallon, "High-Temperature Transport Properties of Dissociating Hydrogen", Physics of Fluids, Vol.5, No.2, February 1962, p.155-64.
- [18] S.A. Miller and M. Martinez-Sanchez, "Viscous and Diffusive Effects in Electrothermal and MPD Arcjet Thrusters", IEPC 91-060, AIDAA/AIAA/DGLR/JSASS 22nd International Electric Propulsion Conference, Viareggio, Italy, October 1991.
- [19] R.W. MacCormack and B.S. Baldwin, "A Numerical Method for Solving the Navier-Stokes Equations with Application to Shock-Boundary Layer Interactions", AIAA 75-1, AIAA 13th Aerospace Sciences Meeting, Pasadena, January 1975.
- [20] P. Kutler, L. Sakell, and G. Aiello, "On the Shock-On-Shock Interaction Problem", AIAA 74-524, AIAA 7th Fluid and Plasma Dynamics Conference, Palo Alto, June 1974.
- [21] B. Glocker and M. Auweter-Kurtz, "Radiation Cooled Medium Power Arcjet Experiments and Thermal Analysis", AIAA 92-3834, AIAA/SAE/ASME/ASEE 28th Joint Propulsion Conference, Nashville, July 1992.
- [22] J.J. Wang, *Electrodynamic Interactions Between Charged Space Systems and the Ionospheric Plasma Environment*, Doctoral Thesis, Massachusetts Institute of Technology, June 1991.

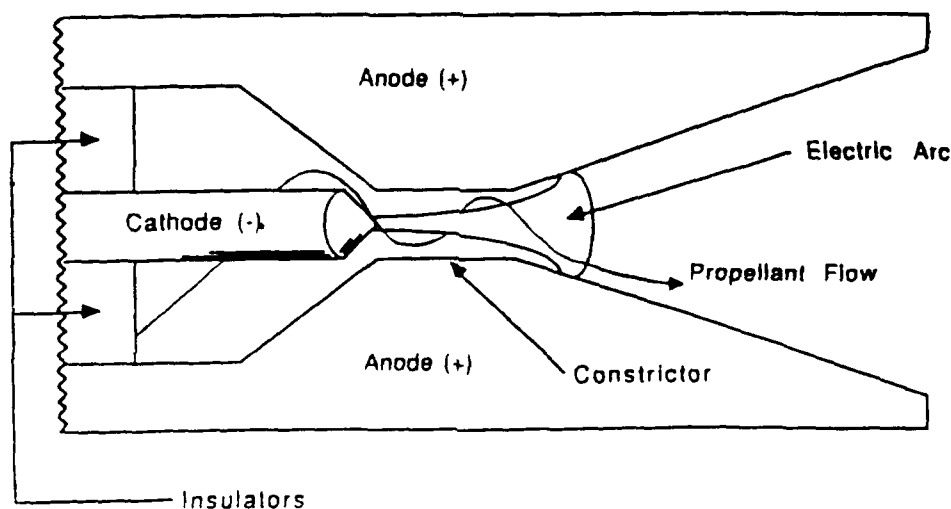


Figure 1: Electrothermal Arcjet Diagram

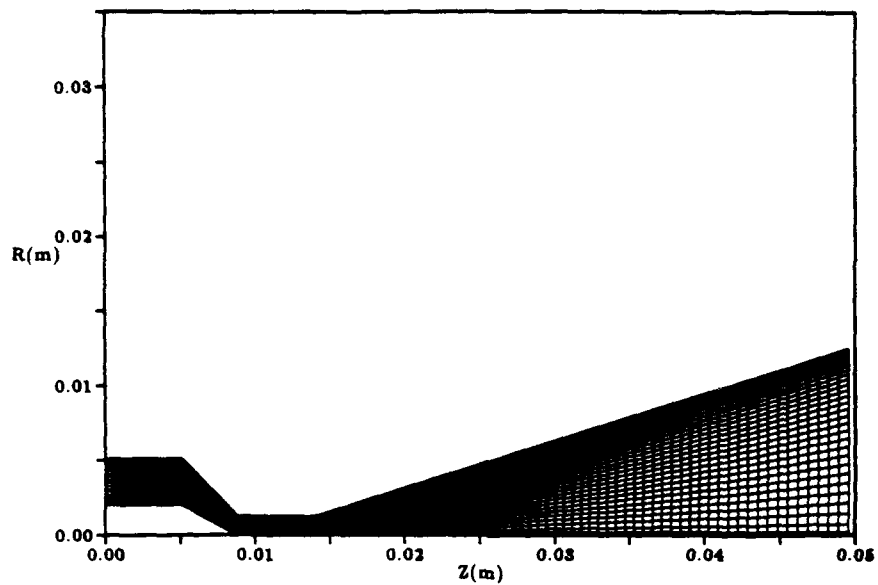


Figure 2: Physical Grid for Arcjet Simulations

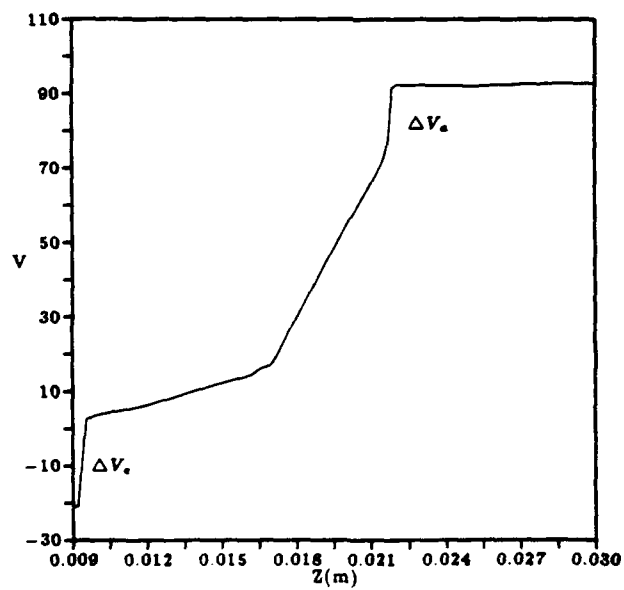


Figure 3: Electric Potential Axial Profile for the Baseline Case Arcjet Simulation

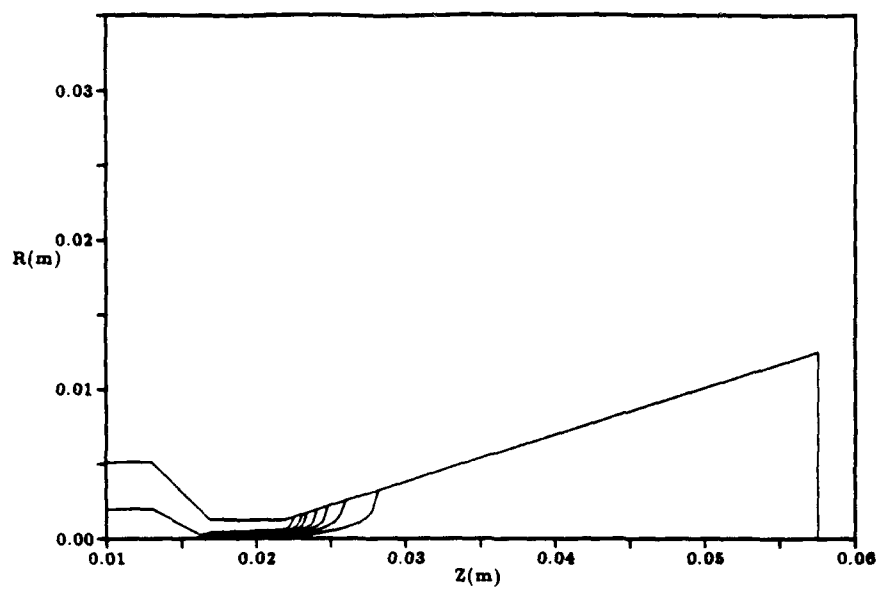


Figure 4: Enclosed Current Contours for the Baseline Case of  $I = 100A$ ,  $\dot{m} = 0.1g/s$

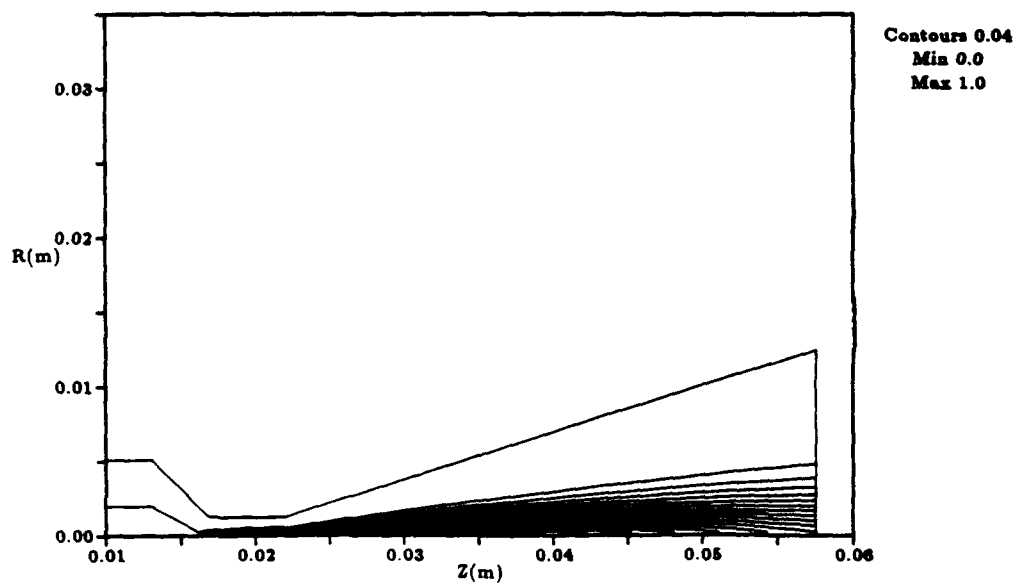


Figure 5: Ionization Fraction Contours for the Baseline Case of  $I = 100A$ ,  $\dot{m} = 0.1g/s$

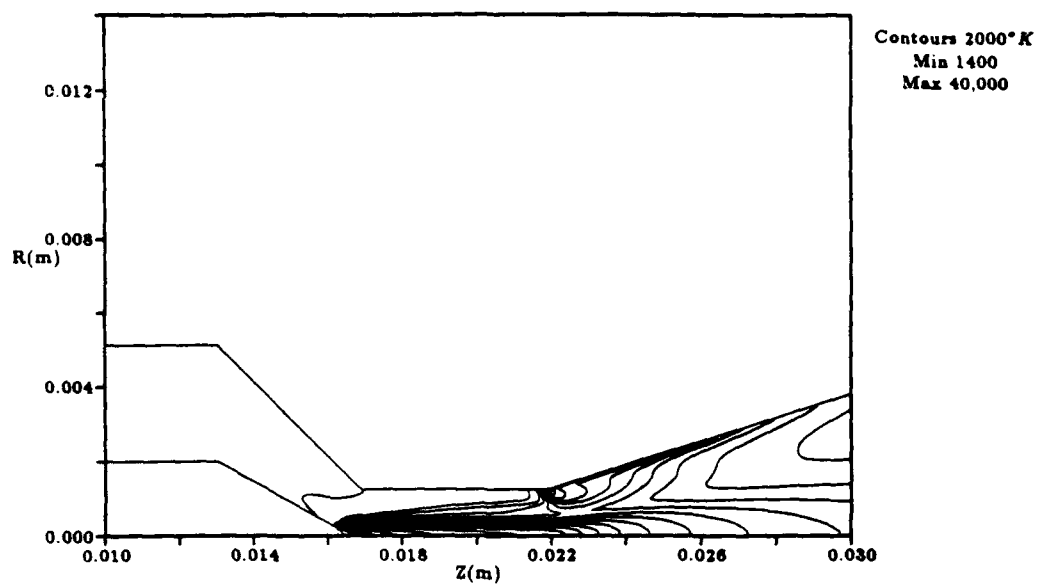


Figure 6: Electron Temperature Contours for the Baseline Case of  $I = 100A$ ,  $\dot{m} = 0.1g/s$

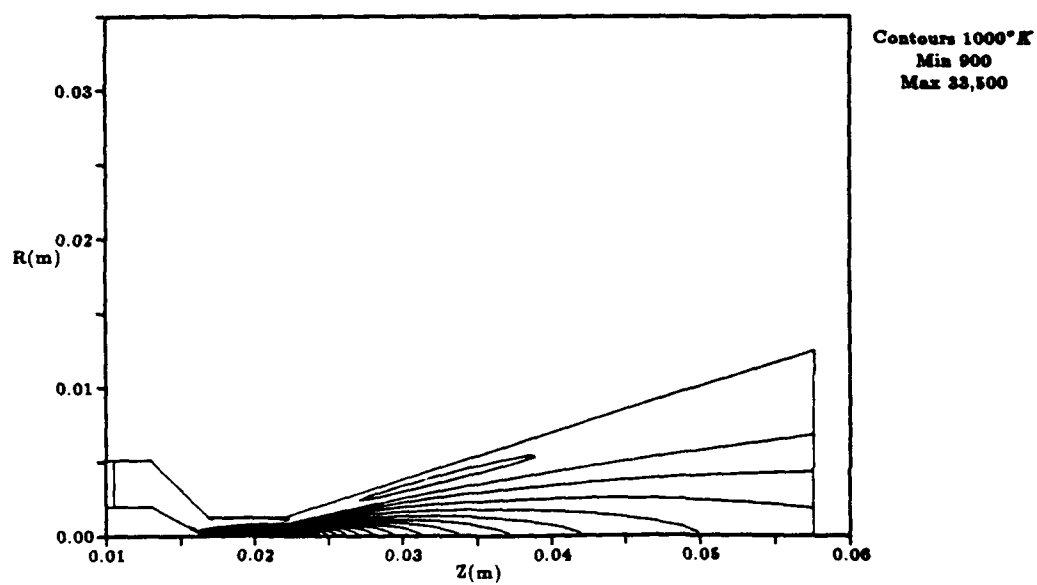


Figure 7: Gas Temperature Contours for the Baseline Case of  $I = 100A$ ,  $\dot{m} = 0.1g/s$

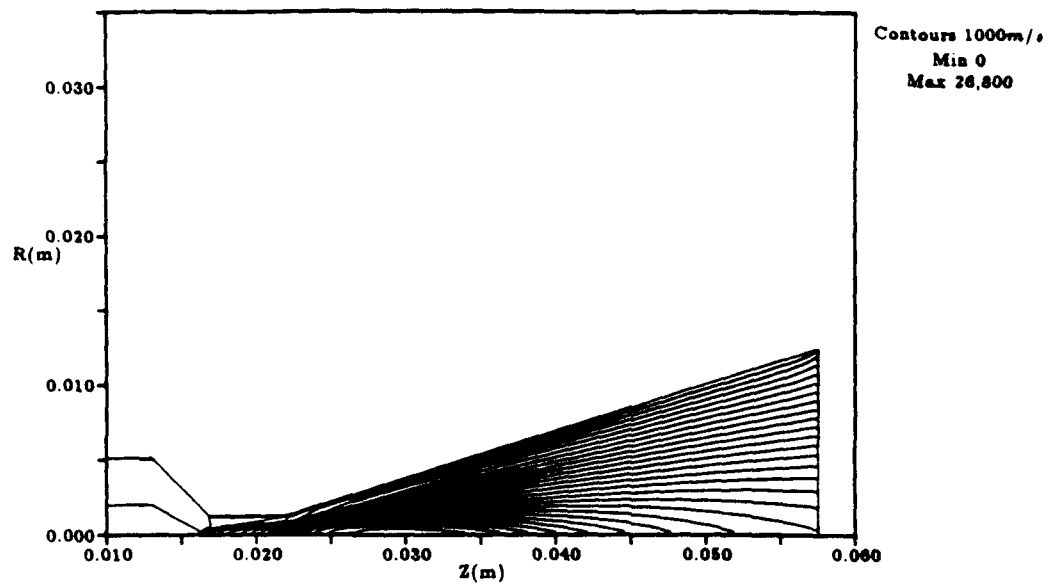


Figure 8: Axial Velocity Contours for the Baseline Case of  $I = 100A$ ,  $\dot{m} = 0.1g/s$

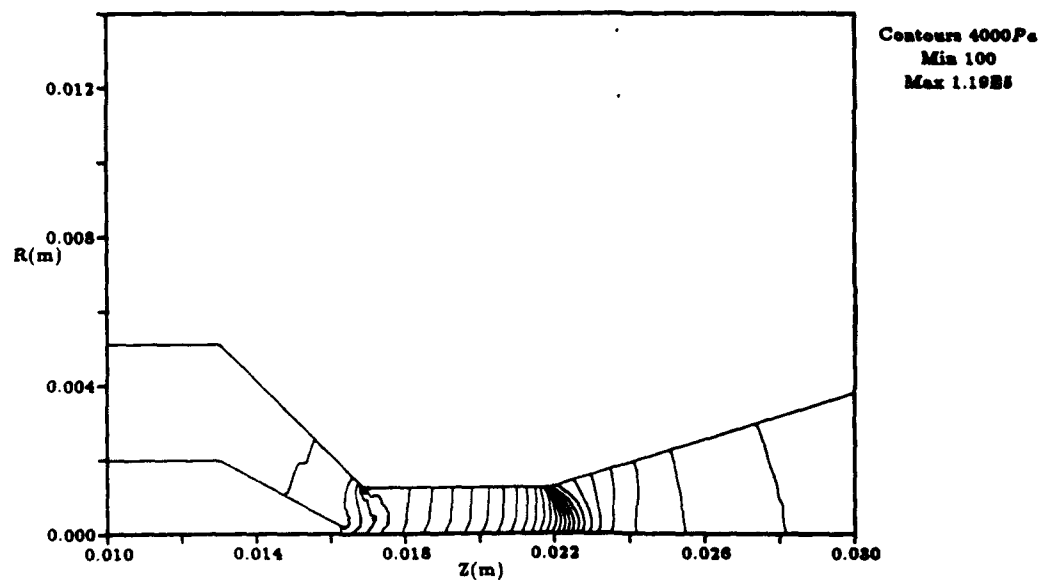


Figure 9: Pressure Contours for the Baseline Case of  $I = 100A$ ,  $\dot{m} = 0.1g/s$

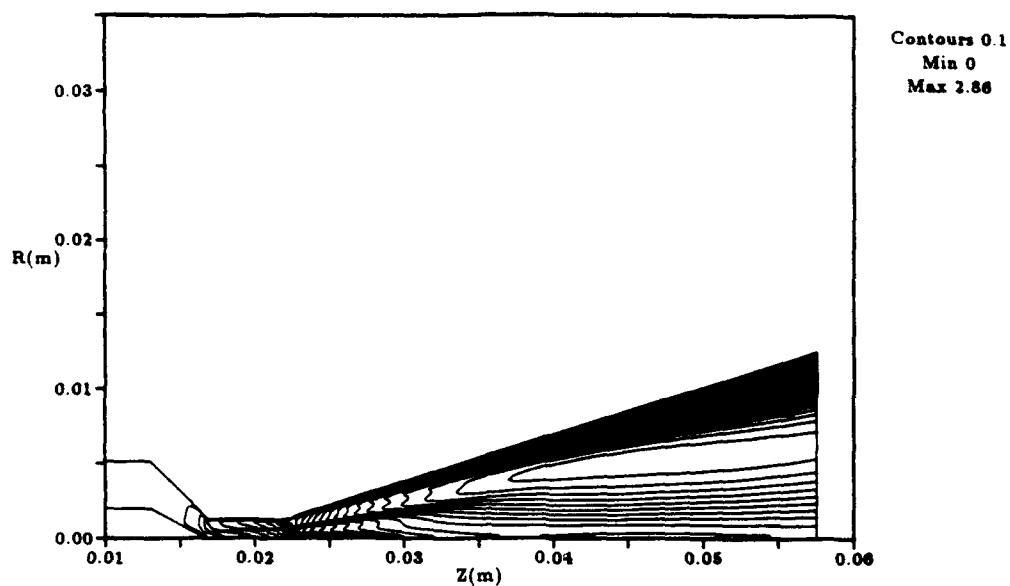


Figure 10: Mach Number Contours for the Baseline Case of  $I = 100A$ ,  $\dot{m} = 0.1g/s$

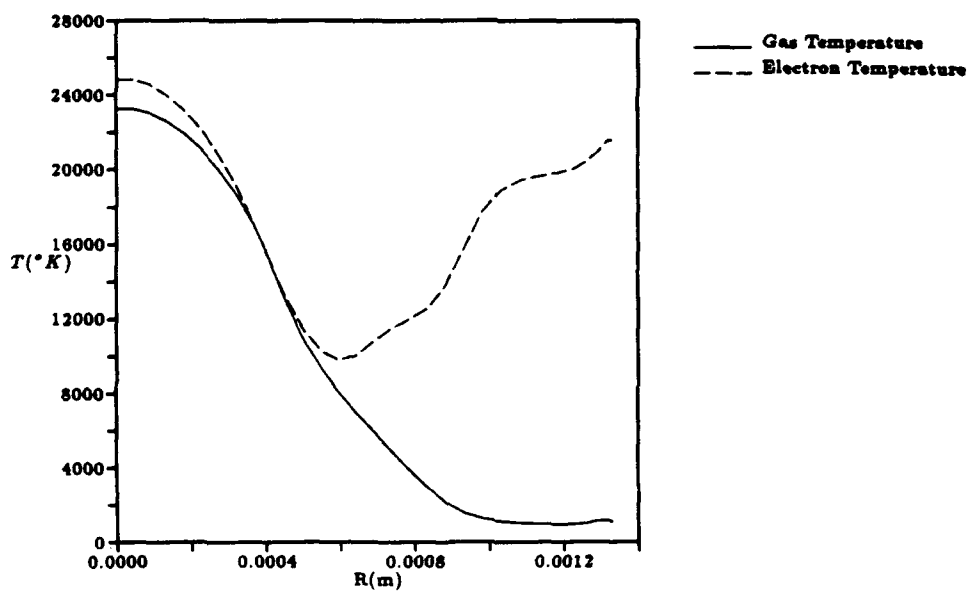


Figure 11: Radial Profiles of Electron and Heavy Species Temperatures 0.25mm Downstream of the Constrictor Exit



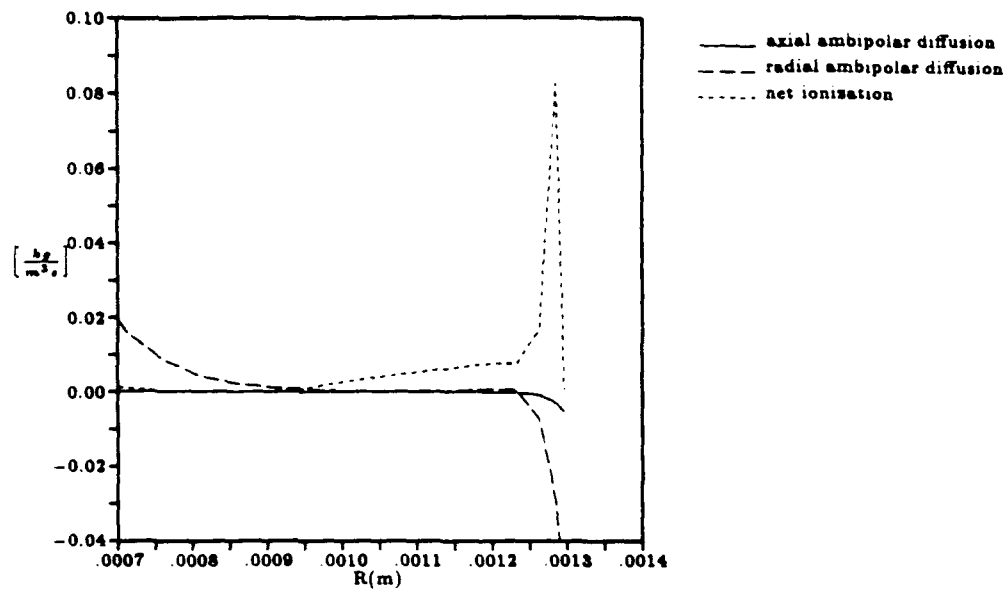


Figure 12: Radial Profiles of Some Terms in the Electron Density Equation in the Current Attachment Region Just Downstream of the Constrictor Exit

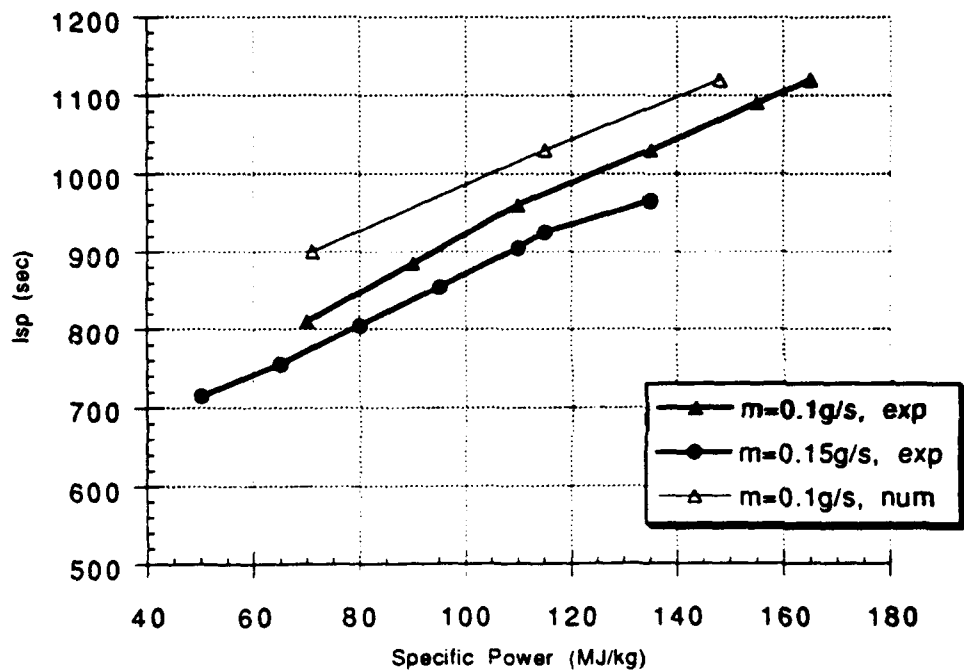


Figure 13: Predicted  $I_{sp}$  Compared to Experimental Data, German TT1 Radiation-Cooled Hydrogen Arcjet



**AIAA 93-2491**

**Transient One Dimensional Numerical  
Simulation of Hall Thrusters**

**C. A. Lentz and M. Martinez-Sanchez**

**Space Power and Propulsion Laboratory**

**Dept. of Aeronautics and Astronautics**

**MIT**

**Cambridge, MA**

**AIAA/SAE/ASME/ASEE**

**29th Joint Propulsion**

**Conference and Exhibit**

**June 28-30, 1993 / Monterey, CA**

# TRANSIENT ONE DIMENSIONAL NUMERICAL SIMULATION OF HALL THRUSTERS

Christopher A. Lentz\* and Manuel Martinez-Sanchez†  
Space Power and Propulsion Laboratory  
Department of Aeronautics and Astronautics  
Massachusetts Institute of Technology, Cambridge, MA

## Abstract

A numerical code for the plasma properties in the acceleration channel of a Hall thruster was written and its results compared with experiments. The model was constructed to help understand the acceleration process in the channel and to relate the axial distributions to thruster performance. Specific to this analysis are the definition of an ion distribution function, careful treatment of the electron energy equation, and momentum transfer between neutrals and ions.

## Nomenclature

(SI units unless noted otherwise)

$A$	Channel cross sectional area
$\alpha$	Ionization fraction
$B$	Magnetic field strength
$c_s$	Random velocity of species $s$
$\bar{c}_s$	Thermal velocity of species $s$
$D$	Diffusion coefficient
$\delta$	Secondary electron emission from the wall
$\Delta t$	Time step
$\Delta z$	Spatial step in the axial direction
$E$	Electric field strength
$e$	Electric charge of proton
$E_i$	Ionization energy
$\eta$	Thrust efficiency
$\eta_a$	Acceleration efficiency
$\eta_n$	Nonuniformity factor
$\eta_u$	Utilization efficiency
$f_s$	Distribution function for species $s$
$F$	Thrust
$\bar{F}_s$	External force p.u. volume on species $s$
$\Gamma_s$	Spitzer logarithm for species $s$
$\gamma$	Ion production cost
$I_a$	Anode current
$I_{sp}$	Specific impulse
$J_s$	Electric current for species $s$
$j_s$	Electric current density for species $s$

$k$	Boltzmann constant
$K_e$	Heat transfer coefficient
$L$	Channel length
$\dot{m}$	Mass flow rate
$\dot{m}_i$	Ion mass flow rate
$m_e$	Electron mass
$m_i$	Ion mass
$n_s$	Particle density for species $s$
$n_i$	Ionization rate
$n_w$	Wall loss rate
$\nu_{sr}$	Collision freq. of species $s$ with species $r$
$\phi$	Electric potential
$\phi_a$	Anode potential
$Q_{in}$	Ion-neutral collision cross section
$q_s$	Electric charge of species $s$
$\vec{q}_s$	Thermal conduction vector for species $s$
$S_2$	Source term for energy equation
$\sigma_i$	Ionization cross section
$T_{no}$	Neutral inlet temperature
$T_s$	Temperature of species $s$
$v_b$	Bohm velocity
$v_s$	Velocity for species $s$
$\bar{v}_s$	Mean mass velocity for species $s$
$W$	Channel width
$\xi_k$	Number of electrons in $k$ th level
$\langle \rangle$	Average value

## Introduction

Hall thrusters are a type of coaxial plasma accelerators. A radial magnetic field and an axial voltage drop between the anode and a cathode are externally applied. (See Figure 1) Neutral gas (typically Xenon or Argon) flows in through slits in the anode. Ionization takes place by electron-neutral collisions and the ions are then accelerated axially by the electric potential. Because ionization takes place throughout the acceleration channel, the ions accelerate to different exit velocities depending upon the potential difference between the location of their birth and the cathode. A cathode downstream of the accelerator releases electrons into the ion stream neutralizing the flow. A fraction of

\*Graduate Student, Member AIAA

†Professor, Member AIAA

these electrons travel both azimuthally due to the  $\vec{E} \times \vec{B}$  fields and drift axially toward the anode.

The numerical code developed here solves a set of differential equations derived from taking moments of the Boltzmann equation, Ohm's Law and an ion distribution function. For the code, an ion distribution function is formulated and integrated to generate axial ion density and mean velocity profiles. Time dependent equations for neutral continuity and electron temperature are formulated. Additional equations for axial current conservation and electric field are used in the code.

The acceleration channel is discretized into a fixed grid of differential segments. Axial distributions are initialized onto the grid at the beginning of the solution routine. A convective-diffusive, finite difference scheme is used to integrate the set of equations in time until they converge to a steady state solution. From the numerical solution, the thrust and efficiency of the thruster may be calculated.

Assumptions used in the code include plasma quasi-neutrality throughout the accelerator and ambipolar loss of electron-ion pairs to the walls of the channel. Additionally, in this one dimensional study, the plasma is assumed uniform in the radial and azimuthal directions.

For the cases studied, the geometry and operational conditions of an experimental thruster are reproduced in the code. The results produced from the numerical analysis are then compared with the experimental results from research performed in Japan. [1]

This paper demonstrates that the one-dimensional numerical code can be a useful design and plasma analysis tool. The method is versatile and simple enough that multiple analysis on various thruster parameters (different anode currents, mass flows, etc.) or different geometries can be examined in a relatively short time.

### Physical Model

The model for the thruster includes seven primary equations describing the unknown variables - neutral and electron (or ion) density, neutral, ion and electron velocity, electron temperature and electric field. From these values, the performance characteristics of the thruster may be calculated.

Several assumptions are used to facilitate the computations in this analysis. The first is that quasi one dimensional flow exists resulting in no variations in the radial or azimuthal directions. Additionally, it is assumed that only one component of electric and magnetic fields exists as illustrated in Figure 1. Finally, the flow is

assumed to be quasi neutral in the acceleration channel.

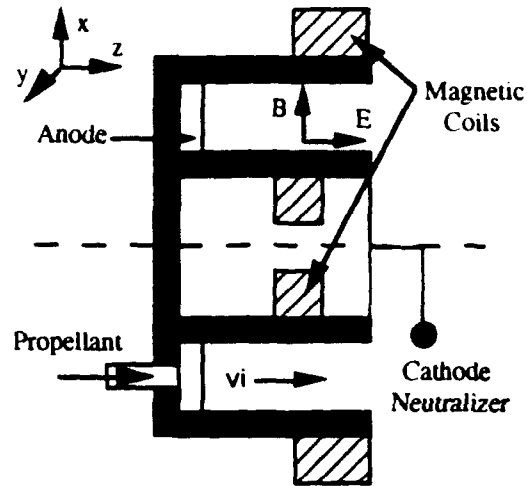


Figure 1: Hall Thruster Diagram

### Neutral Continuity

The continuity equation for neutrals is derived by taking the first moment of Boltzmann's equation. The resulting expression in differential form is

$$\frac{\partial n_n}{\partial t} + \frac{\partial (n_n \bar{v}_n)}{\partial z} = \dot{n}_w - \dot{n}_i \quad (1)$$

The terms on the right represent the rate per unit volume at which ions are lost to the wall, and the ionization rate respectively.

The ion loss rate to the wall is calculated from the rate at which ions enter the insulating wall sheath:

$$\dot{n}_w = \frac{2n_e v_b}{W} S(z) \quad (2)$$

where the Bohm velocity is given as

$$v_b = e^{-\frac{1}{2}} \sqrt{\frac{kT_e}{m_i}} \quad (3)$$

In Equation 2,  $S(z)$  represents a shape factor to account for imperfect wall-plasma contact near the injector and has values ranging from zero near the anode to one about halfway down the channel and beyond.

The ionization rate is derived assuming a Maxwellian electron distribution, a nonelastic ionization cross section according to Drawin's theory [2], and integrating over all electron energies. The resulting expressions used are

$$n_e = Q n_i n_n B_1 \frac{I(\theta)}{\theta^2} \quad (4)$$

$$I(\theta) = \int_0^\infty e^{-\frac{u}{\theta}} u g(u) du = \int_0^\infty e^{-\frac{u}{\theta}} \frac{u-1}{u} \ln(1.25 B_2 u) du \quad (5)$$

$$Q = 4 \bar{\sigma}_i \sqrt{\frac{E_i}{2 \pi m_i}} \quad (6)$$

$$u = \frac{E}{E_i} \quad (7)$$

$$\theta = \frac{k T_e}{E_i} \quad (8)$$

$\bar{\sigma}_i$  is a constant obtained by gathering all other constants into one and has the value for Argon of  $\bar{\sigma}_i = 1.04 \times 10^{-19}$ . The quantity  $Q$  is evaluated as  $Q_{Ar} = 2.77 \times 10^{-13}$  for Argon.  $E_i$  is the ionization energy,  $B_1$  and  $B_2$  are constants of order unity introduced from Drawin's cross-sectional theory, and  $u$  represents the ratio of energy to the propellants ionization energy.

### Electric Field Equation

The equation for electron momentum is obtained by taking the momentum moment of Boltzmann's equations. In applying the result to electrons, the terms due to electron inertia and the acceleration of heated electrons may be neglected. Additionally, variations in the radial and azimuthal directions are ignored and Bohm diffusion is used to obtain an effective electron collision frequency. The resulting expression after these simplifications is

$$n_e k \frac{\partial T_e}{\partial z} + k T_e \frac{\partial n_e}{\partial z} = -e n_e E - 16 e B n_e v_e \quad (9)$$

Rewriting  $E$  as  $-\frac{\partial \phi}{\partial z}$  and rearranging Equation 9, an expression for the electric field is obtained.

$$\frac{\partial \phi}{\partial z} = 16 B v_e + \frac{k T_e}{e n_e} \frac{\partial n_e}{\partial z} + \frac{k}{e} \frac{\partial T_e}{\partial z} \quad (10)$$

### Ion Density and Velocity Equations

To determine the ion density and velocity, a distribution function for ions is derived. In the absence of collisions, the Boltzmann Equation is used to produce

$$\frac{\partial f_i}{\partial t} + v_i \frac{\partial f_i}{\partial z} + \frac{e E}{m_i} \frac{\partial f_i}{\partial v_i} = n_i \delta(v_i - v_n) - \frac{n_w}{n_i} f_i \quad (11)$$

where  $f_i$  is the ion distribution function and the Dirac delta function,  $\delta$ , is employed so that ions are created at the neutral velocity. In Equation 11,  $n_i$  is the ionization rate and  $n_w$  is the ion loss rate to the channel walls per unit volume. This equation however, does not include the effects of ion-neutral collisions. Adding in a term to approximate this transfer results in

$$\frac{\partial f_i}{\partial t} + v_i \frac{\partial f_i}{\partial z} + \frac{e E}{m_i} \frac{\partial f_i}{\partial v_i} = n_i \delta(v_i - v_n) - \frac{n_w}{n_i} f_i + n_n Q_{in} \frac{1}{2} [n_i (\bar{v}_i - v_n) \delta(v_i - v_n) - (v_i - v_n) f_i] \quad (12)$$

The last term of Equation 12 is derived in such a way that it ensures conservation of ions and gives the correct momentum exchange rate. The addition of the factor of 1/2 preceding the last term is necessary to ensure the correct momentum transfer. Additionally, a constant value for the ion-neutral collision cross section,  $Q_{in}$ , is used. Rearranging slightly produces

$$\begin{aligned} \frac{\partial f_i}{\partial t} + v_i \frac{\partial f_i}{\partial z} + \frac{e E}{m_i} \frac{\partial f_i}{\partial v_i} = & \left[ n_i + \frac{1}{2} n_n Q_{in} (\bar{v}_i - v_n) \right] \delta(v_i - v_n) \\ & - \left[ \frac{n_w}{n_i} + \frac{1}{2} n_n Q_{in} (v_i - v_n) \right] f_i \quad (13) \end{aligned}$$

Equation 13 may be solved using the method of characteristics. The first step is to find the characteristic trajectories and then to calculate the rate of change of  $f_i$  along them. The characteristic system is

$$\frac{dt}{1} = \frac{dz}{v_i} = \frac{dv_i}{\frac{e E}{m_i}} = \frac{df_i}{(n_i + n_n \bar{v}_n) \delta(v_i - v_n) - \left( \frac{n_w}{n_i} + v_n \right) f_i} \quad (14)$$

where

$$v_{in} = \frac{1}{2} n_n Q_{in} (v_i - v_n) \quad (15)$$

$$\bar{v}_{in} = \frac{1}{2} n_n Q_{in} (\bar{v}_i - v_n) \quad (16)$$

Notice that the first equality in Equation 14 simply relates position and velocity and the second and third terms produce the energy equation for ions. However, the equality of interest is between the last two terms:

$$\left[ (n_e + n_e \bar{v}_{in}) \delta(v_i - v_n) - \left( \frac{n_e}{n_e} + v_{in} \right) f_i \right] dv_i = \frac{eE}{m_i} df_i \quad (17)$$

This equation may be integrated to create a distribution function. The integration is over the interval from  $v_i = \bar{c}_n$ , representing ions that were just created, to the maximum velocity the ions could achieve at their present location. This maximum velocity would equal the ion velocity if they were created at the anode and had no collisions:

$$v_{i,\max} = \sqrt{\frac{2e}{m_i} (\phi_a - \phi_z) + \bar{c}_n^2} \quad (18)$$

where  $\phi_a$  is the anode potential and  $\phi_z$  is the potential at the present axial location.  $\bar{c}_n$  is the neutral speed of sound at the anode,  $\bar{c}_n = \sqrt{\frac{5}{3} \frac{kT_{no}}{m_i}}$ , so that  $\bar{c}_n = \bar{v}_{no}$ . The distribution function is solved for each particular location  $z$ . For each  $v_i$ , there is a different  $z_0$ , or location where the ion was created, such that

$$\phi(z_0) = \phi(z) + \frac{m_i}{2e} (v_i^2 - \bar{v}_{no}^2) \quad (19)$$

The solution to Equation 17 is

$$f_i(v_i) = \left[ \frac{m_i (n_e + n_e \bar{v}_{in})}{eE} \right]_{z_0, t_0} e^{-\frac{m_i}{e} \int_{v_n}^{v_i} \frac{1}{E} \left( \frac{n_e}{n_e} + v_{in} \right) dv_i} \quad (20)$$

In the integral appearing in Equation 20, the quantities  $E$ ,  $\frac{n_e}{n_e}$  and  $v_{in}$  are evaluated at the time  $t'$  and location  $z'$  at which an ion with velocity  $v_i$  at  $(z, t)$  went through velocity  $v_i'$ . Thus,  $v_i'$  acts as the dummy variable of integration and as a parameter specifying the integrand. The time and location  $(z_0, t_0)$  are simply the  $(z', t')$  at which this particular ion was created and at which  $v_i' = \bar{v}_n$ . Also, note that the neutral speed  $\bar{v}_n$  is to be evaluated at  $(z', t')$  as well.

The ion distribution function, integrated over velocity, produces the ion or electron density

$$n_i(z) = \int_{\bar{v}_n}^{v_{i,\max}} f_i dv_i \quad (21)$$

The mass average ion velocity can be found by multiplying the right side of Equation 20 by  $v$  and integrating

$$n_i \bar{v}_i(z) = \int_{\bar{v}_n}^{v_{i,\max}} v_i f_i dv_i \quad (22)$$

### Neutral Velocity

Due to ion-neutral collisions, momentum is transferred from the ions to the neutrals resulting in an increase in the neutral velocity and a decrease in the ion velocity. For simplicity, the neutral velocities are all lumped together into their mean velocity,  $v_n$ , so that a neutral distribution function does not need to be created. The neutral momentum conservation equation may be written as

$$n_n \frac{d}{dz} \left( \frac{1}{2} m_i v_n^2 \right) = M_{in} \quad (23)$$

$M_{in}$  is the momentum change due to collisions and, assuming the same mass for both neutrals and ions, can be defined as

$$M_{in} = \int_0^{\bar{v}_n} \frac{m_i}{2} n_n (v_i - v_n) Q_{in} [n_e (\bar{v}_i - v_n) \delta(v_i - v_n) - (v_i - v_n) f_i] dv_i \quad (24)$$

Here  $Q_{in}$  is the collision cross section and for Argon  $Q_{in} = 1.4 \times 10^{-18} \text{ m}^3$ . Equation 24 satisfies the zeroth moment of the Boltzmann equation and produces the correct answer for the first (momentum) moment, but is invalid at higher moments. Simplifying and solving Equation 24 yields

$$M_{in} = \frac{m_i}{2} n_n Q_{in} \int_0^{\bar{v}_n} (v_i - v_n)^2 f_i dv_i \quad (25)$$

and evaluating the integral

$$M_{in} = \frac{m_i}{2} n_n n_e Q_{in} \langle (v_i - v_n)^2 \rangle \quad (26)$$

The term within  $\langle \rangle$  represents the averaged value of the quantity inside. Thus, Equation 23 may be written as

$$\bar{v}_n(z) = \sqrt{\bar{c}_n^2 + \Delta_n(z)} \quad (27)$$

where  $\Delta_n$  is given as

$$\Delta_n = Q_n \int_0^1 n_e \langle (v_i - v_n)^2 \rangle dz \quad (28)$$

### Electron Energy Equation

A total energy equation for electrons may be obtained by taking the energy moment of Boltzmann's equation and adding it to the dot product of the electron velocity and electron momentum. The resulting expression

$$\frac{\partial}{\partial t} \left[ n_e m_e \left( \frac{3}{2} \frac{k}{m_e} T_e + \frac{v_e^2}{2} \right) \right] + \nabla \cdot \left[ n_e m_e \bar{v}_e \left( \frac{3}{2} \frac{k}{m_e} T_e + \frac{v_e^2}{2} \right) + \bar{q}_e \right] + \nabla \cdot (n_e k T_e \bar{v}_e) = S_e \quad (29)$$

represents the total electron energy. The term  $\bar{q}_e$  is the thermal conduction vector

$$\bar{q}_e = -K_e \bar{\nabla} T_e \quad (30)$$

The right side source term includes energy lost to collisions, to the wall, and the energy gained due to the electric field ( $\bar{j} \cdot \bar{E}$ ). This equation may be simplified by introducing the variable  $X$  representing the total energy density, defined as

$$X = n_e m_e \left( \frac{3}{2} \frac{k}{m_e} T_e + \frac{v_e^2}{2} \right) \approx \frac{3}{2} n_e k T_e \quad (31)$$

So that Equation 29 may be rewritten as

$$\frac{\partial X}{\partial t} + \nabla \cdot [\bar{v}_e X + \bar{q}_e] + \nabla \cdot (n_e k T_e \bar{v}_e) = S_e \quad (32)$$

Rearranging and expanding equation 32, its differential form is obtained as

$$\frac{\partial X}{\partial t} + \frac{\partial(v_e X)}{\partial z} + \left( k n_e v_e - \frac{\partial K_e}{\partial z} \right) \frac{\partial T_e}{\partial z} - K_e \frac{\partial^2 T_e}{\partial z^2} = S_e - k T_e \frac{\partial(n_e v_e)}{\partial z} \quad (33)$$

Here the term  $k T_e \frac{\partial(n_e v_e)}{\partial z}$  has been moved to the right hand side as a source term since it contains no temperature term.

The term  $K_e$  is the heat conduction coefficient and described as a sum of two limiting models. The first is due to collisions and is the "classical" description in the presence of a strong magnetic field [2].

$$K_{e1} = 2.689 \times 10^{-11} \frac{T_e^{\frac{5}{2}}}{\beta^2 \ln \Gamma_e} \quad (34)$$

where

$$\Gamma_e = 1.24 \times 10^7 \sqrt{\frac{T_e^3}{n_e}} \quad (35)$$

$$\beta = \frac{eB}{m_e v_e} \quad (36)$$

The alternative heat conduction coefficient is derived according to Bohm diffusion.

$$K_{e2} = \frac{1}{2\pi} \frac{k^2 n_e T_e}{eB} \quad (37)$$

Summing these two thermal conductivities produces the effective heat transfer coefficient.

$$K_e = K_{e1} + K_{e2} \quad (38)$$

In Equation 38, because the Hall parameter,  $\beta$ , is large  $K_{e1} \approx K_{e2}$  and Bohm diffusion is the driving model for heat conduction.

The source terms for the energy equation include energy lost to the wall, energy lost in ionization and energy imparted to the plasma by the electric field. The energy input from the electric field is given as

$$\bar{j}_e \cdot \bar{E} = -en_e v_e E = en_e v_e \frac{\partial \phi}{\partial z} \quad (39)$$

Energy lost to ionization is

$$(1 + \gamma) e E_i n_i \quad (40)$$

Where the term  $(1 + \gamma)$  represents the net energy cost for each ion produced. For these calculations, a value of  $\gamma = 3$  is selected based on a more detailed analysis [3].

The energy lost to the wall consists of two electron fluxes, one into and one away from the wall, as shown in Figure 2. The first term, Equation 41, represents the energy lost by the electron flux to the wall and the second is the energy flux carried by the secondary electrons emitted at the wall back into the plasma.

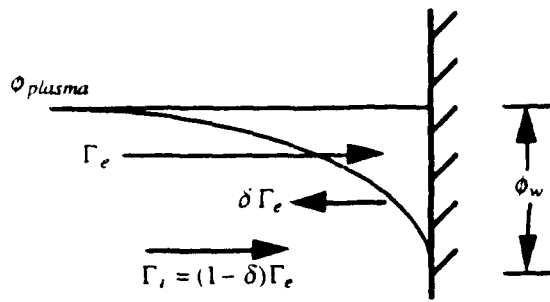


Figure 2 Wall fluxes

$$\Gamma_{\epsilon_i} = -\Gamma_e (2eT'_e + e\phi_w) \quad (41)$$

$$\Gamma_{\epsilon_i} = \Gamma_e e \delta \phi_w \quad (42)$$

where

$$\Gamma_e = \frac{n_e \bar{c}_e}{4} e^{-\frac{e\phi_w}{kT'_e}} \quad (43)$$

$$\bar{c}_e = \left( \frac{8 k T'_e}{\pi m_e} \right)^{\frac{1}{2}} \quad (44)$$

and  $\delta$  is the secondary emission coefficient. The total energy lost to the wall is given as

$$\sum \Gamma_{\epsilon_i} = -e \Gamma_e [2T'_e + (1 - \delta)\phi_w] \quad (45)$$

The term  $T'_e$  represents the electron temperature in electron volts, and  $\phi_w$  is the potential drop at the wall, given by  $\Gamma_i = (1 - \delta)\Gamma_e$  and  $\Gamma_i = n_i v_{bi}$ ,

which is valid for  $\phi_w > T'_e$  or  $1 - \delta > \sqrt{2\pi \frac{m_e}{m_i}}$ .

This gives

$$\phi_w = T'_e \ln \left[ (1 - \delta) \frac{e^{\frac{1}{2}}}{4} \sqrt{\frac{8m_i}{\pi m_e}} \right] \quad (46)$$

Equation 41 and 42 are represented in terms of the electron flux to the wall, but by using  $\Gamma_i = (1 - \delta)\Gamma_e$ , they may be rewritten in terms of the flux of ions to the wall or the ion wall loss defined in Equation 2:

$$\sum \Gamma_{\epsilon_i} = -en_w \left[ \frac{2T'_e}{1 - \delta} + \phi_w \right] \quad (47)$$

Summing all the energy sources gives the total energy source term for Equation 33

$$S_2 = en_e v_e \frac{\partial \phi}{\partial z} - e \left( (1 + \gamma) E_i n_e + n_w \left[ \frac{2T'_e}{1 - \delta} + \phi_w \right] \right) \quad (48)$$

### Channel Current

An additional relation for the plasma properties in the channel is one for current conservation where

$$\frac{I_a}{A} = j_i + j_e = en_e \bar{v}_e - en_e v_e \quad (49)$$

$I_a$  is the anode current and  $j_i$  and  $j_e$  are current densities. The equation could also be written in the form  $I_a = J_i + J_e$  to use currents. The ion current  $J_i$  at the exit, is sometimes referred to as the beam current  $I_b$ . Figure 3 diagrams the currents in the thruster. At the cathode, a part  $I_b$  of the emitted electrons, are required to neutralize the current of  $I_b$  ions. At the anode, the rest of the cathode electrons and the electrons produced by ionization,  $I_b$ , equals the anode current  $I_a$ .

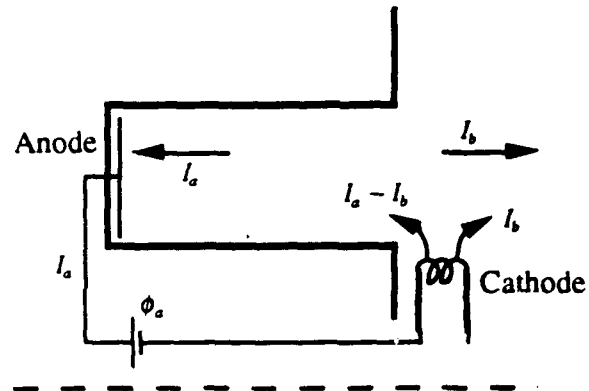


Figure 3 Hall Thruster Current Diagram

### Performance Characteristics

The thrust produced by the thruster can be calculated knowing the exit and inlet conditions. The thrust is derived as

$$F = \dot{m} (\bar{v}_{e,exit} - \bar{c}_e) + \dot{m}_n (\bar{v}_{n,exit} - \bar{c}_n) + k(n_e T'_e)_{exit} A + \frac{\epsilon_0}{2} E_{exit}^2 A \quad (50)$$

The specific impulse and thrust efficiency are calculated respectively by



$$I_{sp} = \frac{F}{mg} \quad (51)$$

$$\eta = \frac{F^2}{2mI_a\phi_a} \quad (52)$$

Here  $m$  is the mass flow,  $g$  gravitational acceleration, and  $I_a$  and  $\phi_a$  the acceleration current and potential.

To further define the flow efficiencies, three internal efficiencies are introduced as given by Komurasaki et. al. [1].

$$\eta_u = \frac{\dot{m}_i}{\dot{m}} \quad (53)$$

$$\eta_a = \frac{I_b}{I_a} \quad (54)$$

$$\eta_e = \frac{\dot{m}_e}{2e} \left( \frac{F}{\dot{m}_i} \right)^2 \quad (55)$$

$\eta_u$  is the propellant utilization efficiency,  $\eta_a$  the primary electron utilization and  $\eta_e$  a non uniformity factor representing the distribution in exit velocities.  $\eta_e$  penalizes the acceleration of ions over only part of the potential.  $\dot{m}_i$  is the ion mass flow rate and  $I_b$  the beam current.

Subsequently, by their definition, the thrust efficiency may be expressed as the product of the internal efficiencies

$$\eta = \eta_a \eta_e \eta_u \quad (56)$$

### Geometric Model

The geometric dimensions of the thruster chosen for verification of the model [1] are shown in Figure 4. The thruster has an inner radius of 2 cm, an outer radius of 2.4 cm, and accelerator length of 8 mm. The flow analysis extends out into the plume, where 6 mm past the accelerator channel exit plane, the cathode is located. The accelerator channel has a constant area to the physical exit. Beyond the exit, ions are still lost to a fictitious wall but no wall recombination takes place.

### Inputs and Boundary Conditions

The inputs to the code include the mass flow, magnetic field, anode current, neutral inlet temperature, and an initial or pre-ionization factor. From these parameters, the ion and neutral densities and ion, electron and neutral velocities at the anode may be computed and used as boundary conditions.

Additional boundary conditions at the end of the grid are that the electric field goes to zero, the electron temperature equals 1eV and the slope of the electron temperature is zero. This comprises a set of boundary conditions for six first order and one second order equation.

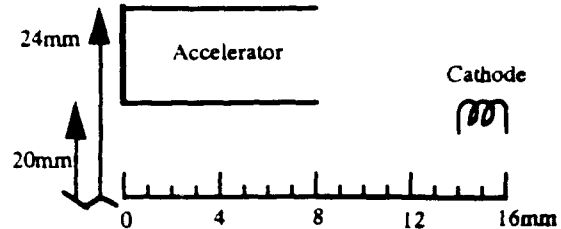


Figure 4: Thruster Geometry

### Numerical Model

The numerical model consist of a fixed spatial grid of eighty fixed intervals. Velocity is broken up into a scaleable grid of eighty intervals between  $\bar{v}_n$  and  $v_{max}$ . The neutral continuity equation (Equation 1) and the electron temperature equation (Equation 33) are integrated using MacCormack's method [4], a second-order accurate predictor-corrector method. The time step for a purely convective equation (Equation 1) is given by the Courant-Freidrichs-Lowy condition [4] as

$$\Delta t_c \leq \frac{\Delta z}{v_{max}} \quad (57)$$

The time step for a conductive-diffusive equation (Equation 33) given by Anderson is

$$\Delta t_d \leq \frac{(\Delta z)^2}{\left| kn_e v_e - \frac{\partial K_e}{\partial z} \right| + 2K_e} \quad (58)$$

The ratio of these two time steps  $\Delta t_c / \Delta t_d = N$  can be on the order of tens of thousands. For this reason, the electron energy equation is integrated  $N$  times for each time the other plasma equations are integrated and solved.

The flow path for the program is outlined in Figure 5. All the plasma properties are set to some initial value close to what the answer is believed to be. The electric field is then frozen. The time steps and source terms are evaluated using the values of the previous time step. Then the neutral conservation and momentum equations and ion distribution function are solved. The electron temperature equation is integrated  $N$  times and the plasma densities are checked for convergence. If the

densities have not converged, time is advanced one step and the equations solved again. If the densities have converged then the electric field equation is solved and checked for convergence. If it has not converged the electric field is frozen at its new value and the plasma properties solved again. If the electric field has converged the results are printed to a file.

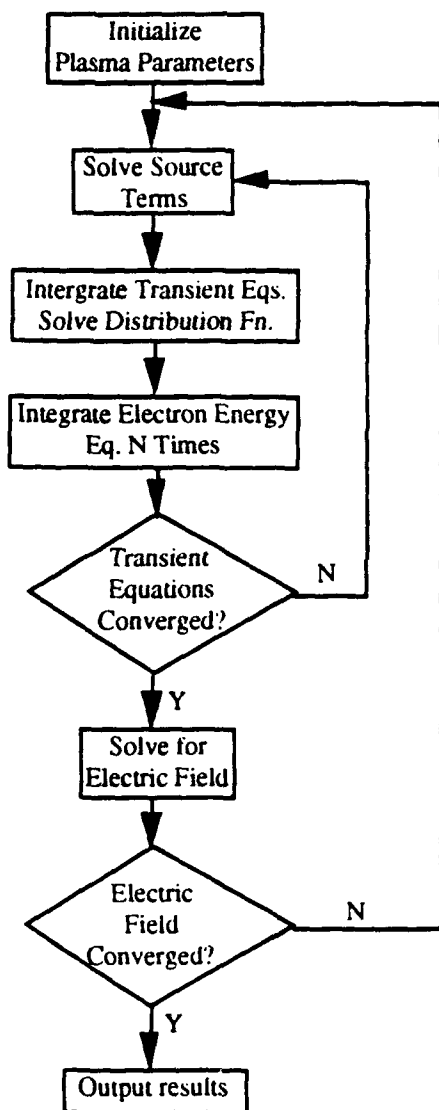


Figure 5: Program Flow Path

Typically, the time step calculated is of the order  $\Delta t = 10^{-8}$  seconds, except, as noted, for the electron temperature equation. The computational time for a solution is on the order of  $10^{-5}$  to  $10^{-4}$  seconds and the time for an ion to flow from the anode to the exit is of the order of  $10^{-6}$  seconds.

## Results

For all the runs presented here, the working gas is Argon with a mass flow of  $2.0 \text{ Aeq}$  ( $8.283 \times 10^{-7} \text{ kg/s}$ ). The average magnetic field is 0.1 Tesla with a minimum value of 0.093 T and maximum of 0.105. The loss shape factor used in Equation 2 has the profile shown in Figure 6 and is the same for all the numerical runs. The secondary electron emission from the wall,  $\delta$ , is set to 0.6 and a value of 3 is used for  $\gamma$ .

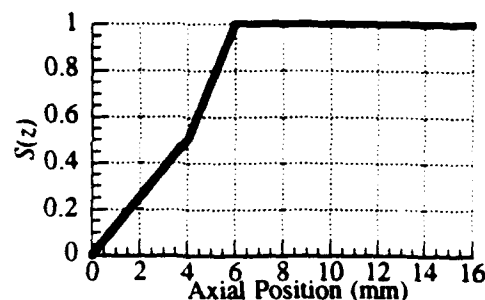
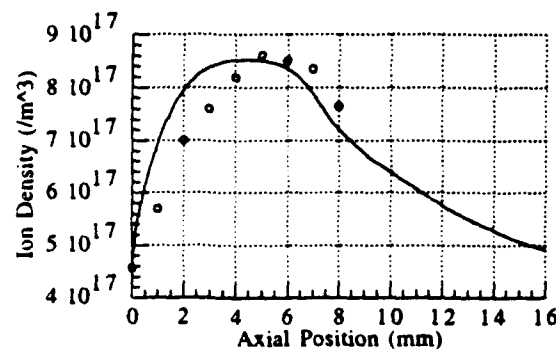


Figure 6: Shape Factor Profile

## Numerical/Experimental Comparison

For this run,  $I_a = 1.5 \text{ Amps}$  and the initial ionization fraction was chosen as 0.007. The numerical results are compared, when the data was given, to the results from Komurasaki where the two dimensional profiles have been averaged over the radial direction for several axial locations.



— Numerical Results    ° Komurasaki Data

Figure 7: Ion Density

Figures 7 through 11 show the profiles of the plasma properties. In Figure 7, the ion density rises more quickly than the experimental values. This is most likely due to incorrect modeling of the shape profile near the anode, in that there are actually more losses to the wall than modeled. However, the density reaches the same maximum density that the data does. The numerical results peak and fall off earlier than the data which

indicates that either the ionization rate is too low in this region or the wall loss is too large. The rapid falling off is more likely due to the ionization rate, which is lower than expected in the exit region.

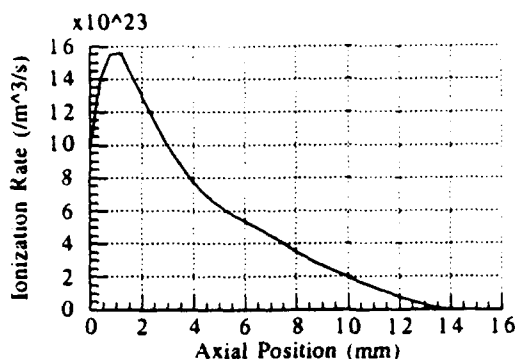


Figure 8: Ionization Rate

The ionization rate (Figure 8) reaches its maximum quickly and drops away smoothly after that. The peak is reached early in the channel where, even though the ion density is low, temperature and neutral density are at or near their maxima.

Figure 9 shows the ion and neutral velocity. The neutral velocity increases fairly constantly due to the ion-neutral collisions. The ion velocity shows a slope discontinuity at the channel exit (8 mm location). This is due to continued expansion and acceleration of the plasma without any wall losses. As Figure 10 shows, from the accelerator exit to the end of the computational grid, the potential drops less than half of the anode potential, while the ion velocity almost doubles. This is due to the majority of ions actually having a smaller velocity than their mean. These ions then benefit more in the remaining potential drop than those ions with velocities greater than their mean.

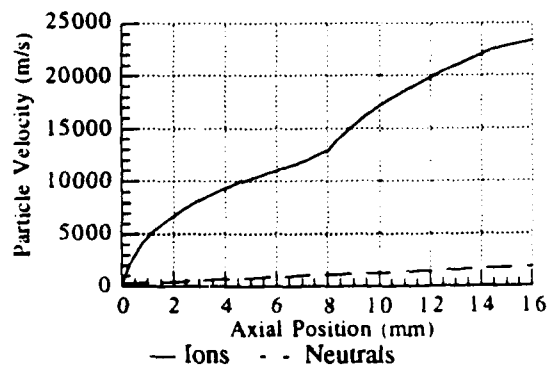
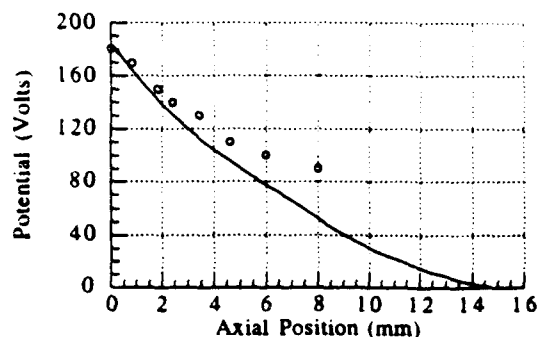


Figure 9: Heavy Particle Velocity

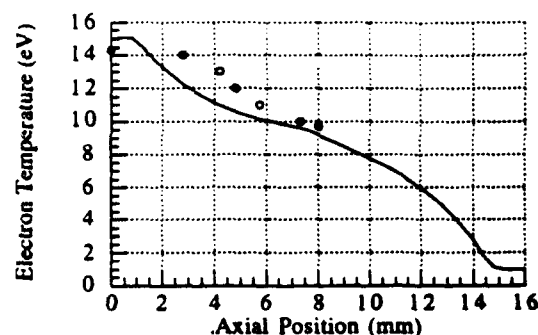
Figure 10 demonstrates that the numerical code accurately calculates the anode potential, but

that the potential drops away slightly quicker than the data. This indicates that over the accelerating channel, the electric field calculated is higher than in the experiment, while it is smaller outside the channel.



— Numerical Results ° Komurasaki Data

Figure 10: Potential



— Numerical Results ° Komurasaki Data

Figure 11: Electron Temperature

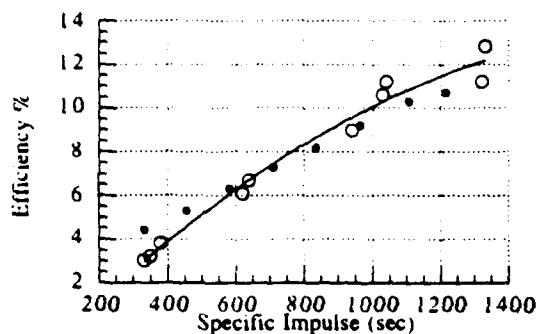
The electron temperature (Figure 11) peaks near the anode at almost fifteen electron volts. The data points shown in this case represent the channel centerline values and not channel averaged values. The experimental temperature at the anode is slightly lower and could be due to several factors. The first is that the computed electric field is too large in this area and the ionization rate and wall losses are too small. Another explanation is that the value selected for gamma is too small and does not accurately account for secondary ionization.

### Performance Comparison

The performance comparison was conducted to check the numerical code's validity at predicting the performance characteristics of the thruster over a wide range of operating powers. For this analysis, the average magnetic field remained at 0.1 Tesla, the mass flow was held at 2.0 Aeq while the anode

current was varied between 0.75 and 2.5 Amps to alter the operating power levels.

Figure 12 shows the results from this study. The efficiency was found to vary from 4.5% at an anode current of 0.75 Amps to almost 11% at 2.5 Amps. Over this same range, the anode potential increases from 127 Volts to 225 Volts and the propellant utilization efficiency rises from 24% to 74%. Both the acceleration efficiency and nonuniformity factor are relatively constant over the range studied, with values 0.25 and 0.6 respectively. Their insensitivity to the accelerating current agrees with results and conclusions from Komurasaki's analysis.



° Komurasaki Data — Komurasaki Data Fit  
• Numerical Results

Figure 12: Performance Results

## Conclusions

The purpose of this study was to create a relatively simple yet versatile code for the analysis of a Hall thruster. The code produced demonstrates a high level of accuracy in both predicting the plasma properties in the acceleration channel and in calculating the performance characteristics of the thruster. In the course of developing the code, a model was constructed of the ion distribution function accounting for momentum transfer between heavy species and for the effect of wall losses. Further studies will test the code over a wider range of operating conditions and model other thruster geometries to test its full viability.

## Bibliography

1. Komurasaki, K., Hirakawa, M. and Arakawa, Y., "Plasma Acceleration Process in a Hall-Current Thruster," IEPC Paper 91-078, 1991.
2. Mitchner and Kruger, Partially Ionized Gases, John Wiley & Sons, New York, 1973.

3. Dugan, John V. and Sovie, Ronald J., "Volume Ion Production Costs in Tenuous Plasmas: A General Atom Theory and Detailed Results for Helium, Argon and Cesium," NASA TN D-4150.

4. Anderson, Dale A., Tannehill, John C., Pletcher, Richard H., Computational Fluid Mechanics and Heat Transfer, Hemisphere Publishing Corporation, New York, 1984.

# AN EXPLANATION FOR ANODE VOLTAGE DROPS IN MPD THRUSTERS

E.H. Niewood\* and M. Martinez-Sanchez<sup>†</sup>

Space Power and Propulsion Laboratory

Dept. of Aeronautics and Astronautics, MIT, Cambridge, MA 02139

## Abstract

Theoretical and computational predictions of MPD thruster efficiency are substantially higher than experimental measurements for comparable geometries. One reason for this discrepancy is the large anode voltage drops found in experiments but not in current models. This paper shows that these voltage drops could be occurring in the quasi-neutral near anode region of the plasma. These near anode drops arise because of starvation of the plasma. A one dimensional analytical model is used to show that these voltage drops may, in principle, exist. A computational axisymmetric thruster simulation is used to show that the voltage drops which arise by this mechanism show good agreement with experimental data.

## Nomenclature

$B$	Magnetic field strength.
$\bar{C}$	Random velocity.
$e$	Charge of a proton.
$E$	Electric field strength.
$E_i$	Ionization energy.
$J$	Current density.
$k$	Boltzman's constant.
$m$	Particle mass.
$n$	Number density.
$n_e$	Electron production rate.
$P$	Pressure.
$t$	Time.
$Q$	Collision cross section.
$T$	Temperature.
$V$	Velocity.
$\alpha$	Ionization fraction.
$\nu$	Collision frequency.
$\rho$	Mass density.
$\sigma$	Electrical conductivity.

$\Theta$	Heat conduction coefficient.
$\nu$	Viscosity coefficient.

Note: The subscripts e,n,i, and g refer to electrons, neutrals, ions, and heavy species respectively. When used as subscripts or otherwise, r,  $\theta$ , and z refer to the coordinate directions.

## 1 Introduction

Magnetoplasmdynamic (MPD) thrusters have been considered as a means of propulsion for spacecraft on long missions for the past thirty years. MPD thrusters produce thrust in the range of 1-100 Newtons at specific impulses ranging from 1000-5000 seconds. They are expected to be most efficient at power levels on the order of MegaWatts. However, the experimentally measured efficiency of these devices is too low for them to be attractive for space use. Experiments show efficiencies under 30% in almost all cases [17, 10]. These experimental measurements are much lower than efficiencies predicted by theoretical or computational means [12, 14]. As the devices are run at fixed currents, the efficiency is a function only of the jet power and the voltage between the electrodes. Computational and analytical predictions of jet power are usually quite good [11, 14]. Therefore, the discrepancy in efficiency must arise due to low voltage predictions by the various models. Recent experiments have shown that a large component of the voltage drop in experimental devices takes place very near the anode and results mainly in heating of the anode [5, 7].

This paper attempts to show that these voltage drops may be a result of starvation of the near anode plasma. Section 2 details the mechanism by which these drops arise. Section 3 describes an analytical model which gives some insight into the physics of the voltage drops. Section 4 describes a computational model of MPD thrusters. Section 5 presents results from that simulation showing good agreement between numerically predicted and experimen-

\*Graduate Student, Member AIAA

<sup>†</sup>Professor, Member AIAA

tally measured voltage drops.

## 2 Theory

If there were such a thing as an ideal thruster without the Hall effect, there would be no axial current and the current would run straight from electrode to electrode. However, due to the Hall effect there is axial current, the magnitude of which is approximately given by

$$J_z \approx -\frac{\sigma B_\theta}{en_e} J_r = \beta J_r \quad (1)$$

where  $\beta = \frac{\sigma |B_\theta|}{en_e}$  is the Hall parameter and the magnetic field is into the plane of the thruster and so has a negative sign. Since the Hall parameter is inversely proportional to the electron number density,  $\beta$  and  $J_z$  increase as  $n_e$  decreases. Increased axial current leads to higher radial Lorentz force, which must be approximately balanced by a radial pressure gradient:

$$\frac{\partial n_e k(T_e + T_g)}{\partial r} = -J_z B_\theta. \quad (2)$$

Since  $J_z$  and  $B_\theta$  are both negative and  $T_e$  and  $T_g$  are expected to be relatively constant, the radial gradient of  $n_e$  must be negative. Therefore,  $n_e$  must decrease dramatically in the radial direction if  $J_z$  is large, as

$$\frac{\partial n_e}{\partial r} \approx -\frac{J_z B_\theta}{k(T_e + T_g)}.$$

So, low electron number density and high axial current can build on each other and lead to anode starvation.

Once the anode becomes starved, large radial electric fields will develop, as seen from Ohm's Law. The Hall component of the radial field, which is dominant in the starved region, is given by

$$E_r \approx -\frac{1}{en_e} (J_z B_\theta + \frac{\partial P_e}{\partial r}) \quad (3)$$

Since  $n_e$  is small and  $J_z$  is large, the radial electric field can be quite large. Starvation has been observed experimentally [9]. However, the width of the starved region, and therefore the extent of the voltage drop across it, has not been experimentally determined. If this field is large enough and occurs over a wide enough region, the voltage drop across the starved region can be significant.

## 3 Analytical Model

Probably the first model of anode starvation is that of Bakhst. Bakhst's [2] focus was on determining when starvation occurs, but his model also

predicts the resulting voltage drop. Bakhst assumes that the axial electric field is zero with the axial electron pressure gradient and ion velocity neglected. Assuming that the ion and electron temperatures are constant radially and combining equations 1 and 2 yields

$$\frac{\partial n_e}{\partial r} = \frac{\sigma B_\theta^2 J_r}{en_e k(T_e + T_g)}. \quad (4)$$

If  $B_\theta$  and  $J_r$  are constant radially then

$$n_e(r) = \sqrt{\frac{2\sigma B_\theta^2 J_r (r - r_a)}{ek(T_e + T_g)}} + n_{e0}. \quad (5)$$

From equation 3, the contribution to the radial electric field from the Hall and electron pressure terms is then

$$E_{r,Hall} = \frac{\sigma B_\theta^2 J_r}{(en_e)^2} \frac{T_g}{T_e + T_g} \quad (6)$$

The potential drop across the near anode layer is then given by

$$\begin{aligned} \Delta V(\text{anode}) &= \int_{r_{\text{anode}}}^{r_a} E_r dr \\ &= \frac{kT_g}{2e} \ln \frac{k(T_e + T_g)en_{e0}^2}{(r_{\text{outer}} - r_a)2\sigma B_\theta^2 J_r + k(T_e + T_g)en_{e0}^2}. \end{aligned} \quad (7)$$

Bakhst assumes that the anode current density will be due to the random electron thermal flux to the wall, so that

$$n_{e0} = -\frac{4J_r}{e\bar{C}}$$

Bakhst's model can be used to predict the anode voltage drop between the anode and the last inner point of the simulation described in Section 5. At a point midway down the electrode,  $T_e = 23,000\text{K}$ ,  $T_g = 3200\text{K}$ ,  $B_\theta = 0.0726T$ ,  $\sigma = 3580 \frac{\text{Si}}{\text{m}}$ , and  $J_r = -2.08 \times 10^{-5} \frac{\text{A}}{\text{m}^2}$ . So,  $\bar{C} = 591,000\text{m/s}$  and, to get the right thermal flux,  $n_{e0} = 8.8 \times 10^{18}$ . The last interior point is 0.1 mm away from the anode at  $r_a = 0.072\text{m}$ . The Bakhst model predicts a potential drop over the last cell of -1.09 Volts. The distribution of the electron number density, the radial electric field, and the potential drop are shown in Figures 1 - 3.

However, this Bakhst formulation neglects a number of effects, particularly in the transverse momentum equation. A somewhat more complete model has been developed. This model also assumes that the axial electric field is zero throughout the near anode region,

$$\frac{1}{\mu_0 \sigma r} \frac{\partial r B_\theta}{\partial r} = V_{ir} B_\theta + \frac{1}{en_e} \frac{\partial}{\partial z} \frac{B_\theta^2}{2\mu_0} + \frac{1}{en_e} \frac{\partial}{\partial z} n_e k T_e \quad (8)$$

where electron-neutral collisions have been neglected. The transverse momentum equation for the charged species is modified by including the contribution due to ion-ion viscosity,  $S_{ir}$ , so that

$$\frac{\partial n_e}{\partial r} = \frac{1}{k(T_g + T_e)} \left[ -\frac{B_\theta}{\mu_0 r} \frac{\partial r B_\theta}{\partial r} + S_{ir} \right]. \quad (9)$$

Even though the ion-neutral viscosity is 2-5 times larger than the ion-ion viscosity, due to the low ionization fraction, the radial gradients of the ion velocity are 100-1000 times larger than those of the neutral velocity. Therefore, the viscosity source term, given in complete form in Section 4 will be assumed to be given by

$$S_{ir} \approx \frac{4}{3} v_{ii} \frac{\partial^2 V_{ir}}{\partial r^2}.$$

Over the small transverse region being modeled, the change in the axial flow must be relatively small. Therefore,

$$\frac{\partial}{\partial r} \rho_i V_{ir} \approx 0 \quad (10)$$

Taking the appropriate derivatives,

$$\frac{\partial^2 V_{ir}}{\partial r^2} = -\frac{V_{ir}}{\rho_i} \frac{\partial^2 \rho_i}{\partial r^2} + \frac{2V_{ir}}{\rho_i^2} \left( \frac{\partial \rho_i}{\partial r} \right)^2$$

The radial momentum equation can then be written as

$$\frac{\partial^2 n_e}{\partial r^2} = \frac{2}{n_e} \left( \frac{\partial n_e}{\partial r} \right)^2 - \frac{3n_e}{4v_{ii} V_{ir}} \left[ B_\theta J_z + k(T_g + T_e) \frac{\partial n_e}{\partial r} \right] \quad (11)$$

where

$$J_z = \sigma \left[ V_{ir} B_\theta + \frac{B_\theta}{en_e \mu_0} \frac{\partial B_\theta}{\partial z} + \frac{1}{en_e} \frac{\partial}{\partial z} n_e k T_e \right].$$

The magnetic field is given by

$$\frac{\partial r B_\theta}{\partial r} = \mu_0 J_z r \quad (12)$$

and the Hall component of the radial electric field is given by

$$E_{r,Hall} = -\frac{1}{en_e} \left[ B_\theta J_z + k T_e \frac{\partial n_e}{\partial r} \right]. \quad (13)$$

In order to match the Bakhst theory, the magnetic field and the electron number density at the anode were chosen as two of the boundary conditions. The third boundary condition was that the radial derivative of  $n_e$  was zero at the outer edge of the layer. For the same  $T_e$ ,  $T_g$  and  $\sigma$  as used for the Bakhst model and with additional conditions that  $v_{ii} = 7.3 \times 10^{-8}$  and  $V_{ir}(d) = V_b$  at the wall and assuming  $\frac{\partial P_e}{\partial z} = 0$ , the solutions for this modified theory are given along

with the Bakhst results in Figures 1 - 3. The solutions were obtained by shooting with a variable step size Runge-Kutta algorithm. The total Hall potential drop across the near anode region predicted by this model is -9.68 Volts. The difference between the two models is due to the lower electron number density over the layer predicted by the modified theory. The modified theory predicts lower  $n_e$  because the total pressure (fluid and magnetic) away from the anode is less than that at the anode due to viscous dissipation. Lower total pressure for constant temperatures implies lower electron number density.

## 4 Computational Model

A three fluid simulation of MPD thrusters has been developed and used to show that anode starvation can lead to voltage drops of the same magnitude seen experimentally. The simulation assumes that the plasma is quasi-neutral. The geometry is assumed to be cylindrical, with no variation in the azimuthal direction. The magnetic field is assumed to be confined to the azimuthal direction. The electric field, the current, and the velocity all have components in both in plane directions. The plasma is treated as being out of equilibrium, in that the electron and heavy species temperatures are treated separately and coupled only by elastic collisional energy transfer, the ionization fraction is not determined by Saha equilibrium, but by balancing ion flow with ionization and recombination collisions, and the ion and neutral velocities are coupled only by collisional drag. The governing equations and the relevant source terms are described below.

### 4.1 Governing Equations

Incorporating the above assumptions yields a model consisting of nine partial differential equations. There are eight differential equations for the fluid variables and one for the magnetic field.

$$\frac{\partial n_e}{\partial t} + \frac{\partial(n_e V_{ir})}{\partial r} + \frac{\partial(n_e V_{iz})}{\partial z} = -\dot{n}_R + \dot{n}_I - \frac{n_e V_{ir}}{r}, \quad (14)$$

and

$$\frac{\partial n_n}{\partial t} + \frac{\partial(n_n V_{nr})}{\partial r} + \frac{\partial(n_n V_{nz})}{\partial z} = -\dot{n}_I + \dot{n}_R - \frac{n_n V_{nr}}{r}. \quad (15)$$

where  $\dot{n}_R$  represents the number of recombination events and  $\dot{n}_I$  represents the number of ionization events. As mentioned above, the plasma is assumed to be quasi-neutral, so that  $n_e$  is used in place of  $n_i$ . It is useful to define the global density,

$$\rho = m_e n_e + m_i n_e + m_n n_n \approx m_n (n_e + n_n).$$

It is convenient to define the global velocity, the current, and the neutral slip velocity, where, respectively,

$$\mathbf{V} = \frac{m_e n_e \mathbf{V}_e + m_i n_i \mathbf{V}_i + m_n n_n \mathbf{V}_n}{\rho} \approx \alpha \mathbf{V}_i + (1-\alpha) \mathbf{V}_n$$

with

$$\alpha = \frac{n_e}{n_e + n_n},$$

$$\mathbf{J} = -en_e(\mathbf{V}_e - \mathbf{V}_i)$$

$$\mathbf{U} = \mathbf{V}_i - \mathbf{V}_n.$$

The state equation for each species is assumed to be given by

$$P_s = n_s k T_s. \quad (16)$$

Therefore, the neutral momentum equations are

$$\frac{\partial(\rho_n V_{nr})}{\partial t} + \frac{\partial(\rho_n V_{nr}^2 + P_n)}{\partial r} + \frac{\partial(\rho_n V_{nr} V_{nz})}{\partial z}$$

$$= S_{nnr} + S_{nir} + K_{ni}(V_{ir} - V_{nr}) + K_{ne}(V_{er} - V_{nr})$$

$$- \dot{n}_I m_i V_{nr} + \dot{n}_R m_i V_{ir} - \frac{\rho_n V_{nr}^2}{r} \quad (17)$$

and

$$\frac{\partial(\rho_n V_{nz})}{\partial t} + \frac{\partial(\rho_n V_{nr} V_{nz})}{\partial r} + \frac{\partial(\rho_n V_{nz}^2 + P_n)}{\partial z}$$

$$= S_{nnz} + S_{niz} + K_{ni}(V_{iz} - V_{nz}) + K_{ne}(V_{ez} - V_{nz})$$

$$- \dot{n}_I m_i V_{nz} + \dot{n}_R m_i V_{iz} - \frac{\rho_n V_{nr} V_{nz}}{r} \quad (18)$$

where  $S_{nir}$  and  $S_{niz}$  represent the viscous terms and

$$K_{st} = n_s m_{st} \nu_{st} = K_{ts}$$

$$m_{st}^{-1} = m_s^{-1} + m_t^{-1}$$

and

$$\nu_{st} = n_t \bar{C}_{st} Q_{st}.$$

The electron momentum equations are used to derive the Ohm's laws, given by

$$E_r = V_{iz} B_\theta - \frac{1}{en_e} (J_z B_\theta + \frac{\partial P_e}{\partial r}) + \frac{J_r}{\sigma} \quad (19)$$

$$E_z = -V_{ir} B_\theta - \frac{1}{en_e} (\frac{\partial P_e}{\partial z} - J_r B_\theta) + \frac{J_z}{\sigma} \quad (20)$$

These equations can be used to replace the electric field term in the ion momentum equation. Doing this yields the ambipolar momentum equations

$$\frac{\partial(\rho_i V_{ir})}{\partial t} + \frac{\partial(\rho_i V_{ir}^2 + P_i + P_e)}{\partial r} + \frac{\partial(\rho_i V_{ir} V_{iz})}{\partial z} = -J_z B_\theta$$

$$+ S_{iir} + S_{inr} + K_{in}(V_{nr} - V_{ir}) + K_{en}(V_{nr} - V_{er})$$

$$+ \dot{n}_I m_i V_{nr} - \dot{n}_R m_i V_{ir} - \frac{\rho_i V_{ir}^2}{r} \quad (21)$$

and

$$\frac{\partial(\rho_i V_{iz})}{\partial t} + \frac{\partial(\rho_i V_{ir} V_{iz})}{\partial r} + \frac{\partial(\rho_i V_{iz}^2 + P_i + P_e)}{\partial z} = J_r B_\theta$$

$$+ S_{iiz} + S_{inz} + K_{in}(V_{nz} - V_{iz}) + K_{en}(V_{nz} - V_{ez})$$

$$+ \dot{n}_I m_i V_{nz} - \dot{n}_R m_i V_{iz} - \frac{\rho_i V_{ir} V_{iz}}{r} \quad (22)$$

If  $T_i = T_n$  then the overall heavy species energy equation is

$$\frac{\partial(\frac{3}{2} P_g)}{\partial t} + \frac{\partial(\frac{3}{2} P_g V_r)}{\partial r} + \frac{\partial(\frac{3}{2} P_g V_z)}{\partial z} + P_g (\frac{\partial V_r}{\partial r} + \frac{\partial V_z}{\partial z})$$

$$= \frac{3k}{m_n} (K_{ie} + K_{ne})(T_e - T_g) + \Phi + \kappa_i + \kappa_n - \frac{5}{2} \frac{P_g V_r}{r}$$

$$+ \frac{1}{2} [K_{ni} + K_{in} + m_i (\dot{n}_I + \dot{n}_R)] (U_r^2 + U_z^2). \quad (23)$$

where  $T_g \equiv T_i = T_n$  and  $P_g \equiv \frac{h}{m_i} \rho T_g$ .

Using the electron continuity equation the energy equation can be rewritten in non-conservative form as

$$\frac{3}{2} n_e k [\frac{\partial T_e}{\partial t} + V_{er} \frac{\partial T_e}{\partial r} + V_{ez} \frac{\partial T_e}{\partial z} + T_e (\frac{\partial V_{er}}{\partial r} + \frac{\partial V_{ez}}{\partial z})]$$

$$= (K_{ei} + K_{en}) \left[ \frac{3k}{m_n} (T_g - T_e) \right] + \kappa_e + \frac{J^2}{\sigma}$$

$$+ K_{en} (U^2 - 2 \frac{\mathbf{J} \cdot \mathbf{U}}{en_e}) - \dot{n}_e (E_i - \frac{3}{2} k T_e) - \frac{P_e V_{er}}{r}. \quad (24)$$

From Maxwell's equations,

$$\frac{\partial B_\theta}{\partial t} = -\frac{\partial E_r}{\partial z} + \frac{\partial E_z}{\partial r}. \quad (25)$$

The scalar components of the current are given by

$$J_r = -\frac{1}{\mu_0} \frac{\partial B_\theta}{\partial z} \quad (26)$$

and

$$J_z = \frac{1}{\mu_0 r} \frac{\partial r B_\theta}{\partial r} = \frac{1}{\mu_0} \frac{\partial B_\theta}{\partial r} + \frac{B_\theta}{\mu_0 r} \quad (27)$$

## 4.2 Source Terms

Because of the substantial slip between neutrals and ions, the viscous source terms are more complex than those in the one fluid Navier-Stokes equations. A derivation and expression for these terms was found in a recent paper by Fernandes and Fernandes[3]. According to their derivation the non-isotropic part of the pressure tensor is given by

$$\Pi_s = 2\nu_{si} \nabla \circ \mathbf{V}_i + 2\nu_{sn} \nabla \circ \mathbf{V}_n. \quad (28)$$

where the operator  $\nabla \circ \mathbf{V}$  is the symmetric traceless gradient of  $\mathbf{V}$  given by [4]

$$\nabla \circ \mathbf{V} \equiv \tilde{\nabla} \mathbf{V} - \frac{1}{3} (\nabla \cdot \mathbf{V}) \mathbf{I} \equiv \mathbf{T}, \quad (29)$$



Expanding the various derivatives yields the viscous source terms [1],

$$S_{itr} = v_{it} \left[ \frac{4}{3} \frac{\partial^2 V_{ir}}{\partial r^2} + \frac{\partial^2 V_{ir}}{\partial z^2} + \frac{1}{3} \frac{\partial^2 V_{iz}}{\partial r \partial z} \right] + \frac{4}{3} \frac{\partial V_{ir}}{\partial r} \left( \frac{v_{it}}{r} + \frac{\partial v_{it}}{\partial r} \right) + \frac{\partial V_{ir}}{\partial z} \frac{\partial v_{it}}{\partial z} + \frac{\partial V_{iz}}{\partial r} \frac{\partial v_{it}}{\partial z} - \frac{2}{3} \frac{\partial V_{iz}}{\partial z} \frac{\partial v_{it}}{\partial r} - \frac{2}{3} \frac{V_{ir}}{r} \left( \frac{\partial v_{it}}{\partial r} + 2 \frac{v_{it}}{r} \right) \quad (30)$$

and

$$S_{itz} = v_{it} \left[ \frac{4}{3} \frac{\partial^2 V_{iz}}{\partial z^2} + \frac{\partial^2 V_{iz}}{\partial r^2} + \frac{1}{3} \frac{\partial^2 V_{ir}}{\partial r \partial z} \right] + \frac{\partial V_{ir}}{\partial z} \left( \frac{1}{3} \frac{v_{it}}{r} + \frac{\partial v_{it}}{\partial r} \right) - \frac{2}{3} \frac{\partial V_{ir}}{\partial r} \frac{\partial v_{it}}{\partial z} - \frac{2}{3} \frac{V_{ir}}{r} \frac{\partial v_{it}}{\partial z} + \frac{\partial V_{iz}}{\partial r} \left( \frac{\partial v_{it}}{\partial r} + \frac{v_{it}}{r} \right) + \frac{4}{3} \frac{\partial v_{it}}{\partial z} \frac{\partial V_{iz}}{\partial z} \quad (31)$$

The pressure tensor also appears in the energy equations. The non-diagonal terms of the pressure tensor are buried in the viscous dissipation term and are given by [1]

$$\Phi = \Phi_i + \Phi_n = \sum_i \left[ (v_{ii} + v_{nn}) \left( \frac{4}{3} \left( \frac{\partial V_{ir}}{\partial r} \right)^2 + \left( \frac{V_{ir}}{r} \right)^2 + \left( \frac{\partial V_{iz}}{\partial z} \right)^2 - \frac{V_{ir}}{r} \frac{\partial V_{ir}}{\partial r} - \frac{\partial V_{ir}}{\partial r} \frac{\partial V_{iz}}{\partial z} - \frac{V_{ir}}{r} \frac{\partial V_{iz}}{\partial z} + \left( \frac{\partial V_{ir}}{\partial z} + \frac{\partial V_{iz}}{\partial r} \right)^2 \right) \right] \quad (32)$$

The various viscosity coefficients are given by [3]

$$v_{ii} = \left[ \alpha^2 \left( \frac{2}{3} + a_i \right) + \frac{\alpha(1-\alpha)v_*}{v_n} \right] / q_i, \quad (33)$$

$$v_{nn} = \left[ (1-\alpha)^2 \left( \frac{2}{3} + a_i \right) + \frac{\alpha(1-\alpha)v_*}{v_i} \right] / q_i, \quad (34)$$

and

$$v_{in} = v_{ni} = \alpha(1-\alpha) \left( \frac{2}{3} - a_i \right) / q_i \quad (35)$$

where

$$q_i = \left( \frac{2}{3} + a_i \right) \left[ \frac{\alpha^2}{v_i} + \frac{(1-\alpha)^2}{v_n} \right] + \alpha(1-\alpha) \left[ \frac{v_*}{v_n v_i} + \frac{8a_i}{3v_*} \right],$$

$$v_* = \frac{5kT_g}{8\Omega_i^{(2,2)}},$$

$$v_* = \frac{kT_g}{4\Omega_{in}^{(1,1)}},$$

and

$$a_i = \frac{\Omega_{in}^{(2,2)}}{5\Omega_{in}^{(1,1)}}.$$

The collision integrals  $\Omega$  are given by [4]

$$\Omega_{ij}^{(l,r)} = \left( \frac{kT_g}{2\pi m_{ij}} \right)^{\frac{1}{2}} \int_0^\infty e^{-g^2} g^{2r+3} Q_{ij}^{(l)} dg. \quad (36)$$

The neutral-neutral and ion-neutral collisions will be modeled as hard sphere collisions. Using experimental values from Lieberman and Velikovich [13], the relevant cross sections are given by

$$Q_{nn}^{(2)} = \frac{2}{3} Q_{nn}^{\text{experimental}} = \frac{2}{3} (1.7 \times 10^{-18} T_n^{-\frac{1}{2}}) \quad (37)$$

and

$$Q_{in}^{(2)} = \frac{2}{3} Q_{in}^{\text{experimental}} = \frac{2}{3} (1.4 \times 10^{-18}). \quad (38)$$

All units in the thesis are MKS unless otherwise noted. For the ion-ion collisions the integrals can be approximated using the Coulomb interaction potential cut off at the Debye length. From Fersiger and Kaper again,

$$\Omega_{ii}^{(2,2)} = \frac{1}{4} \left( \frac{2\pi kT_g}{m_{ii}} \right)^{\frac{1}{2}} \left( \frac{e^2}{4\pi\epsilon_0 kT_g} \right)^2 \ln \Gamma_g, \quad (39)$$

where

$$\Gamma_g = 1.24 \times 10^7 \sqrt{\frac{T_g^3}{n_e}}. \quad (40)$$

The heat conduction terms  $\kappa_s$  are given by  $\kappa_s = -\nabla \cdot \mathbf{H}_s$ . The heat flux vector,  $\mathbf{H}$  is

$$\mathbf{H}_s = -\Theta_s \nabla T_s. \quad (41)$$

where  $\Theta$  represents the thermal conductivity. So, the contribution from the heat conduction terms is

$$\kappa_s = \Theta_s \left[ \frac{1}{r} \frac{\partial T_s}{\partial r} + \frac{\partial^2 T_s}{\partial r^2} + \frac{\partial^2 T_s}{\partial z^2} \right] + \frac{\partial T_s}{\partial r} \frac{\partial \Theta_s}{\partial r} + \frac{\partial T_s}{\partial z} \frac{\partial \Theta_s}{\partial z}. \quad (42)$$

From Mitchner and Kruger [15], the thermal conductivity for the electrons is given by

$$\Theta_e = \frac{2.4}{1 + \frac{\nu_{ei}}{\sqrt{2}\nu_{eg}}} \frac{k^2 n_e T_e}{m_e \nu_{eg}} \quad (43)$$

For the heavy species the thermal conductivity is given similarly by

$$\Theta_g = \frac{k^2 T_g}{m_i \tilde{C}_g} \left[ \frac{n_n}{n_n Q_{nn} + n_e Q_{in}} + \frac{n_e}{n_e Q_{ii} + n_n Q_{in}} \right] \quad (44)$$

where

$$Q_{ii} = \frac{e^4 \ln \Gamma_i}{32\pi\epsilon_0^2 k^2 T_i^3}. \quad (45)$$

and

$$\tilde{C}_s = \sqrt{\frac{8kT_s}{\pi m_s}}.$$

Sheppard [16] has developed a fit to a multilevel model which compares well with experiment. His recombination coefficient,  $R$ , for Argon is given by [16]

$$R = 8.25 \times 10^{-43} e^{1.8276(\log \frac{T_e}{1000} - 3.95)} \quad (46)$$

The recombination rate is then given by

$$\dot{n}_R = R n_e^2$$

By detailed balancing, the ionization rate is then given by

$$\dot{n}_I = R S n_e n_n$$

where

$$S = 2.9 \times 10^{22} T_e^{\frac{1}{2}} \exp\left(\frac{-eE_i}{kT_e}\right)$$

## 5 Computational Results

The experimental device on which this research concentrated was the Constant Area Channel (CAC) studied by Heimerdinger, Kilfoyle, and Martinez-Sanchez [7, 8, 6, 9]. However, the bulk of the experimental work reported by Heimerdinger et. al. involved the Fully Flared Cathode (FFC), which differed from the CAC in the shape of the cathode, but was the same device in other respects. Results from the two thrusters will be treated somewhat interchangeably in the following discussion. Where necessary, a distinction will be drawn between the two devices.

The physical thruster was an axisymmetric device with the cathode as the inner electrode. Both the cathode and anode were 0.09 m long, with a constant outer radius for the cathode of the CAC of 0.053 m and a constant inner radius for the anode of 0.072 m. The FFC had a cathode which varied from 0.042 m outer radius at the inlet to 0.053 m at the throat to 0.033 m at the thruster exit. Currents ranged from 20 kA to 60 kA with a mass flow of  $4 \times 10^{-3} \frac{kg}{s}$ . Onset appeared to occur at approximately 60 kA.

The numerical thruster is depicted in Figure 4. It consists of two concentric cylinders, of which the first 0.109 m of each is conducting, followed by a short insulating section of 0.031 m. The interelectrode gap is 0.02 m, with a cathode inner radius of 0.052 m. The plume is not included in the simulation. The mass flow of  $4 \times 10^{-3} \frac{kg}{s}$  is assumed to be injected through the whole backplate, with the mass flow per unit area constant at all radial locations. A number of different current levels, ranging from 23.4 kA up to 39.0 kA, were simulated. These currents are all well below the onset condition but span the region where large anode voltage drops develop.

As discussed in Section 1, simple theories and numerical models of MPD thrusters have always significantly underpredicted the total voltage of thrusters as observed in experiments. The data from Heimerdinger, as well as from other experiments discussed previously, indicate that the total voltage is distributed between a cathode fall voltage, a bulk plasma voltage, and an anode fall voltage. None of the existing theoretical or numerical results show the anode and cathode fall voltages, or adequately explain the cause of the anode falls. This is why the theoretical and numerical results predict voltages so much lower than those observed experimentally.

The model and simulation used in this research however does seem to reproduce the anode voltage drop behaviour seen by Heimerdinger. The anode voltage drops seen in the simulation occur in the quasi-neutral bulk plasma very near the anode. The voltage drops appear even though the model uses fluid equations and does not include the non-neutral anode sheath. These voltage drops occur because of the basic mechanism outlined in Section 3, as will be shown by the data presented herein.

Figure 5 shows the current lines for the baseline case, with the concentration of lines a measure of the current density. The plot is drawn so that the axial and radial dimensions are roughly in the correct proportions. The numbers on the plot indicate the approximate percentage of current enclosed by the nearest contour. As can be seen, the current is highly skewed near the anode, turning almost parallel to the electrode. This is because the axial component of the current is substantially larger than the radial component. The axial component is so large because the Hall parameter near the anode is quite large, reaching values as high as 100.

The Hall parameter is so high because of the low electron number density. The electron number density along five radial cuts is shown in Figure 6. The cuts are at the axial locations shown in the figure key. The electron number density decays from a maximum of  $2 \times 10^{21} m^{-3}$  near the cathode to a minimum of  $1 \times 10^{19} m^{-3}$  at the anode. The electron number density is dropping because both the ionization fraction and the total mass density are dropping near the anode. The ionisation fraction is low near both the cathode and the anode due to recombination of the ions at the wall. The low ionization fraction near the cathode, and the slight (relatively) drop in electron density there leads to a small cathode voltage drop.

The electron number density near the anode is so low because the plasma has been turned away from the anode by the radial Lorentz force. This turn is shown in Figure 8 where there is a region of large negative radial velocity near the backplate. Num-

bers on the plot show values at the local minima (-582, -177, -61, -346 m/sec) and the maximum value (754 m/sec). It is also illustrated by the streamlines, shown as the dotted lines in Figure 10. This turn leads to depletion of the plasma near the anode, as shown by the isobars (solid lines) of Figure 10. As shown by the streamlines, the plasma then turns back so that it is flowing almost parallel to the anode. This turn is accompanied by a drop in Mach number, to subsonic speeds along some streamlines. The initial acceleration and subsequent drop in Mach number are shown in Figure 9, contours of constant Mach number. The label A is at a local maximum of 1.57. As shown by the labelled Mach 1 contour, along a number of axial lines the plasma is dropping from supersonic to subsonic speeds. Along streamlines near the anode the plasma first sees decreasing pressure as it accelerates, and then increasing pressure as the streamlines straighten out. The current lines (solid lines) and constant potential contours (dotted lines) shown in Figure 11, also show a sharp transition in this region. Both 0.1 mm from the anode and along a ridge of high Hall parameter between  $z = 0.0015$  and  $z = 0.0075$ , the lines run almost parallel to each other, parallel to the anode very near the anode, and parallel to the backplate along the ridge. Further along the channel, as the pressure increases and the Hall parameter decreases, the angle between the lines becomes larger.

When the plasma parameters at the last interior point are input to the near anode boundary equations, they predict significant voltage drops, as shown in Figure 12, transverse cuts of the potential drop.

How do the anode voltage drops behave at different currents? Heimerdinger[7] directly measured the anode voltage drop over a range of currents in the FFC and at 60 kA in the CAC. The measured voltage drop is the difference between the potential measured 2 mm from the anode at an axial location of 0.043 m from the inlet, and the potential at the anode. His data are shown in Figure 13. The data show that at low applied currents, anode voltage drops are negligible or non-existent. As the applied current is increased, the voltage drops appear and increase with increasing applied current. The anode drops seem to level out as the total current is increased past 50-55 kA, although the large error bars make this difficult to ascertain. The one data point available for the CAC seems to indicate that the anode voltage drop in this thruster is somewhat smaller than in the FFC. In general, the anode drops seem to account for 50 - 75 % of the total terminal voltage in those cases for which the anode seems to be starved, i.e. for currents above 25 kA or so.

The numerically predicted voltage drops behave in a similar manner. Simulations were performed for the CAC at currents of 23.4 kA, 27.3 kA, 31.2 kA, 35.9 kA, and 39.0 kA. The computed numerical voltage drops are also plotted in Figure 13. At 23.4 kA, the voltage drops are quite small. As current is increased, the numerically predicted anode voltage drops grow, like the experimental data. The total potential drops from the experimental data and the numerical simulation are shown in Figure 14. Agreement gets better as the current is increased, although whether this trend will continue with current beyond 39 kA is unclear. The reason for the large discrepancy at low currents is also unclear. Possibly this is due to artificial ignition of the plasma in the low current numerical cases, due to the lower limit on ionisation fraction. It might also be due to excessive damping in the numerical simulation at low Mach numbers.

## 6 Conclusions

The analytical results demonstrate that starvation of the near anode plasma could result in significant voltage drops in the quasi neutral plasma. The computational results show that this mechanism causes voltage drops with behaviour and magnitude similar to those in an experimental device. As these voltage drops are a major cause of thruster inefficiency, understanding them should lead to improved thruster designs.

## References

- [1] D.A. Anderson, J.C. Tannehill, and R.H. Pletcher. *Computational Fluid Mechanics and Heat Transfer*. Hemisphere Publishing Corporation, New York, 1984.
- [2] F.G. Bakhst, B. Ya. Moishes, and A.B. Rybakov. "Critical Regime of a Plasma Accelerator". *Soviet Physics: Technical Physics*, 18(12):1613-1616, June 1974.
- [3] J. Fernandez de la Mora and R. Fernandez-Feria. "Two-Fluid Chapman-Enskog Theory for Binary Gas Mixtures". *Physics of Fluids*, 30(7):2063-2072, July 1987.
- [4] J.H. Ferziger and H.G. Kaper. *Mathematical Theory of Transport Processes in Gases*. American Elsevier Publishing Company, New York, 1972.
- [5] A.D. Gallimore, A.J. Kelly, and R.G. Jahn. "Anode Power Deposition in MPD Thrusters".

bers on the plot show values at the local minima (-582, -177, -61, -346 m/sec) and the maximum value (754 m/sec). It is also illustrated by the streamlines, shown as the dotted lines in Figure 10. This turn leads to depletion of the plasma near the anode, as shown by the isobars (solid lines) of Figure 10. As shown by the streamlines, the plasma then turns back so that it is flowing almost parallel to the anode. This turn is accompanied by a drop in Mach number, to subsonic speeds along some streamlines. The initial acceleration and subsequent drop in Mach number are shown in Figure 9, contours of constant Mach number. The label A is at a local maximum of 1.57. As shown by the labelled Mach 1 contour, along a number of axial lines the plasma is dropping from supersonic to subsonic speeds. Along streamlines near the anode the plasma first sees decreasing pressure as it accelerates, and then increasing pressure as the streamlines straighten out. The current lines (solid lines) and constant potential contours (dotted lines) shown in Figure 11, also show a sharp transition in this region. Both 0.1 mm from the anode and along a ridge of high Hall parameter between  $z = 0.0015$  and  $z = 0.0075$ , the lines run almost parallel to each other, parallel to the anode very near the anode, and parallel to the backplate along the ridge. Further along the channel, as the pressure increases and the Hall parameter decreases, the angle between the lines becomes larger.

When the plasma parameters at the last interior point are input to the near anode boundary equations, they predict significant voltage drops, as shown in Figure 12, transverse cuts of the potential drop.

How do the anode voltage drops behave at different currents? Heimerdinger[7] directly measured the anode voltage drop over a range of currents in the FFC and at 60kA in the CAC. The measured voltage drop is the difference between the potential measured 2 mm from the anode at an axial location of 0.043 m from the inlet, and the potential at the anode. His data are shown in Figure 13. The data show that at low applied currents, anode voltage drops are negligible or non-existent. As the applied current is increased, the voltage drops appear and increase with increasing applied current. The anode drops seem to level out as the total current is increased past 50-55 kA, although the large error bars make this difficult to ascertain. The one data point available for the CAC seems to indicate that the anode voltage drop in this thruster is somewhat smaller than in the FFC. In general, the anode drops seem to account for 50 - 75 % of the total terminal voltage in those cases for which the anode seems to be starved, i.e. for currents above 25 kA or so.

The numerically predicted voltage drops behave in a similar manner. Simulations were performed for the CAC at currents of 23.4 kA, 27.3 kA, 31.2 kA, 35.9 kA, and 39.0 kA. The computed numerical voltage drops are also plotted in Figure 13. At 23.4 kA, the voltage drops are quite small. As current is increased, the numerically predicted anode voltage drops grow, like the experimental data. The total potential drops from the experimental data and the numerical simulation are shown in Figure 14. Agreement gets better as the current is increased, although whether this trend will continue with current beyond 39 kA is unclear. The reason for the large discrepancy at low currents is also unclear. Possibly this is due to artificial ignition of the plasma in the low current numerical cases, due to the lower limit on ionization fraction. It might also be due to excessive damping in the numerical simulation at low Mach numbers.

## 6 Conclusions

The analytical results demonstrate that starvation of the near anode plasma could result in significant voltage drops in the quasi neutral plasma. The computational results show that this mechanism causes voltage drops with behaviour and magnitude similar to those in an experimental device. As these voltage drops are a major cause of thruster inefficiency, understanding them should lead to improved thruster designs.

## Acknowledgments

This work was supported by an Air Force Laboratory Graduate Fellowship. Supercomputer time was provided by the Nasa Lewis Research Center.

## References

- [1] D.A. Anderson, J.C. Tannehill, and R.H. Pletcher. *Computational Fluid Mechanics and Heat Transfer*. Hemisphere Publishing Corporation, New York, 1984.
- [2] F.G. Bakhst, B. Ya. Moizhes, and A.B. Rybakov. "Critical Regime of a Plasma Accelerator". *Soviet Physics: Technical Physics*, 18(12):1613-1616, June 1974.
- [3] J. Fernandez de la Mora and R. Fernandez-Feria. "Two-Fluid Chapman-Enskog Theory for Binary Gas Mixtures". *Physics of Fluids*, 30(7):2063-2072, July 1987.

- [4] J.H. Ferziger and H.G. Kaper. *Mathematical Theory of Transport Processes in Gases*. American Elsevier Publishing Company, New York, 1972.
- [5] A.D. Gallimore, A.J. Kelly, and R.G. Jahn. "Anode Power Deposition in MPD Thrusters". In *22nd International Electric Propulsion Conference, Italy*. AIDAA/AIAA/DGLR/JSASS, October 1991. IEPC 91-125.
- [6] D.J. Heimerdinger and M. Martinez-Sanchez. "Fluid Mechanics in a Magnetoplasmadynamic Thruster". In *20th International Electric Propulsion Conference, West Germany*. DGLR/AIAA/JSASS, October 1988. IEPC-88-039.
- [7] D.J. Heimerdinger. *Fluid Mechanics in a Magnetoplasmadynamic Thruster*. PhD thesis, Massachusetts Institute of Technology, January 1988.
- [8] D.J. Heimerdinger, D.B. Kilfoyle, and M. Martinez-Sanchez. "Experimental Characterization of Contoured Magnetoplasmadynamic Thrusters". In *24th Joint Propulsion Conference, Boston*. AIAA/ASME/SAE/ASEE, July 1988. AIAA Paper 88-3205.
- [9] D.B. Kilfoyle, M. Martinez-Sanchez, D.J. Heimerdinger, and E.J. Sheppard. "Spectroscopic Investigation of the Exit Plane of an MPD Thruster". In *20th International Electric Propulsion Conference, West Germany*. DGLR/AIAA/JSASS, October 1988. IEPC-88-027.
- [10] K. Kuriki, M. Onishi, and S. Morimoto. "Thrust Measurement of K III MPD Arcjet". *AIAA Journal*, 20(10), October 1982.
- [11] M.R. LaPointe. "Numerical Simulation of Self-Field MPD Thrusters". In *27th Joint Propulsion Conference, Sacramento CA*. AIAA/SAE/ASME/ASEE, June 1991. AIAA-91-2341.
- [12] M.R. LaPointe. "Numerical Simulation of Geometric Scale Effects in Cylindrical Self-Field MPD Thrusters". In *28th Joint Propulsion Conference, Nashville TN*. AIAA/SAE/ASME/ASEE, July 1992. AIAA-92-3297.
- [13] M.A. Lieberman and A.L. Velikovich. *Physics of Shock Waves in Gases and Plasmas*. Springer-Verlag, Berlin, 1986.
- [14] M. Martinez-Sanchez. "Structure of Self Field Accelerated Plasma Flows". *Journal of Propulsion and Power*, 7(1):56-64, January-February 1991.

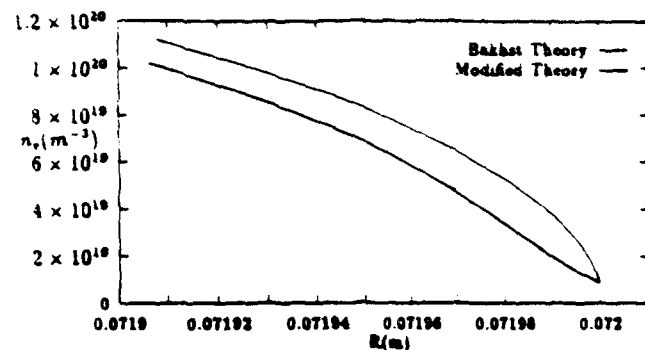


Figure 1: Electron Number Density, Analytical Models

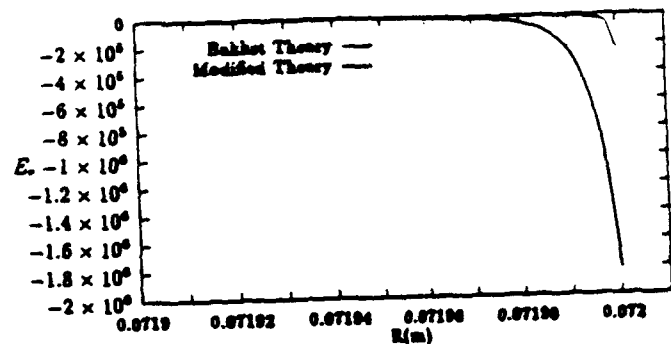


Figure 2: Radial Electric Field, Analytical Models

- [15] M. Mitchner and C. Kruger. *Partially Ionized Gases*. John Wiley and Sons, New York, 1973.
- [16] E. Sheppard. Private Communication.
- [17] J. S. Sovey and M. A. Mantieniks. "Performance and Lifetime Assessment of Magnetoplasmadynamic Arc Thruster Technology". *Journal of Propulsion and Power*, 7(1):71-83, 1991.

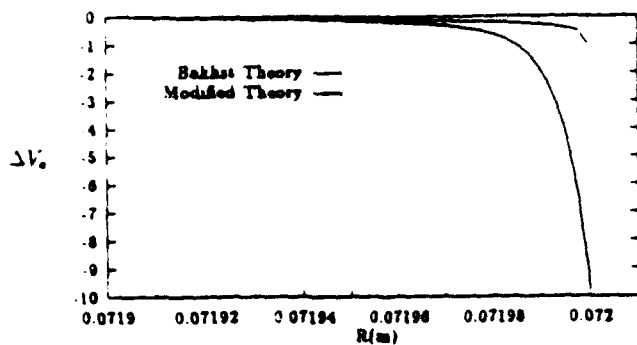


Figure 3: Anode Potential Drop, Analytical Models

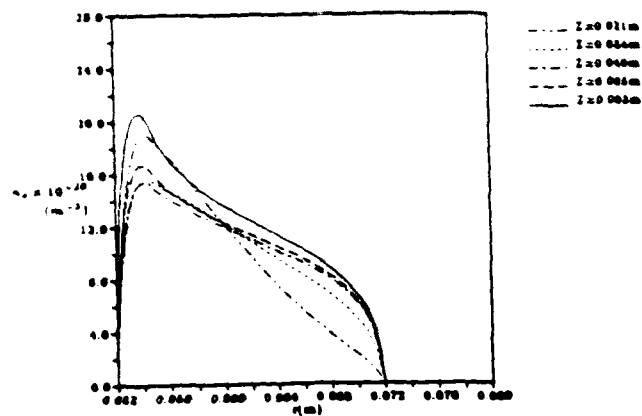


Figure 6: Radial Cuts of Electron Number Density

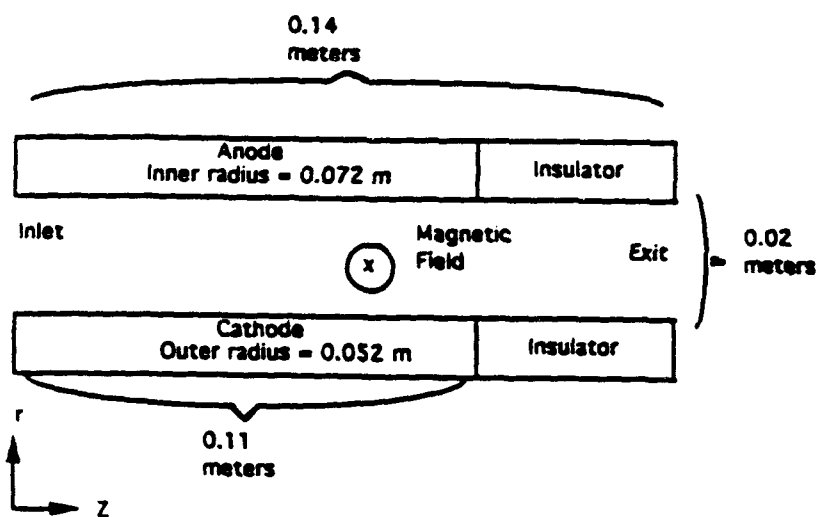


Figure 4: Numerical CAC Geometry

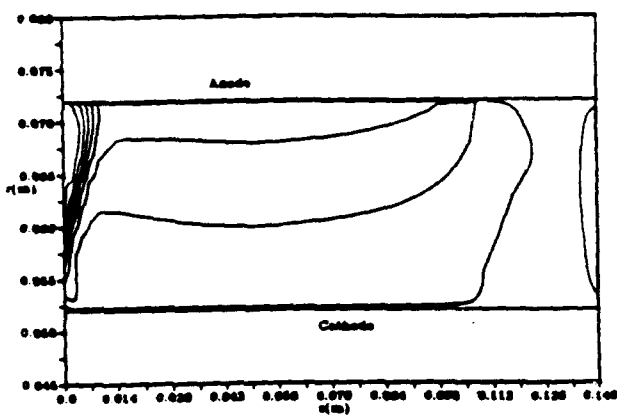


Figure 7: Constant Contours of Potential Drop

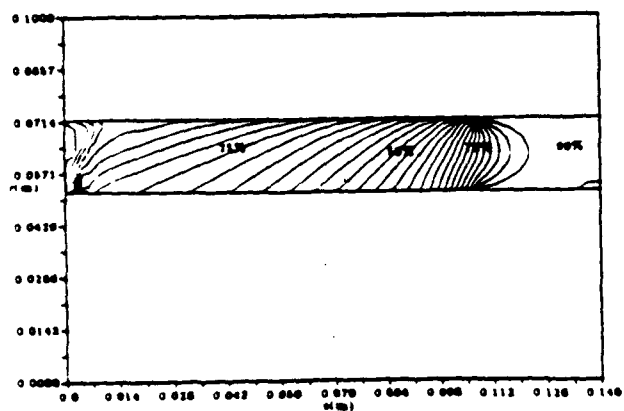


Figure 5: Current Lines in 31.2 kA CAC (Baseline)

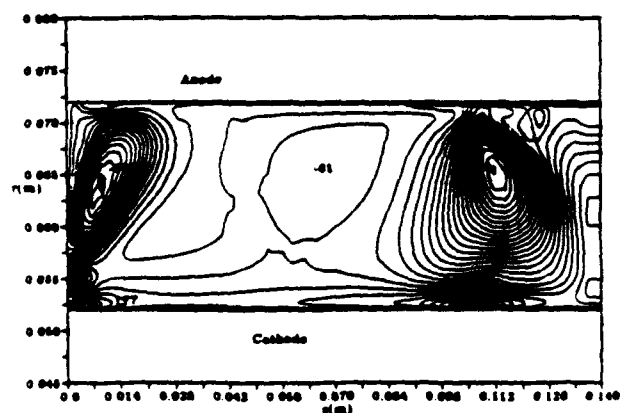


Figure 8: Radial Velocity Contours

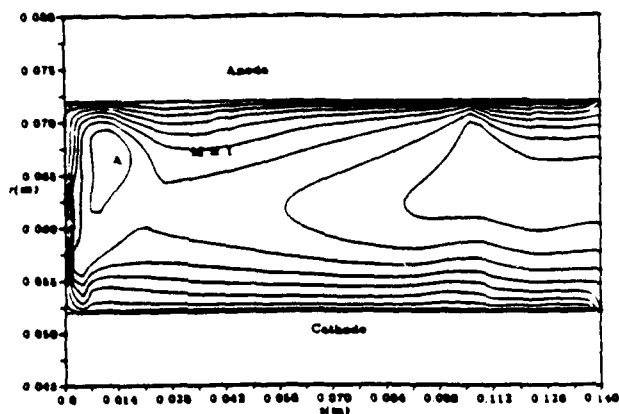


Figure 9: Mach Number Contours

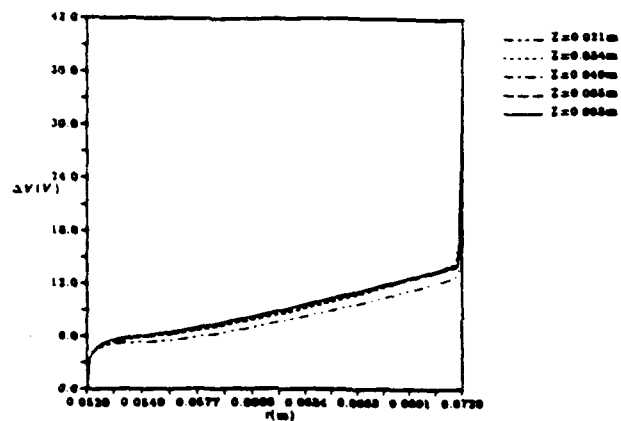


Figure 12: Radial Cuts of Potential Drop in 31.2 kA CAC (Baseline)

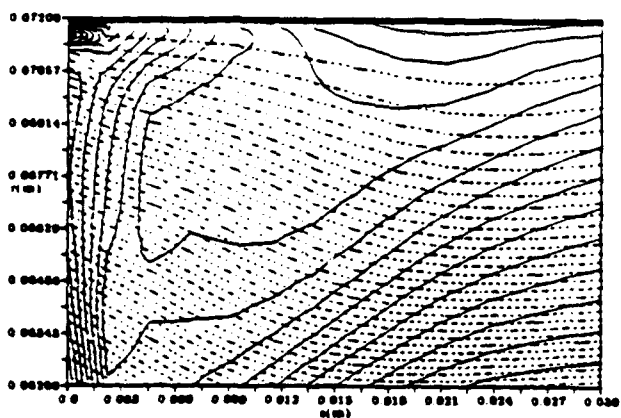


Figure 10: Stream Lines and Constant Pressure Contours

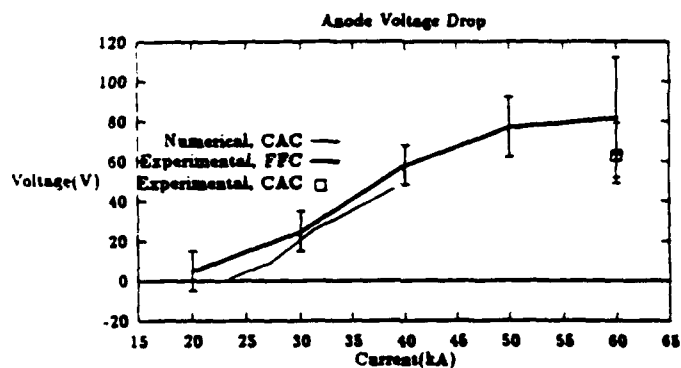


Figure 13: Experimental and Numerical Anode Voltage Drops

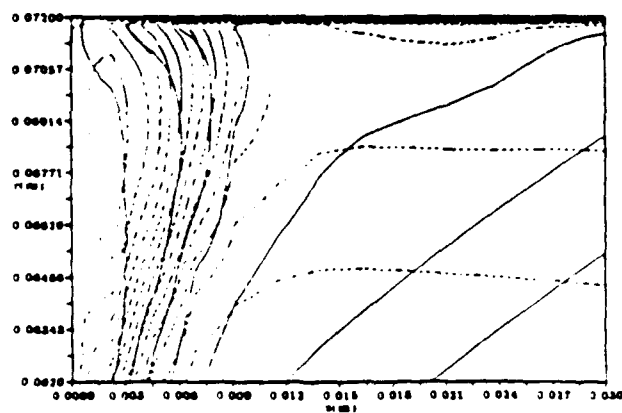


Figure 11: Current Lines and Constant Potential Contours

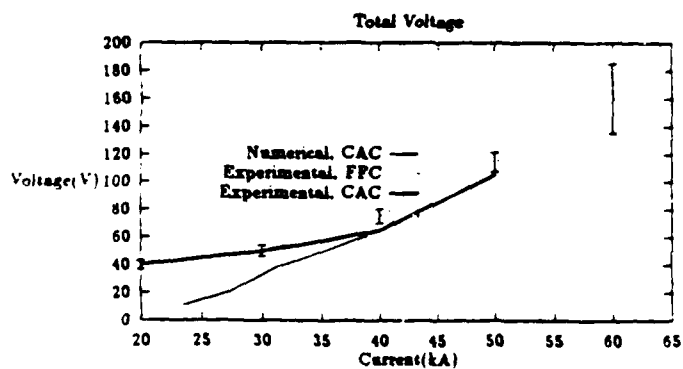


Figure 14: Experimental and Numerical Total Voltage Drops



**AIAA 93-1904**

**Simplified Analysis of Arcjet Thrusters**

M. Martinez-Sanchez and A. Sakamoto

Space Power and Propulsion Laboratory

Dept. of Aeronautics and Astronautics

MIT

Cambridge, MA

**AIAA/SAE/ASME/ASEE  
29th Joint Propulsion  
Conference and Exhibit**

June 28-30, 1992 / Monterey, CA



# SIMPLIFIED ANALYSIS OF ARCJET THRUSTERS

M. Martinez-Sanchez<sup>†</sup> and A. Sakamoto\*

Space Power and Propulsion Laboratory

Dept. of Aeronautics and Astronautics, MIT, Cambridge, MA 02139

## Abstract

For purposes of systems tradeoffs, as well as for preliminary design purposes, there is a need for relatively simple methods to estimate arcjet performance without the cost and delay of a full-fledged numerical study. We present here one such method, and its verification against a variety of test data.

## Nomenclature

$a$	$Ra/R$
$B^2$	Average slope of $\phi$ vs. $\sigma$
$E$	Axial electric field
$F$	Thrust
$G$	Average value of $h / \sigma$
$h$	Static enthalpy
$h_e$	Static enthalpy at arc edge
$H$	Total enthalpy
$\dot{H}$	Total enthalpy flux
$\dot{H}_a$	Enthalpy flux in arc
$I$	Arc current
$J$	Momentum flux
$K$	Thermal conductivity
$\dot{m}$	Total mass flow parameter (Eq. 41)
$\dot{m}_a$	Arc mass flow
$N$	Frozen flow parameter (Eq. 41)
$p, p_0$	Pressure, stagnation pressure
$q$	$\rho u^2$
$Q$	Effective value of $\gamma / \gamma - 1$
$r$	Radial coordinate
$R$	Radius of flow passage
$R_a$	Radius of arc
$T$	Temperature
$u$	Axial velocity
$V$	Arc voltage

$x$	Axial coordinate
$z$	$p/q$
$\gamma$	Specific heat ratio
$\theta$	$h/h_e$
$\phi$	Heat flux potential
$\rho$	Density
$\sigma$	Electrical conductivity

## 1 Introduction

The model is based on a two-stream approximation, plus a set of simplified relations for gas physical properties—enthalpy, conductivity, etc. The outer stream is treated as ideal adiabatic flow, with Ohmic heating and heat conduction limited to the inner ("arc") stream. Growth of this inner stream follows from heat diffusion across external streamlines. By postulating a reasonable set of radial shape functions for the conductivity and the dynamic head ( $\rho u^2$ ) the conservation laws become a set of ordinary differential equations, which must be integrated subject to prescribed initial conditions and to smooth passage through the sonic section. Several aspects of the actual physics are outside the scope of the model, and must be externally supplied. These include the arc attachment point and the anode voltage drop, plus a few less significant effects, such as the chemical freezing point or the initial centerline enthalpy. The results presented include a study of the sensitivity of predicted performance to these inputs.

The model was tested against an extensive set of data from Stuttgart University on a 20kw thruster, over a range of currents, flow rates, propellants and cooling methods, and also against data from two higher power and one smaller power thruster. Results include chamber pressure, thrust, voltage, arc radius and anode heat loss, plus derived quantities such as specific

<sup>†</sup>Professor, member AIAA

\*Graduate Student

impulse and efficiency. The agreement with data is reasonable good.

## 2 Formulation and Assumptions

The geometry considered is shown in Fig. 1. The region outside the arc ( $R > r > R_a$ ) is modeled as an isentropic flow region, where the gas convected from upstream has not yet been affected by the diffusive spread of heat coming from the arc itself ( $r < R_a$ ).

This is supported by photometric data [1], which show a sharply delineated arc boundary surrounding by non-emitting gas, and also by results of detailed 2-D simulations [3], according to which the buffer gas is actually colder than the walls, with a thin wall boundary layer of the order of 0.3 mm total thickness (for a constrictor diameter of 2.5 mm).

The arc itself is a region of intense Ohmic heating and radial heat conduction. Radiant heat transfer is comparatively negligible for arc diameters less than about 1 cm. Convection is, of course, the other important effect. Ignoring friction, the governing equations (conservation of mass, energy and momentum) can be integrated across the flow area ( $0 < r < R(x)$ ) to obtain

$$\frac{dm}{dx} = 0 \quad (1)$$

$$\frac{dH}{dx} = 2\pi R \left( K \frac{\partial T}{\partial r} \right)_W + EI \quad (2)$$

$$\frac{dJ}{dx} = p 2\pi R \frac{dR}{dx} \quad (3)$$

where the overall fluxes  $\dot{m}$ ,  $\dot{H}$  and  $J$  are

$$\dot{m} = \int_0^R \rho u 2\pi r dr \quad (4)$$

$$\dot{H} = \int_0^R \rho u \left( h + \frac{u^2}{2} \right) 2\pi r dr \quad (5)$$

$$J = \int_0^R (p + \rho u^2) 2\pi r dr \quad (6)$$

The total current  $I$  in Eq. (2) is calculated from Ohm's law as

$$I = E \int_0^R \sigma 2\pi r dr \quad (7)$$

where  $E$  is the axial electric field, and  $\sigma$  is the electrical conductivity of the gas. The current is kept invariant with  $x$  up to the attachment cross-section, where it goes abruptly to zero.

The wall heat flux term in Eq. (2) will be neglected, except in the anode attachment region as will be discussed below. Accordingly, Eq. (9) gives for the electric potential from the cathode tip

$$V - \Delta V_c = \frac{H - H(0)}{I} \quad (8)$$

where  $\Delta V_c$  is the cathode potential drop, and  $H(0)$  is the axial enthalpy flux at the cathode tip section. In the anode attachment region, the quasi-one dimensionality is locally violated, and a large radial electric field does occur leading to the observed anode drop,  $\Delta V_A$ . The energy  $\Delta V_A$  dissipated in this region is mainly absorbed by the wall, and the axial enthalpy flux  $\dot{H}$  must therefore decrease by  $-\Delta \dot{H} = I \Delta V_A$ .

The axial evolution of the arc mass flux  $\dot{m}_a$  which is defined as in Eq. 4, but with the upper limit changed to  $R_a(x)$ , is governed by the diffusive spread of the region of heated gas, which covers a steadily increasing number of stream tubes. This fact will be used here to formulate a simple growth model. Even though the enthalpy radial profile  $h(r)$  is in reality continuous, it is, as we noted, very steep at the edge of the arc. This partly due to the counterflow heat diffusion, but also the very rapid variation of electrical conductivity with temperature in the 5000-7000 K region, where the gas begins to ionize thermally. Since the heating rate is  $\sigma(T)E^2$  once a temperature  $T_e \sim 6000$  K is reached, dissipation increases rapidly with further  $T$  increases, and the  $T$ -profile must steepen. Consider an idealized situation as shown in Fig. 4, where  $h_c(x)$  is the arc centerline enthalpy,  $h_{out}(x)$  is the adiabatic outer enthalpy, and  $h_e$ , corresponding to  $T_e \cong 6000$  K, is the arc-edge enthalpy. If the arc is "ingesting" gas at the rate  $\frac{d\dot{m}_a}{dx}$ , the amount of heat  $(h_e - h_{out}) \frac{d\dot{m}_a}{dx}$  must be supplied to this region per unit length (more precisely, total enthalpies should be used,

including kinetic energies). This heat is supplied by radial conduction. If

$$q_c = \left( -K \frac{\partial T}{\partial r} \right)_{R_a}$$

is the radial heat flux at the arc edge, we obtain

$$(h_e - h_{out}) \frac{dm_a}{dx} = 2\pi R_a q_c \quad (9)$$

Turning now to the momentum equation, the overall conservation law (Eq. 3) needs to be supplemented by some other equation which expresses the character of the axial momentum balance. Since the dynamic head  $\rho u^2$  which develops gradually in the arc-heated duct is generated by the gradual drop in pressure and  $p$  is radially uniform, it can be reasonably expected that  $\rho u^2$  itself will also be nearly independent of  $r$ . This is confirmed by inspection of full 2-D solutions, such as those shown in Refs. 2,4.

## 2 Approximation for Gas Properties and Radial Profiles

In the interest of algebraic simplicity, we would like to interrelate the gas enthalpy, thermal and electrical conductivity, pressure and density in as simple a fashion as possible, while preserving the basic physics. The following approximations have been found reasonable and useful:

$$(a) \quad h \equiv Q \frac{p}{\rho} \quad (10)$$

Of course, for an ideal gas,  $Q = \frac{\gamma}{\gamma - 1}$ ,  $\gamma$  being

the specific heat ratio. For a diatomic gas, then,  $Q=3.5$ , and for a monatomic gas  $Q=2.5$ . For a non-ideal gas undergoing dissociation and ionization,  $\gamma$  will approach unity, and  $Q$  can be rather large over limited  $T$  intervals. From data collected, for example by Lee (Ref. 5)  $Q$  is on average 7-8 for  $H_2$  and  $N_2$  over a broad interval, to over 30,000K. The parameter  $Q$  (and others) is given in Table 1 for  $N_2$  and  $H_2$ , as well as for  $N_2H_4$ , for which simple molar averaging has been used.

(b) The thermal conductivity  $K$  has very sharp peaks (due to molecular diffusion followed by recombination) in the dissociation and ionization ranges. Fortunately, the quantity of interest is the so-called heat-flux potential.

$$\phi = \int_0^T K dT \quad \left( K \frac{\partial}{\partial T} = \frac{\partial}{\partial \phi} \right) \quad (11)$$

which varies more smoothly. In fact,  $\phi$  is almost linearly related to the electrical conductivity  $\sigma$ , as shown in Fig. 3 for Hydrogen at 1 atm. We adopt the form

$$\phi \equiv \phi_0 + B^2 \sigma \quad (12)$$

with parameters  $\phi_0$  and  $B$  as shown in Table 1.

(c) It is also useful to relate the enthalpy  $h$  to the electrical conductivity  $\phi$ . Fig. (4) shows this relationship for hydrogen at 1 atm. To a rough approximation, we will use

$$h \equiv G\sigma \quad (13)$$

with  $G$  also specified in Table 1

These correlations are relatively insensitive to pressure; some correction is included in the model to account for the Spitzer logarithm effects [7].

The radial variations of velocity, mass flux, enthalpy flux and kinetic energy can now be expressed in terms of only those of the enthalpy. We define

$$q(x) = \rho u^2 \quad (\text{independent of } r) \quad (14)$$

and obtain

$$u = \sqrt{\frac{\rho u^2}{\rho}} = \sqrt{\frac{q}{p \rho}} = \sqrt{\frac{q}{Q p}} \sqrt{h} \quad (15)$$

$$\rho u = \sqrt{\rho(\rho u^2)} = \sqrt{\frac{p}{p/\rho}} q = \frac{\sqrt{Q p q}}{\sqrt{h}} \quad (16)$$

$$\rho u h = \sqrt{Q p q} \sqrt{h} \quad (17)$$

$$\rho u \frac{u^2}{2} = q \frac{u}{2} = \frac{q}{2} \sqrt{\frac{q}{Q p}} \sqrt{h} \quad (18)$$

and hence

$$\rho u h_t = \rho u \left( h + \frac{u^2}{2} \right) \quad (19)$$

$$= \left( 1 + \frac{1}{2Q} \frac{q}{p} \right) \sqrt{Q p q} \sqrt{h}$$

In these expressions, the factors involving  $Q$ ,  $p$  and  $q$  are independent of  $r$ . These expressions indicate a large velocity, but a small mass flux inside the arc, where  $h$  is high. The enthalpy flux is large, but only in proportion to  $\sqrt{h}$  rather than to  $h$ , as one might have expected.

It is clear then, that the specification of the radial variation of, say, electrical conductivity, would suffice to specify those of all the quantities needed to evaluate the integrals  $\dot{m}$ ,  $\dot{m}_a$ ,  $H$  (since  $\sigma$  is related to  $h$  by Eq. (13)). A two-parameter profile is adopted, of the form.

$$\sigma = \sigma_c(x) f(r/R_a(x)) \quad (20)$$

and a convenient form for  $f$  is obtained by consideration of the simpler problem of an arc which fills a cylindrical cooled wall of radius  $R_a$ :

$$\sigma = \sigma_c J_0 \left( 2.405 \frac{r}{R_a} \right) \quad (21)$$

where  $J_0(y)$  is the zero'th order Bessel function, whose first zero is at  $y=2.405$ . In the purely cylindrical case, the relationship  $E=2.405 \frac{B}{R_a}$  is obtained from the radial heat balance. Since we now have substantial convective cooling, this is

not a good approximation, although it does show the correct trends.

Because of Eq. (13), this also gives the enthalpy profile:

$$h(r, x) = h_c(x) J_0 \left( 2.405 \frac{r}{R_a(x)} \right) \quad (22)$$

Substituting Eq. (21) into the total current expression (Eq. 7) gives

$$\begin{aligned} I &= 2\pi E \sigma_c \int_0^{R_a} J_0 \left( 2.405 \frac{r}{R_a} \right) r dr \\ &= 1.356 E \sigma_c R_a^2 \end{aligned} \quad (23)$$

This expresses the axial field  $E$  and the dissipation per unit length,  $EI$ , in terms of  $I$ ,  $\sigma_c$  and  $R_a$ . The heat flux  $q_c$  at the arc edge needed in Eq. (9) can also be evaluated now:

$$\begin{aligned} 2\pi R_a q_c &= -2\pi R_a \left( \frac{d\phi}{dr} \right)_{R_a} = 2\pi R_a B^2 \left( \frac{d\sigma}{dr} \right)_{R_a} \\ \text{or } 2\pi R_a q_c &= 7.843 B^2 \sigma_c \end{aligned} \quad (24)$$

Finally, we can use Eq. (22) to evaluate the mass and energy flux integrals. For the arc mass flow,

$$\begin{aligned} \dot{m}_a &= \int_0^{R_a} \rho u \cdot 2\pi r dr = \\ &= \frac{2\pi}{\sqrt{h_c}} \left( \frac{R_a}{2.405} \right)^2 \left[ \int_0^{2.405} \frac{x dx}{\sqrt{J_0(x)}} \right] \sqrt{Q p q} \\ &= 7.634 \sqrt{Q} \sqrt{p q} \frac{R_a^2}{\sqrt{h_c}} \end{aligned} \quad (25)$$

The mass flow rate outside the arc is easier to evaluate, because  $h=h_{out}=const.$  in that region. We obtain

$$\begin{aligned} \dot{m} - \dot{m}_a &= (\rho u)_{out} \pi (R^2 - R_a^2) = \\ &= \pi \sqrt{Q_{out}} \sqrt{p q} \frac{R^2 - R_a^2}{\sqrt{h_{out}}} \end{aligned} \quad (26)$$

where we have used  $Q_{out}$  instead of the  $Q$  value, which is appropriate only to the high temperature region. For  $H_2$  or  $N_2$  we can use  $Q_{out}=3.5$  ( $\gamma=1.4$ ).

For the total enthalpy flux in the arc,

$$H_a = \int_0^{R_a} \rho u \left( h + \frac{u^2}{2} \right) 2\pi r dr =$$

$$2\pi \left( 1 + \frac{1}{2Q} \frac{q}{p} \right) \sqrt{Qqp} \sqrt{h_c} \frac{R_a^2}{(2.405)^2}$$

$$\left[ \int_0^{2.405} \sqrt{J_0(x)} x dx \right]$$

the new integral is calculated to be 1.762, giving

$$\dot{H}_a = 1.914 \left( 1 + \frac{1}{2Q} \frac{q}{p} \right) \sqrt{Q} \sqrt{pq} h_c R_a^2 \quad (27)$$

Again, the enthalpy flux outside the arc is simpler. Using Eq. (19) we obtain

$$\dot{H} - \dot{H}_a = \pi \left( 1 + \frac{1}{2Q_{out}} \frac{q}{p} \right) \sqrt{Q_{out}}$$

$$\sqrt{pq h_{out}} (R^2 - R_a^2) \quad (28)$$

### 3 Integration in the Axial Direction

We compile here the relevant governing equations. Non-dimensional arc radius and enthalpies are introduced as  $a = \frac{R_a}{R}$

$$\theta_c = \frac{h_c}{h_e}, \quad \theta_{out} = \frac{h_{out}}{h_e}, \text{ and, using Eqs.}$$

(1,2) (with zero wall heat flux), (3) and (9), and expressing the dissipation and the arc-edge heat flux from Eqs. (23) and (24), we obtain

$$\dot{m} = \text{const.} \quad (29)$$

$$\frac{d\dot{m}}{dx} = 7.843 \frac{B^2}{G} \frac{\theta}{1 - \theta_{out}} \quad (30)$$

$$\frac{dJ}{dx} = p \, 2\pi R \frac{dR}{dx} \quad (31)$$

$$\frac{dH}{dx} = \frac{G I^2}{1.356 h_e \theta_c} \frac{1}{R^2 a^2} \quad (32)$$

$$\theta_{out} = \theta_{out,0} \left( \frac{p}{p_0} \right)^{\frac{\gamma-1}{\gamma}} \quad (33)$$

The integral quantities ( $\dot{m}$ ,  $\dot{m}_a$ ,  $J$  and  $\dot{H}$ ) are related to the primitive variables ( $p$ ,  $q$ ,  $a$ ,  $\theta_c$ ) by

$$\dot{m}_a = 7.364 \sqrt{\frac{Q}{h_e}} \sqrt{\frac{pq}{\theta_c}} R^2 a^2 \quad (34)$$

$$\dot{m} = \dot{m}_a + \pi \sqrt{\frac{Q}{h_e}} \sqrt{\frac{pq}{\theta_{out}}} R^2 (1 - a^2) \quad (35)$$

$$J = \pi R^2 (p + q) \quad (36)$$

$$\dot{H} = R^2 \sqrt{h_e} \left[ 1.914 \left( 1 + \frac{q/p}{2Q} \right) \sqrt{Q} a^2 \sqrt{\theta_c} \right.$$

$$\left. + \pi \left( 1 + \frac{q/p}{2Q_{out}} \right) \sqrt{Q_{out}} (1 - a^2) \sqrt{\theta_{out}} \right] \sqrt{pq} \quad (37)$$

Thus, after advancing one step in the axial direction, the set of non-linear equations (34-37) must be solved for ( $p$ ,  $q$ ,  $a$ ,  $\theta_c$ ) which then can be used to evaluate the axial derivatives and repeat the cycle.

Equations (34-37) can be reduced to a single nonlinear equation in the quantity  $z=q/p$ , which for an ideal gas would be equivalent to  $\gamma M^2$ ,  $M$  being the Mach number. The quantities  $\dot{m}_a$ ,  $\dot{H}$  and  $J$ , which are known from the integration's to the current  $x$  location, are parameters in this equation for  $z$ . This equation can have two, one or no roots. Starting from the low-speed end, where  $\dot{m}_a$  is small, two roots

occur, of which one can be identified as the desired subsonic solution. As  $\dot{m}_a$  increases, and if  $P_o$  is too high for the given  $\dot{m}$ , the end of the constrictor is reached within this subsonic branch. Continuation into the widening nozzle region then leads to a Venturi-type solution, which fails to expand the flow supersonically. On the other hand, a  $P_o$  which is too low leads to a situation where no solutions exist beyond a certain point in the constrictor. The correct  $P_o$  is such as to place the sonic point at the constrictor exit, such that the sudden area divergence allows the solution to transition smoothly into the supersonic branch. The solution itself is accomplished at each  $x$  value in a few Newton-Raphson iterations.

Once  $z=q/p$  is known, the remaining primitive variables can be easily found:

$$p + q = \frac{J}{\pi R^2} = s ; \quad p = \frac{s}{1+z} ; \quad q = zp \quad (38)$$

$$\theta_c = 5.495 \left[ \sqrt{\frac{Q}{h_e}} \frac{\sqrt{z}}{1+z} \frac{J}{\dot{m}_a} - \sqrt{\frac{Q}{Q_{out}}} \frac{\dot{m}_{out}}{\dot{m}_a} \sqrt{\theta_{out}} \right]^2 \quad (39)$$

$$a = \sqrt{\frac{1+z}{\sqrt{z}}} \frac{0.4266}{\sqrt{Q/h_e}} \frac{\sqrt{\theta_c}}{J/\dot{m}_{out}} \quad (40)$$

#### 4 Nozzle Expansion, Frozen Flow and Other Effects

Once the flow enters the divergent nozzle, the pressure falls rapidly, and chemical reaction rates fails to keep up with the evolving conditions (frozen flow). From the thermodynamic viewpoint, the principal consequence of this is that the failure to recombine keeps large amounts of heat of recombination from becoming thermal energy, which could then be converted to directed kinetic energy by the nozzle. Formally speaking, the curve of enthalpy  $h$  vs.  $p/\rho$  will have a slope

$$Q_{fr} = \gamma / (\gamma - 1) \text{ corresponding to a non-}$$

reacting mixture of mono- and diatomic molecules, rather than the much steeper  $Q$  which is used for the hot, reacting gas in the arc upstream of the freezing point.

Assuming  $h$  is still linear with  $p/\rho$ , but with the new slope, and further, that fluid elements move along lines of constant  $r/R_a(x)$ , it

can be shown [7] that this effect can be characterized by the parameter

$$N(x) = \sqrt{\frac{Q}{Q_{fr}} - \left( \frac{Q}{Q_{fr}} - 1 \right) \frac{h_c(x_{fr})}{h_c(x)}} \quad (41)$$

which reduces to unity when  $Q_{fr}=Q$ . The factor

$1 + \frac{q/p}{2Q}$  in Eq. (27) (for  $H_a$ ) should now be

replaced by  $1/N + \frac{q/p}{2Q}N$ , while a factor  $1/N$

should multiply the right-hand side of Eq. (25)

(for  $\dot{m}_a$ ). Similarly, Eq. (39) should have a

factor of  $1/N^2$ , and Eq. (40) a factor  $\sqrt{N}$ . The iteration for  $z$  is now slightly more involved, because  $N$  itself depends on  $z$ , but this is easily accounted for by using Eqs. (39) and (41) at each step of the iteration.

The physics of the anode region is beyond the scope of this model. Experimental evidence suggests that the arc attaches near the beginning of the supersonic nozzle if the walls are hot, and somewhat further downstream if they are cold. The voltage drop  $\Delta V_A$  in this attachment is also difficult to predict from first principles. Experiments on the German TT1 thruster [2] which is water-cooled, and on its radiation cooled counterpart [1] show that  $\Delta V_A$  is higher by ~20V in the case where the walls are cold.

Numerical experimentation with the present model shows that the fraction  $a=R_e/R$  continues to increase in the nozzle, as it should in the presence of heat diffusion. This, plus the expansion of  $R(x)$  itself, makes the "arc" radius increase rapidly, reducing its cooling rate, and hence its axial electric field. Beyond a few constrictor diameters into the nozzle, the arc voltage increases very little, and arbitrarily moving the attachment point up or downstream has only a minor effect on total voltage. For the numerical applications reported here, we have assumed attachment at the constrictor exit for hot-wall cases, and about 2 constrictor diameters into the nozzle for cold walls.

Wall friction is a relatively small effect in arcjets, but it does have some effect on the net performance, mainly by reducing the nozzle efficiency. We have used a relatively crude model to account for it. This consists of adding

to the integral momentum equation a frictional term derived from the numerical simulations of Ref. 3. For the constrictor, this amounts to a friction factor  $c_f=0.015$ . In the nozzle,  $c_f$  is allowed to decrease according to a flat-plate formula.

### 5 Arcjet Performance, Method of Calculation

The vacuum thrust of the arcjet is given by

$$F = \int_0^R \rho u^2 2\pi r dr + (p\pi R^2)_{exit} \quad (42)$$

$$\text{or } F = \left[ \pi R^2 (p + q) \right]_{exit} = J_{exit} \quad (43)$$

and, in fact, the impulse  $J(x)$  gives the thrust that would result by terminating the nozzle at the current  $x$  station. Specific impulse and efficiency then follow from standard definitions. Computations are performed according to the following sequence:

- (1) Specify geometric parameters, nozzle contour, etc.
- (2) Specify initial outer temperature  $T_{out}(0)$  (actually at the cathode tip).
- (3) Prescribe the anode attachment point  $x_{att}$  and the anode voltage drop  $\Delta V_A$ .
- (4) Specify mass flow  $\dot{m}$  and current  $I$ .
- (5) Guess an initial pressure  $p_0$ .
- (6) Integrate forward to the constrictor exit and check for smooth sonic passage. If not achieved, modify  $p_0$  and repeat.
- (7) When smooth sonic passage achieved, continue integration to attachment point. At  $x=x_{att}$ , add  $\Delta V_A$  to voltage, subtract  $I\Delta V_A$  from  $\dot{H}$ .
- (8) Continue to nozzle exit. Calculate thrust, specific impulse

$$I_{sp} = \frac{1}{g} \frac{F}{\dot{m}}, \text{ efficiency } \eta = \frac{F^2}{2\dot{m} I V}$$

Some additional details must be discussed about the initial values used to start the computation. As noted, the chamber pressure  $p_0$  is found by the sonic passage condition. Less clearly defined are the arc parameters (radius and temperature) right at the cathode tip where the integration starts. It is found that a fairly wide

latitude exists in the choice of  $a(0)=R_a(0)/R$  and of  $\theta_c(0) = h_c(0)/h_e$ . The effect of a change in either of these parameters is only felt in the near vicinity of the cathode, and the arc behavior in the constrictor is very nearly independent of these changes. The procedure adopted is therefore to select  $a(0)$  and  $\theta_c(0)$  such as to generate smooth profiles of  $a(x)$ ,  $\theta_c(x)$  near the cathode. Typically this leads to  $a(0) \sim 0.2-0.3$  and  $\theta_c(x) \sim 15-30$  (based on  $h_e \approx h(6000K)$  for the gas considered).

### 6 Results and Comparison to Data

The medium-power (6-30 kW) arcjets of References (1,2,6) have been very well documented experimentally, and constitute an excellent test bed for theoretical models. They cover a wide range of flow rates (0.05-0.3 g/sec), currents (50-200 Amp) propellants ( $H_2$ ,  $N_2$  +  $H_2$ , Argon) and cooling arrangements (water cooling, radiation cooling). Measured quantities include voltage, stagnation pressure, heat loss and its distribution, thrust and, in some cases, arc radius and constrictor pressure.

The basic TT1 thruster is water-cooled with segmented copper nozzle and constrictor. The constrictor has a length of 5mm and a diameter of 2.5mm. The area ratio of the supersonic nozzle is 100:1 with a 17.5° mean nozzle angle. The cathode has a conical tungsten tip with a 30° cone angle, mating to a similar conical chamber wall from which it is separated by a 2 mm axial gap.

Calculations and data for the extreme values of mass flow rate and current reported in Ref. [2] are compiled in Table 2. As noted in the table, attachment was throughout assumed at  $x=9$  mm (3.2 mm past the constrictor end). The anode drop  $\Delta V_A=28V$  was kept the same for all cases, and was selected so as to provide the best match to measured voltages. As the  $Q_{LOSS}$  column shows, this  $\Delta V_A$ , times the total current, also matches reasonably well against the experimentally measured total heat loss. The selected values of  $h_c(0)$  and  $a(0)$  are arbitrary (see discussion in Sec. 5) but insensitive.

The initial outer temperatures  $T_{out,0}=700$  K at 0.1 g/sec, 500K at 0.3 g/sec are reasonable values for the gas which has been in contact with (on the outside) the water-cooled copper wall, and (on the inside) the hot tungsten

cathode. It was found that the chamber pressure  $p_o$  varied with  $T_{out,o}$  roughly as  $\sqrt{T_{out,o}}$ . This is due to the fact that most of the mass flow at the choking plane is in fact in the outer flow region, so that by the choking relation  $\dot{m} = p_o A^* / \sqrt{T_{out,o} \cdot p_o} = \sqrt{T_{out,o}}$  for a fixed  $\dot{m}$ . Because of this the thrust  $F$  also increased with  $T_{out,o}$ . The good match achieved for both  $p_o$  and  $F$  against experiment validates the selection of  $T_{out,o}$ . The higher  $T_{out,o}$  selected for the lower flow rates attempts to reflect the higher (power/mass flow) for such cases, and does appear to yield proper results.

Inspection of Table 2 shows that all the performance parameters are predicted to within 10% (most of them significantly better than this). Of course, the voltage match is largely enforced by the  $\Delta V_A$  choice, and that of the thrust is helped by the  $T_{out,o}$  choice. However, the latter is only moderately affected by variations of  $T_{out,o}$  within the physically reasonable range. For example, for  $\dot{m} = 0.3 \text{ g/sec}$  and  $I = 150 \text{ A}$ , using  $T_{out,o} = 700\text{K}$  instead of the 500K of Table 2 would change the thrust from 1.64 to 1.80, a 10% variation.

Trends with mass flow and current are well reproduced. In particular, the slight decrease of voltage with current is accurately predicted. The increase in voltage with mass flow is also well reproduced.

Ref. (1) reported experiments in which a 2mm diameter observation window, centered 2.6 mm downstream of the cathode tip was used to optically observe the arc and also to measure static pressures. A comparison of measured and calculated arc widths is shown in Fig. 5. The excellent agreement further verifies the model's validity.

For the radiation-cooled case, reported in Ref. (1), the geometry was the same, but a monolithic tungsten anode was used instead of the water-cooled segments. The outside temperature of the anode block was measured and varied from 1200°C to 1800°C depending on current. Internal temperatures were modeled numerically and were estimated to yield

$T_{gas} \approx 800^\circ\text{C}$  at the chamber inlet a low power (2kW) case. This is not sufficient information to calculate  $T_{out,o}$  accurately, but a reasonable

estimate can be made of  $T_{out,o} = 1400\text{K}$  for  $\dot{m} = 0.1 \text{ g/sec}$ .

The anode heat loss was not directly measured in these tests, but the observed voltage decrease of 30-40V with respect to the water-cooled case suggests that the anode drop must have become very small indeed. In fact, even allowing for  $\Delta V_A = 0$  and for an earlier arc attachment (at the constrictor exit), we cannot obtain such a large decrease in voltage, as shown in Table 3. As a consequence, even though the thrust prediction is fairly accurate, the efficiency is underestimated by the model. The chamber pressure was not measured, and it is conceivable that  $T_{out,o}$  should be raised somewhat in order to effect a better thrust prediction by increasing  $p_o$ , but this would exacerbate the voltage overprediction problem. It is possible that the anode attachment may occur even before the end of the constrictor, or that at least a part of the current is reaching the anode there; however, the data were insufficient to verify this.

Some calculations were also done for a similar radiation-cooled 30 kW hydrogen thruster from NASA-Lewis RC (Ref. 8). This had a constrictor radius of 0.89 mm, constrictor length of 3.56mm and a 20° nozzle with 270:1 expansion. Results are shown in Table 4. Once again,  $\Delta V_A = 0$  is required, but here, both thrust and voltage are well predicted once this choice is made.

The results for the higher-powered HIPARC thruster [9], which had a constrictor of 3 mm radius and 6 mm length, with a 114:1, 20° nozzle, were similarly accurate at 0.2 g/sec, 500 A:  $V_{\text{predicted}} = 94.6\text{V}$  (including a 6V  $\Delta V_A$ ) vs.  $V_{\text{measured}} = 96\text{V}$ , and  $F_{\text{pred.}} = 1.80\text{N}$  vs.  $F_{\text{meas.}} = 1.96\text{N}$ . On the other hand, at 0.3 g/sec, 800A., while the same  $\Delta V_A$  leads to  $V_{\text{pred.}} = 102\text{V}$  vs.  $V_{\text{meas.}} = 103\text{V}$ , the model gives  $F_{\text{pred.}} = 2.64\text{N}$ , while the data of Ref. [9] indicates  $F_{\text{meas.}} = 3.40\text{N}$ . Inclusion of self-magnetic (MPD) effects accounts for about 0.2N only, so a substantial discrepancy remains. It should be noted that the thrust coefficient implied by the data is  $(C_F)_{\text{meas.}} = 2.46$ , much larger than the values seen in other thrusters and in the model, and perhaps unrealistic.

Even though the molar averaging procedure used to generate the coefficients for  $N_2H_4$  in Table 1 may be open to criticism, the model is able to make accurate predictions for hydrazine-fueled thrusters as well. This is shown



in Table 5, which pertains again to the TT1 water-cooled thruster of Ref. [1]. As in the voltage data, in this case a constant 20V for all cases. Chamber pressures and thrusts are then well predicted for a range of flows and currents.

## 7 Conclusions

A fairly simple model which retains only the essential facts about the physics of the arc and the flow process has been shown to be able to predict most of the important performance parameters of arcjets with an accuracy comparable with water-cooled H<sub>2</sub> case, a substantial anode drop is seen to be required to match the refined numerical simulations. A notable exception is the model's inability to calculate anode drops, for which the near-anode region needs to be modeled to the extent of including temperature non-equilibrium and charge carrier diffusion (Ref. 3). A second shortcoming is the need to provide separate estimates of the temperature of the gas outside the arc; this should be amenable to relatively simple thermal analysis, however. The model could prove useful for preliminary design and for broad systems studies, where the high costs of detailed simulations may be still prohibitive.

## References

- (1) B. Glocker, Th. Rösger and A. Laxander. "Medium Power Arcjet Analysis and Experiments", IEPC-91-016, Viareggio, Italy, 1991.
- (2) B. Glocker, M. Auweter-Kurtz, T.M. Goeltz, H.L. Kurtz and H.O. Schrade, "Medium Power Arcjet Thruster Experiments", AIAA 90-2531, Orlando, FL, 1990.
- (3) S.A. Miller and M. Martinez-Sanchez, "Multifluid Non-Equilibrium Simulation of Electrothermal Arcjet". AIAA/SAE/ASME/ASME 29th Joint Propulsion Conference, June 1993, Monterrey, CA.
- (4) Watson, V.R. and Pegot, E.B., "Numerical Calculations for the Characteristics of a Gas Flowing Axially through a Constricted Arc: NASA TN D-4042 91967).
- (5) Lee, J.H., Physics and Engineering of High Power Switching Devices, MIT Press, 1975.
- (6) Tosti, E. Glocker, B. and Trippi, A., "Final Results of 15 KWe Water-cooled Arcjet Testing". IEPC-91-014, Viareggio, Italy, 1991.
- (7) Atsuko Sakamoto, "Simplified Analysis of Arcjet Thrusters", MS Thesis, MIT, Dept. of Aeronautics/Astronautics. Feb. 1993.
- (8) Haag, T.W. and Curran, F.M., "High Power Hydrogen Arcjet Performance", AIAA-91-2226, 27th Joint Propulsion Conference, 1991.
- (9) Goltz, Th., Auweter-Kurtz et al, "High-Power Arcjet Thruster Experiments", IEPC 91-072 (1991).

Table 1: Fit approximations for hydrogen, hydrazine and nitrogen

Fit Coefficients	Gas		
	Hydrogen	Hydrazine	Nitrogen
$\phi$ (W/m)	36000	26300	7000
B (V)	2.76	2.43	1.58
$T_0$ (K)	7000	7000	7000
$\alpha$ (K·m/s)	1.50	1.50	1.50
Q	7.0	7.23	7.7
G (J·m/s·kg)	$2.47 \times 10^5$	$1.73 \times 10^5$	$2.20 \times 10^4$

Table 2: Computational and experimental data comparison for water-cooled 20 kW level thruster with hydrogen propellant

	Computational (Experimental)			
	Case 1A	Case 1B	Case 1C	Case 1D
$\dot{m}$ (kg/sec $\cdot 10^{-3}$ )	0.1	0.1	0.3	0.3
I (amperes)	50	150	50	150
$T_{out,0}$ (K)	700	700	500	500
$h_{c0}$ (J/kg)	$3 \times 10^9$	$8 \times 10^9$	$3 \times 10^9$	$8 \times 10^9$
$P_0$ (N/m <sup>2</sup> )	$9.02 \times 10^4$ ( $9.00 \times 10^4$ )	$1.23 \times 10^5$ ( $1.30 \times 10^5$ )	$2.03 \times 10^5$ ( $2.35 \times 10^5$ )	$2.44 \times 10^5$ ( $2.74 \times 10^5$ )
V (volts)	165 (165)	155 (140)	225 (233)	199 (198)
F (N)	0.58 (0.60)	0.81 (0.83)	1.32 (1.17)	1.63 (1.62)
$I_{sp}$ (sec)	592 (612)	876 (847)	449 (398)	554 (551)
$\eta$	0.204 (0.218)	0.141 (0.164)	0.258 (0.196)	0.148 (0.147)
$Q_{loss}$ (kW)	1.40 (1.30)	4.20 (4.00)	1.40 (1.00)	4.20 (3.30)
$R_a / R @$ constrictor exit	0.598	0.758	0.462	0.610
$C_F$	1.309 (1.358)	1.342 (1.301)	1.324 (1.002)	1.361 (1.186)

For all cases,  $\Delta V_c = 28$  V,  $R_s(0) = 0.2$  mm,  $x_{exit} = 9$  mm,  $Q = 7$ ,  $Q_{loss} = 3.5$ , and  $Q_{gr} = 4.75$ .

Table 3: Computational and experimental data comparison for radiation-cooled 20 kW level thruster with hydrogen propellant

	Computational (Experimental)	
	Case 2A	Case 2B
$\dot{m}$ (kg/sec·10 <sup>-3</sup> )	0.1	0.1
I (amperes)	50	150
T <sub>cool,0</sub> (K)	1400	1400
h <sub>c,0</sub> (J/kg)	3 x 10 <sup>9</sup>	8 x 10 <sup>9</sup>
P <sub>0</sub> (N/m <sup>2</sup> )	1.17 x 10 <sup>5</sup>	1.51 x 10 <sup>5</sup>
V (volts)	145.2 (120)	117.5 (108)
F (N)	0.73 (0.75)	0.96 (0.99)
I <sub>sp</sub> (sec)	745 (765)	979 (1009)
$\eta$	0.367 (0.467)	0.261 (0.303)
R <sub>a</sub> / R @ constrictor exit	0.558	0.722
C <sub>F</sub>	1.267	1.299

For all cases,  $\Delta V_c = 0$  V,  $R_g(0) = 0.2$  mm,  $x_{att} = 6$  mm,  $Q = 7$ ,  $Q_{out} = 3.5$ , and  $Q_{gr} = 4.75$ .

Table 4: Computational and experimental data comparison for radiation-cooled 30 kW level thruster with hydrogen propellant

	Computational (Experimental)	
	Case 3A	Case 3B
$\dot{m}$ (kg/sec $\cdot 10^{-3}$ )	0.1228	0.1228
I (amperes)	107.1	260.5
$T_{\text{out},0}$ (K)	2000	2000
$h c_0$ (J/kg)	$6 \times 10^9$	$9 \times 10^9$
$P_0$ (N/m $^2$ )	$3.63 \times 10^5$	$5.07 \times 10^5$
V (volts)	184 (172)	164 (161)
F (N)	1.238 (1.238)	1.70 (1.761)
$I_{\text{sp}}$ (sec)	1028 (1028)	1412 (1461)
$\eta$	0.331 (0.331)	0.275 (0.298)
$C_F$	1.37	1.35

For all cases,  $\Delta V_c = 0$  V,  $R_a(0) = 0.2$  mm,  $x_{\text{exit}} = 6$  mm,  $Q = 7$ ,  $Q_{\text{out}} = 3.5$ , and  $Q_{\text{fr}} = 4.75$ .

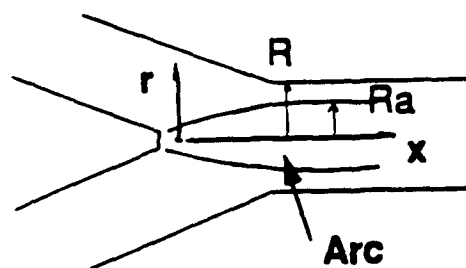


Fig. 1. Arcjet Geometry

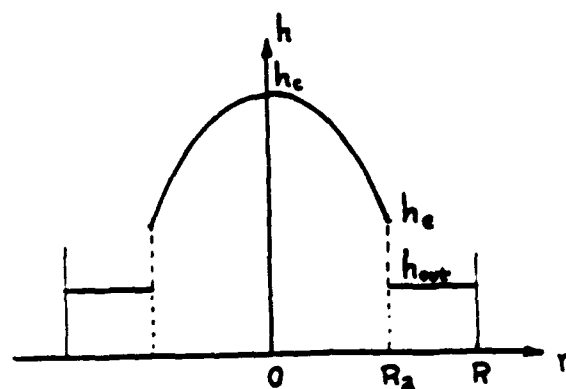


Fig. 2 Idealized enthalpy profile

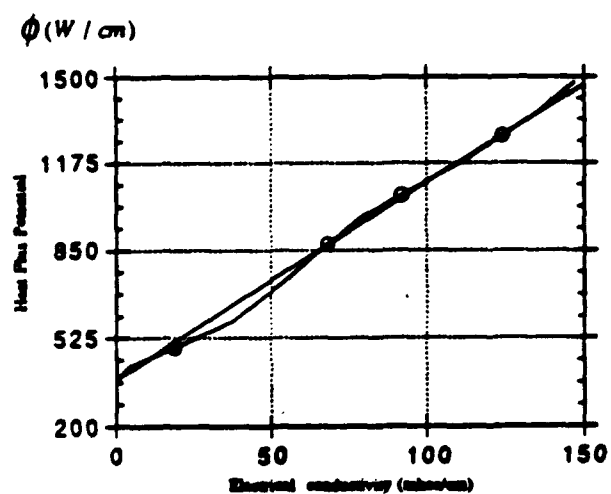


Fig. 3 Calculated heat flux potential vs. electrical conductivity (hydrogen,  $p=1$  atm.)

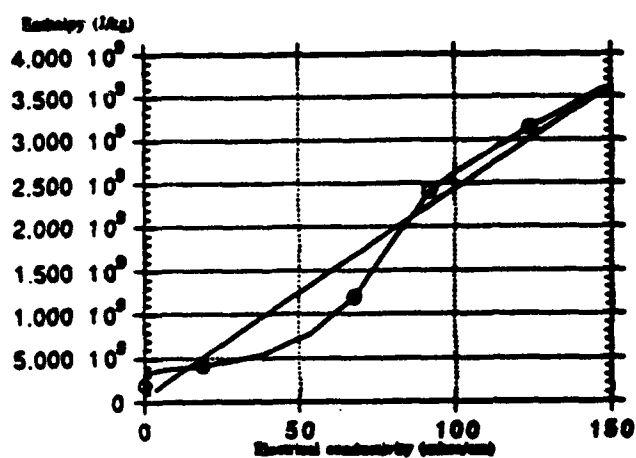


Fig. 4 Calculated enthalpy vs. electrical conductivity (hydrogen,  $p=1$  atm)

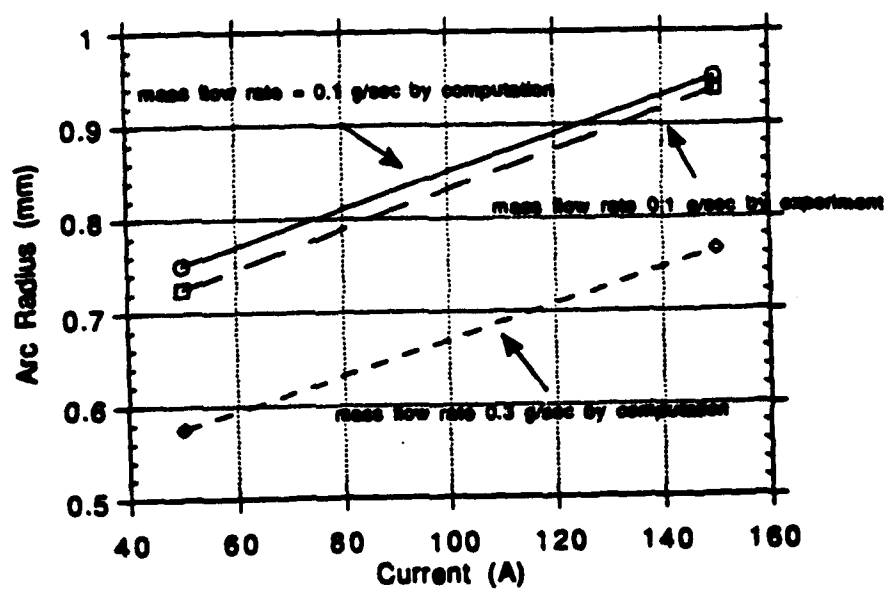


Figure 5: Computational and experimental arc radius vs. current characteristic